

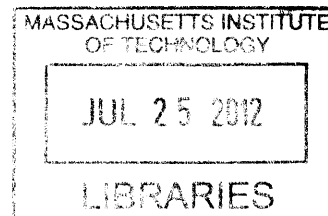
**Remote Detection of Fissile Material:
Cherenkov Counters for Gamma Detection**

by
Anna S. Erickson

B.S. Nuclear Engineering
Oregon State University, 2006

S.M. Nuclear Science and Engineering
Massachusetts Institute of Technology, 2008

ARCHIVES



SUBMITTED TO THE DEPARTMENT OF NUCLEAR SCIENCE AND ENGINEERING IN
PARTIAL FULFILLMENT OF THE REQUIREMENTS FOR THE DEGREE OF

DOCTOR OF PHILOSOPHY IN NUCLEAR SCIENCE AND ENGINEERING
AT THE
MASSACHUSETTS INSTITUTE OF TECHNOLOGY

JUNE 2011

© 2011 MASSACHUSETTS INSTITUTE OF TECHNOLOGY
All rights reserved

Signature of Author: _____
Department of Nuclear Science and Engineering, June 2011

Certified By: _____
Dr. Richard Lanza
Senior Research Scientist
Thesis Supervisor

Certified By: _____
Prof. Benoit Forget
Assistant Professor of Nuclear Science and Engineering
Thesis Reader

Certified By: _____
Dr. Adam Bernstein
Physicist at Lawrence Livermore National Laboratory
Thesis Reader

Certified By: _____
Dr. Michael Hynes
Physicist at Raytheon Integrated Design Systems
Thesis Reader

Certified By: _____
Prof. Mujid Kazimi
Professor of Nuclear Science and Engineering
Chairman of Committee on Graduate Students

Remote Detection of Fissile Material: Cherenkov Counters for Gamma Detection

by
Anna S. Erickson

Submitted to the Department of Nuclear Science and Engineering
on May 12, 2011
in Partial Fulfillment of the Requirements for
the Degree of Doctor of Philosophy in Nuclear Science and Engineering

ABSTRACT

The need for large-size detectors for long-range active interrogation (AI) detection has generated interest in water-based detector technologies. AI is done using external radiation sources to induce fission and to detect, identify, and characterize special nuclear material (SNM) through the gamma rays and neutrons emitted. Long-range applications require detectors with a large solid angle and an ability to significantly suppress low-energy background from linear electron accelerators. Water Cherenkov Detectors (WCD) were selected because of their transportability, scalability, and an inherent energy threshold.

The main objective of this thesis was to design a large-size WCD capable of detecting gamma rays and to demonstrate particle energy discrimination ability. WCD was modeled in detail using Geant4 for optimization purposes. The experimental detector is composed of an aluminum body with a high efficiency (98.5%) diffuse reflector. Cherenkov photons are detected with six 8" hemispherical Hamamatsu photomultiplier tubes (PMT). PMTs are calibrated using two monoenergetic LEDs.

The detector was shown to successfully detect gamma rays of energies above the Cherenkov threshold. The detector was able to discriminate between various sources, such as ^{60}Co and ^{232}Th , even though WCD are known for their poor energy resolution. The detector design and analysis was completed, and it was demonstrated both computationally and experimentally that it is possible to use WCD to detect and characterize gamma rays.

One of the accomplishments of this thesis was demonstration of event reconstruction capability of the detector system. A full-detector model was created using Geant4

simulation toolkit. The performance of the detector was predicted using the model and then experimentally verified. The qualitative agreement between the model and the experiment was observed. The event reconstruction was an important part of the detector performance analysis. Post-experimental data processing was done using ROOT.

Thesis Supervisor: Richard Lanza

Title: Senior Researcher in Nuclear Science and Engineering

ACKNOWLEDGEMENTS

Foremost, I would like to express my immeasurable thankfulness to my supervisors, Dr. Richard Lanza, Dr. Adam Bernstein, and Dr. Michael Hynes, who shared with me a lot of their great expertise in radiation detector design and national nuclear security. Their enthusiasm, inspiration and simply good company turned this project into an enjoyable experience for me. The support and guidance of Dr. Benoit Forget provided a great help in finishing this work.

My gratitude extends to Dr. Tony Galaitis for our many days of fruitful discussions, at MIT and outside. His contribution to the manufacturing and assembly of this detector is what made this detector real. Tony's photography skills need a special acknowledgement here since a lot of the detector pictures in this thesis have been taken by him.

I thank Dr. Russ Terry for his helpfulness and knowledge in detection electronics. I wish to thank Dr. Steven Dazeley for sharing his knowledge in operation of detectors with me and Dr. Gordon Kohse for his invaluable support in the lab.

I am indebted to my student colleagues, Zach Hartwig and Tim Gushue, for not only sharing their knowledge of principle of detector simulation, but also for providing a stimulating and fun environment to learn and work. The informal support of my friends has been indispensable, and I would particularly like to acknowledge Heather Barry, CJ Fong, Craig Gerardi, and Lara Pierpoint.

My sincere thanks also go to Clare Egan and Rachel Batista for their administrative support.

I thank my mother, Natasha, and sister, Masha, for their understanding and support when I made the decision to part with them and go across the country to be at MIT.

My studies and research at MIT would not be possible without the support and encouragement of my dearly loved husband Robert Erickson.

I dedicate this thesis to my grandparents.

This work was supported by NNSA Stewardship Science Graduate Fellowship. I am grateful to the fellowship program for their financial and personal support.

TABLE OF CONTENTS

| | |
|--|-----------|
| ACKNOWLEDGEMENTS | 5 |
| LIST OF FIGURES | 9 |
| LIST OF TABLES | 12 |
| 1. INTRODUCTION INTO THE CURRENT STATE OF THE PROBLEM: REMOTE DETECTION OF SPECIAL NUCLEAR MATERIAL | 13 |
| 1.1. THE NEW PLAYERS ON NUCLEAR ARENA | 14 |
| 1.2. COMPARISON OF SNM | 15 |
| 1.3. SUSCEPTIBILITY TO SNM SMUGGLING | 16 |
| 1.4. NEW METHODS FOR THE DETECTION OF NEW THREATS: AN OVERVIEW OF PASSIVE AND ACTIVE TECHNIQUES | 16 |
| 1.5. MOTIVATION FOR THIS THESIS: DETECTORS FOR ACTIVE INTERROGATION APPLICATIONS | 20 |
| 1.6. OBJECTIVES AND SIGNIFICANCE OF THIS THESIS | 21 |
| 1.7. OVERVIEW OF THIS THESIS | 22 |
| 2. OVERVIEW OF STANDOFF INTERROGATION SYSTEMS | 23 |
| 2.1. GOING ACTIVE: COMPARISON OF BACKGROUND AND SNM SPECTRA | 24 |
| 2.2. BEAM AND INDUCED PHOTOFISSION | 24 |
| 2.3. PRODUCTS OF PHOTOFISSION AND THEIR SIGNATURE CLASSIFICATION IN THE DETECTOR | 29 |
| 2.3.1. PROMPT RADIATION | 31 |
| 2.3.2. DELAYED RADIATION | 31 |
| 2.4. DETECTOR SPECIFICATIONS AND REQUIREMENTS | 34 |
| 2.4.1. SCINTILLATOR NEAR BEAM | 34 |
| 2.4.2. SHORTAGE OF HE-3 | 34 |
| 2.5. CHERENKOV DETECTORS | 35 |
| 3. CHERENKOV RADIATION PHENOMENON AND ITS APPLICATION TO WATER-BASED DETECTORS | 38 |
| 3.1. PROPERTIES OF CHERENKOV RADIATION: THRESHOLD AND DIRECTIONALITY | 39 |
| 3.2. LIGHT YIELD AND SPECTRAL DISTRIBUTION | 42 |
| 3.3. REVIEW OF WCD APPLICATIONS | 43 |
| 3.4. GAMMA DETECTION WITH WATER CHERENKOV COUNTERS | 45 |

| | |
|--|------------|
| 4. MODELING OF THE DETECTOR WITH GEANT4 | 48 |
| 4.1. OVERVIEW OF THE CODE CAPABILITIES | 48 |
| 4.2. MODELING OF GEOMETRY AND MATERIALS | 50 |
| 4.3. MODELING OF OPTICAL PROCESSES | 52 |
| 4.3.1. REFLECTIVITY OF THE WALLS | 52 |
| 4.3.2. WATER ABSORPTION COEFFICIENT | 54 |
| 4.3.3. EFFECT OF WATER ABSORPTION LENGTH AND REFLECTIVITY OF THE WALLS ON DETECTOR EFFICIENCY | 55 |
| 4.4. COMPUTATIONAL RESULTS AND DISCUSSIONS | 58 |
| 4.4.1. OPTIMIZATION OF THE TANK DESIGN | 58 |
| 4.4.2. SIMULATION OF ^{232}Th SOURCE | 64 |
| 5. DESCRIPTION OF THE EXPERIMENTAL GAMMA DETECTOR | 71 |
| 5.1. EXPERIMENTAL DETECTOR DESIGN | 71 |
| 5.2. FRONT-END ELECTRONICS FOR FAST SIGNAL PROCESSING | 73 |
| 5.2.1. ELECTRONICS BASED ON QDC | 74 |
| 5.2.2. ELECTRONICS BASED ON ADC | 77 |
| 5.3. PHOTOMULTIPLIER PROPERTIES | 80 |
| 5.3.1. QUANTUM EFFICIENCY | 81 |
| 5.3.2. NOISE | 83 |
| 5.3.3. SINGLE PHOTON TESTING | 83 |
| 5.4. DETECTOR RESPONSE TO LED PULSED AT VARIOUS FREQUENCIES | 89 |
| 5.5. WATER FILTRATION AND RECIRCULATION SYSTEM | 92 |
| 5.3.1 EXPERIMENTAL INVESTIGATION OF WATER PURITY EFFECTS ON SIGNAL | 92 |
| 5.6. DETECTOR RESPONSE TO VARIATIONS IN WATER PURITY | 94 |
| 6. CALIBRATION AND EFFICIENCY OF THE DETECTOR | 97 |
| 6.1. COMPUTATIONAL EVALUATION OF DETECTOR RESOLUTION | 98 |
| 6.2. SOURCES OF ERROR AND PHOTOELECTRON STATISTICS | 104 |
| 6.2.1. SYSTEMATIC UNCERTAINTIES | 105 |
| 6.3. CALIBRATION SOURCES | 110 |
| 6.4. RESULTS OF DETECTOR CALIBRATION | 113 |
| 6.5. DEAD TIME EFFECTS | 116 |
| 6.6. EFFICIENCY OF THE DETECTOR | 117 |
| 7. EVENT RECONSTRUCTION METHODOLOGY | 121 |
| 7.1. CHARACTERISTICS OF THE SIGNAL | 122 |
| 7.2. AMBIENT AND COSMOGENIC BACKGROUND | 124 |
| 7.3. BACKGROUND REJECTION METHODS | 129 |
| 7.4. FINAL (SIMULATED) EVENT SAMPLE | 132 |
| 7.4.1. SIMULATION OF $^{241}\text{AmBe}$ SOURCE | 132 |
| 7.4.2. SIMULATION CASES | 135 |
| 7.4.3. EXPERIMENTAL VERIFICATION OF $^{241}\text{AmBe}$ SPECTRUM | 142 |

| | |
|---|------------|
| 7.4.4. COMPARISON OF EXPERIMENTAL AND COMPUTATIONAL RESULTS | 146 |
| 7.5. SUMMARY OF EVENT RECONSTRUCTION METHODOLOGY | 150 |
| 8. CONCLUSIONS AND FUTURE WORK | 153 |
| 8.1. RESEARCH OBJECTIVES | 154 |
| 8.2. SUMMARY OF WORK PERFORMED | 154 |
| 8.2.1. COMPUTATIONAL MODEL | 154 |
| 8.2.2. EXPERIMENTAL DETECTOR | 155 |
| 8.3. FUTURE WORK | 156 |
| 8.4. DATA ACQUISITION SYSTEM | 158 |
| 9. BIBLIOGRAPHY | 161 |
| APPENDIX A. IDEAL CASE BASED ON TAMM-FRANK DERIVATION | 169 |
| A.1. DISPERSIVE MEDIUM, DIELECTRIC CONSTANT AND MAGNETIC PERMEABILITY | 169 |
| A.2. MAXWELL'S EQUATIONS | 170 |
| A.3. MOVING POINT CHARGE AND ITS FIELDS | 172 |
| APPENDIX B. NEUTRON DETECTION USING CHERENKOV COUNTERS | 175 |
| B.1 GD MODELING IN GEANT4: COMPARING GEANT4, DICEBOX AND ENDF LIBRARIES | 175 |
| APPENDIX C. EXAMPLES OF GEANT4 AND ROOT | 179 |
| C.1. DETECTOR GEOMETRY AND CONSTRUCTION | 179 |
| C.2. OPTICAL PHOTONS | 183 |
| C.3. SAMPLE ROOT OUTPUT ANALYSIS CODE | 184 |
| LIST OF ACRONYMS AND ABBREVIATIONS | 189 |

LIST OF FIGURES

| | |
|--|----|
| FIGURE 1-1. CRITICAL MASSES OF ^{233}U IN ^{238}U AND ^{235}U IN ^{238}U FOR A BARE METAL SPHERE. FIGURE IS TAKEN FROM FORSBERG ET AL. ⁸ | 17 |
| FIGURE 1-2. SCHEMATIC DESCRIBING AN ACTIVE INTERROGATION TECHNIQUE. A GAMMA OR NEUTRON BEAM IS DIRECTED ONTO AN OBJECT OF INTEREST, INDUCING FISSIONS IF SNM IS PRESENT. DETECTORS ARE USED TO MEASURE THE INCREASE IN RADIATION INTENSITY. | 19 |
| FIGURE 2-1. SPECTRA OF 90% ^{235}U (RED) VS. BACKGROUND (GREEN). | 25 |
| FIGURE 2-2. SPECTRA OF WGPU (RED) VS. BACKGROUND (GREEN). | 25 |
| FIGURE 2-3. GAMMA RAY INTERACTIONS. FIGURE IS TAKEN FROM GOZANI. ²² | 26 |
| FIGURE 2-4. PHOTOFISSION CROSS SECTION AS A FUNCTION OF ENERGY FOR ^{233}U , ^{235}U , AND ^{239}Pu . FIGURES ARE TAKEN FROM IAEA. ²³ | 28 |
| FIGURE 2-5. TIMELINE OF A FISSION PROCESS. FIGURE IS ADOPTED FROM GOZANI. ²² | 30 |
| FIGURE 2-6. DELAYED GAMMA RAYS WITH ENERGIES GREATER THAN 0.51 MEV FROM PHOTOFISSION OF ^{233}U AND ^{235}U (TOP), AND ^{232}Th (BOTTOM). FIGURES ARE TAKEN FROM WALTON ET AL. ²⁶ | 33 |
| FIGURE 3-1. SCHEMATIC OF CHARGED PARTICLE'S MOTION AT THE SPEED OF LIGHT IN THE MEDIUM (TOP) AND FASTER THAN PHASE VELOCITY OF LIGHT (BOTTOM). | 41 |
| FIGURE 3-2. DEPENDENCE OF THRESHOLD KINETIC ENERGY (IN UNITS OF REST ENERGY, $E_0=mc^2$) ON REFRACTIVE COEFFICIENT OF THE MEDIUM. DASHED LINE ILLUSTRATES THE CASE FOR WATER ($n=1.33$). | 41 |
| FIGURE 3-3. COMPARISON OF THRESHOLD ENERGIES FOR ELECTRONS AND GAMMA RAYS. FIGURE IS TAKEN FROM SOWERBY. ⁴⁰ | 46 |
| FIGURE 3-4. POLAR PLOT OF KLEIN-NISHINA FORMULA. THE PLOT SHOWS DEPENDENCE OF SCATTERING ANGLE OF THE ELECTRON ON ENERGY OF THE INCIDENT GAMMA RAY. FIGURE IS TAKEN FROM KNOLL. ⁴¹ | 47 |
| FIGURE 4-1. DETECTOR MODEL IN GEANT4. | 51 |
| FIGURE 4-2. SPECULAR (LEFT) VS. DIFFUSE (RIGHT) REFLECTIVITY. FIGURE IS TAKEN FROM SCHUBERT. ⁴⁵ ... | 53 |
| FIGURE 4-3. COMPARISON OF REFLECTANCE OF VARIOUS MATERIALS. CURVES A AND B CORRESPOND TO 3.0 AND 0.5 MM GORE DRP, RESPECTIVELY. CURVES C, D, E, AND F STAND FOR GRANULAR PTFE, BARIUM SULFATE, MICROPOROUS POLYESTER, AND POWDER COATING. | 53 |
| FIGURE 4-4. COMPARISON OF WATER ABSORPTION LENGTHS AS A FUNCTION OF LIGHT PHOTON WAVELENGTH. QUANTUM EFFICIENCY OF HAMAMATSU TUBES IS ALSO SHOWN (IN BLACK). | 55 |
| FIGURE 4-5. EFFECTS OF DETECTOR WALL REFLECTIVITY AND WATER ABSORPTION LENGTH ON DETECTOR'S RESPONSE. | 56 |
| FIGURE 4-6. THE NUMBER OF CHERENKOV PHOTONS DETECTED AS A FUNCTION OF THE NUMBER OF PMT'S (1 TO 6) AND THE DIFFUSE REFLECTIVITY OF THE WALL MATERIAL (0.8 TO 1.0). | 57 |
| FIGURE 4-7. TWO CONCEPTS OF TANK DESIGN. LEFT: DESIGN 1 - CENTRONICS TUBES ARE PLACED INSIDE WITH 1-CM-THICK BLOCK OF POLY IN FRONT OF THE TANK. RIGHT: DESIGN 2 - CENTRONICS TUBES ARE PLACED OUTSIDE IN A BLOCK OF POLY. | 61 |
| FIGURE 4-8. CHANGE IN DETECTOR (DESIGN 2) RESPONSE AS A FUNCTION OF GAMMA RAY'S ENERGY. | 63 |
| FIGURE 4-9. SPECTRUM OF ^{232}Th AS AN INPUT TO THE GEANT4 MODEL. | 64 |
| FIGURE 4-10. ILLUSTRATION OF THE SOURCE-DETECTOR SYSTEM. | 65 |
| FIGURE 4-11. ^{232}Th SPECTRA AT VARIOUS DISTANCES FROM THE DETECTOR. | 66 |

| | |
|---|-----|
| FIGURE 4-12. ^{232}Th SOURCE, PEAK ONLY (OTHER CONTRIBUTORS SUBTRACTED)..... | 67 |
| FIGURE 4-13. ^{232}Th SOURCE, FULL SPECTRUM AND PEAK ONLY (OTHER CONTRIBUTORS SUBTRACTED)..... | 68 |
| FIGURE 5-1. ALUMINUM BODY OF THE DETECTOR (LEFT) AND POLYPROPYLENE INSERT (RIGHT). | 72 |
| FIGURE 5-2. WATER FILTRATION AND RECIRCULATION SYSTEM (LEFT) AND LEDs POSITIONED INSIDE THE DETECTOR (RIGHT) | 73 |
| FIGURE 5-3. ELECTRICAL PULSE GENERATED BY A DETECTOR. FIGURE IS ADOPTED FROM TINTORI. ⁵² | 74 |
| FIGURE 5-4. WIRING DIAGRAM FOR QDC..... | 75 |
| FIGURE 5-5. DATA ACQUISITION SETUP..... | 76 |
| FIGURE 5-6. BLOCK DIAGRAM OF v1495. FIGURE IS TAKEN FROM CAEN. ⁵³ | 77 |
| FIGURE 5-7. FAST ADC DATA ACQUISITION SETUP..... | 78 |
| FIGURE 5-8. BLOCK DIAGRAM OF v1720 DIGITIZER. FIGURE IS TAKEN FROM CAEN. ⁵⁴ | 79 |
| FIGURE 5-9. HAMAMATSU PMT CHARACTERISTICS. FROM HAMAMATSU. ⁵⁵ | 81 |
| FIGURE 5-10. QE FOR HAMAMATSU R5912-02 TUBES..... | 82 |
| FIGURE 5-11. BLACK BOX TESTING | 84 |
| FIGURE 5-12. SCHEMATIC DIAGRAM OF PMT TESTING WITH LED | 85 |
| FIGURE 5-13. OBSERVED SINGLE PE DATA WITH 8-IN HAMAMATSU PMT. | 86 |
| FIGURE 5-14. SINGLE PHOTOELECTRON PEAK OBSERVATION. THE ABCISSA IS IN ARBITRARY BIN UNITS. | 88 |
| FIGURE 5-15. PMT RESPONSE TO LED PULSED AT FOUR FREQUENCIES, EACH INCREASING BY A LEVEL OF MAGNITUDE..... | 90 |
| FIGURE 5-17. COMPARISON OF PULSE HEIGHT CHANGES FOR VARIOUS WATER SAMPLES. | 93 |
| FIGURE 5-18. LED PLATE CORROSION. | 95 |
| FIGURE 5-19. BACKGROUND SPECTRA BEFORE AND AFTER THE TANK CLEANING. | 96 |
| FIGURE 6-1. PULSE HEIGHT SPECTRA OF GAMMA RAYS OF VARIOUS ENERGIES. | 101 |
| FIGURE 6-2. PULSE HEIGHT (PEAK LOCATION) AND RESOLUTION OF THE DETECTOR AS A FUNCTION OF GAMMA RAY ENERGY (MEV). THE ERROR BARS CORRESPOND TO $\pm\Sigma$ | 102 |
| FIGURE 6-3. DETECTOR RESPONSE TO GAMMA RAYS WITH ENERGIES OF 2, 3, AND 5 MEV. | 102 |
| FIGURE 6-4. SQUARE OF RESOLUTION VS. INVERSE OF LIGHT OUTPUT (SOLID LINE). RESULTS OF LEAST SQUARE FIT (DASHED LINE) ARE ALSO SHOWN ON THE PLOT. | 104 |
| FIGURE 6-5. PEDESTAL AND BACKGROUND SPECTRA FOR ALL 6 PMTS..... | 107 |
| FIGURE 6-6. BG SPECTRA AFTER PEDESTAL SUBTRACTION AND NORMALIZATION. | 108 |
| FIGURE 6-7. SPECTRA VS. AVERAGE SPECTRUM..... | 109 |
| FIGURE 6-8. DISTRIBUTION OF LOW-ENERGY PEAKS. THE LINE REPRESENTS THE AVERAGE OF THE SIX..... | 110 |
| FIGURE 6-9. A SPECTRUM OF THORIUM SLUG USING AN HPGE DETECTOR SHOWING THE MANY GAMMA RAY LINES ORIGINATING FROM DAUGHTERS OF ^{232}Th . THE 2.6 MEV GAMMA RAY ORIGINATES FROM THE DECAY OF ^{208}Tl TO ^{208}Pb , BUT ^{208}Tl IS ONLY REACHED ABOUT 30% OF THE TIME. (100 SECOND RUN) | 112 |
| FIGURE 6-10. DETECTOR AND SOURCE SETUP. SOURCE CAN BE MOVED PERPENDICULARLY TO THE DETECTOR SURFACE..... | 113 |
| FIGURE 6-11. EXPERIMENTAL INTEGRATED SPECTRA OF FOUR SOURCES..... | 114 |
| FIGURE 6-12. COMPUTATIONAL (GEANT4) INTEGRATED SPECTRA OF FOUR SOURCES (NORMALIZED). | 114 |
| FIGURE 6-13. COMPARISON OF EXPERIMENTAL AND COMPUTATIONAL CALIBRATION. THE UNITS ARE DIFFERENT FOR EXPERIMENTAL AND COMPUTATIONAL DATA SETS, BUT THE SLOPE IS NEARLY THE SAME. | 116 |
| FIGURE 6-14. SPECTRUM OF BACKGROUND AND ^{60}Co SOURCE..... | 118 |
| FIGURE 6-15. SPECTRUM OF ^{60}Co SOURCE AFTER BACKGROUND WAS SUBTRACTED. NOTE THAT Y-AXIS IS NOW COUNT RATE PER SECOND. | 119 |
| FIGURE 6-16. SPECTRUM OF ^{60}Co SOURCE AFTER BACKGROUND WAS SUBTRACTED. | 119 |
| FIGURE 6-17. SPECTRUM OF ^{137}Cs SOURCE AFTER BACKGROUND WAS SUBTRACTED. NOTE THAT ^{137}Cs IS ACTUALLY 15 MICROCI..... | 120 |

| | |
|--|-----|
| FIGURE 7-1. EXPECTED SIGNAL FROM VARIOUS TARGET INTERROGATIONS. THE PHOTON ENERGIES SHOWN IN THE PLOT ARE 0.5 TO 10 MeV. THE TIME CUTOFF IS 100 MSEC AFTER THE INTERROGATION. [1 SHAKE = 10 NS (10^{-8} s)]..... | 123 |
| FIGURE 7-2. DECAY CHAINS OF ^{232}Th AND ^{238}U | 125 |
| FIGURE 7-3. BACKGROUND GAMMA SPECTRUM OBTAINED WITH AN UNSHIELDED HPGe DETECTOR, (6293 s LIVE TIME). | 127 |
| FIGURE 7-4. PROGENIES OF COSMIC RAY INTERACTING WITH THE ATMOSPHERIC GASES AND EARTH CRUST. | 128 |
| FIGURE 7-5. BACKGROUND RATES IN THE CHERENKOV TANK WITH MAJORITY SETTINGS OF 1, 2, AND 3 PMTs. | 131 |
| FIGURE 7-6. $^{241}\text{AmBe}$ SOURCE DECAY WITH NEUTRON ABSORPTION ON H IN WATER. | 133 |
| FIGURE 7-7. $^{241}\text{AmBe}$ SOURCE NEUTRON SPECTRUM..... | 134 |
| FIGURE 7-8. AMBe SPECTRUM GENERATED IN CHERENKOV DETECTOR. THE SIGNAL DUE TO 4.4 MeV GAMMA RAYS IS SHOWN IN RED. | 135 |
| FIGURE 7-9. $^{241}\text{AmBe}$ SOURCE AND SHIELDING NEAR THE DETECTOR..... | 136 |
| FIGURE 7-10. SIMULATION RESULTS FOR AMBe SOURCE. | 138 |
| FIGURE 7-11. BARE SOURCE, NEUTRON CAPTURES. THE DIMENSIONS ARE IN CM. LEFT: FACE OF THE DETECTOR. RIGHT: CAPTURES ALONG THE DEPTH OF THE TANK. | 139 |
| FIGURE 7-12. NEUTRON CAPTURES IN THE TANK AND IN THE POLYETHYLENE SHIELDING PLACED ON FOUR SIDES AROUND THE SOURCE. NO POLYETHYLENE WAS PLACED BETWEEN THE TANK AND THE SOURCE. | 140 |
| FIGURE 7-13. NEUTRON CAPTURES IN THE TANK AND IN THE POLYETHYLENE SHIELDING PLACED ON FIVE SIDES AROUND THE SOURCE. 10-CM POLYETHYLENE BLOCK WAS PLACED BETWEEN THE TANK AND THE SOURCE..... | 141 |
| FIGURE 7-14. EXPERIMENTAL SETUP OF AMBe SOURCE AND THE DETECTOR. TOP: SHIELDING ON FOUR SIDES. BOTTOM: SHIELDING ON FIVE SIDES WITH POLYETHYLENE BETWEEN THE SOURCE AND THE DETECTOR. THE SOURCE IS NOT SHOWN. | 143 |
| FIGURE 7-15. EXPERIMENTAL SPECTRA OBTAINED WITH AMBe SOURCE. THE BACKGROUND IS CLEARLY DISTINCT FROM THE SOURCE SPECTRA. | 144 |
| FIGURE 7-16. BACKGROUND-SUBTRACTED AMBe SPECTRA..... | 145 |
| FIGURE 7-17. COMPARISON OF BARE AMBe SOURCE SPECTRA OBTAINED USING GEANT4 MODEL AND EXPERIMENTAL SETUP..... | 147 |
| FIGURE 7-18. COMPARISON OF EXPERIMENT AND SIMULATION AFTER SMOOTHING FUNCTION WAS APPLIED. THE UNITS OF X-AXIS ARE ARBITRARY TO SHOW THE COMPARISON..... | 150 |
| FIGURE B-1. COMPARISON OF GEANT4 AND DICEBOX GAMMA CASCADE GENERATION FOLLOWING NEUTRON CAPTURES ON GD. | 177 |

LIST OF TABLES

| | |
|---|-----|
| TABLE 2-1. SELECTED PHOTONUCLEAR ENERGY THRESHOLDS..... | 27 |
| TABLE 3-1. THRESHOLD KINETIC ENERGY FOR VARIOUS PARTICLES. | 42 |
| TABLE 4-1. COMPARISON OF TWO DESIGNS. | 62 |
| TABLE 4-2. CUTS APPLIED TO VARIOUS DISTANCE CASES. | 69 |
| TABLE 5-1. TEST PARAMETERS AND OUTPUT VALUES OF SINGLE PHOTOELECTRON TESTING. | 87 |
| TABLE 5-2. OPERATIONAL CHARACTERISTICS OF PMTS..... | 88 |
| TABLE 5-3. DEAD TIME OF THE DETECTION SYSTEM AS A FUNCTION OF LED FREQUENCY..... | 91 |
| TABLE 6-1. AVERAGE PHOTOELECTRON PRODUCTION AS A FUNCTION OF GAMMA RAY ENERGY. | 99 |
| TABLE 6-2. SUMMARY OF CALIBRATION SOURCES..... | 111 |
| TABLE 6-3. SUMMARY OF DETECTOR COUNT RATES FOR ¹³⁷ Cs (3 CHECK SOURCES) AND ⁶⁰ Co SOURCES. | 120 |
| TABLE 6-4. SUMMARY OF LIVE PULSER DATA USED FOR NORMALIZATION. | 120 |
| TABLE 7-1. DECAY CHAINS AND SELECTED ENERGIES..... | 126 |

1. Introduction into the current state of the problem: remote detection of special nuclear material

The nuclear industry has been trying to revitalize itself by promoting nuclear energy as a solution to carbon emissions, as a safe and reliable source of power, and a way to decrease the nation's dependence on foreign oil. The opposition to nuclear power has traditionally raised concerns over reactor safety and waste disposal, which have largely been political and to a lesser degree technical issues. Moreover, the nuclear industry is often referred to as "dirty and dangerous" because of the possibility of terrorist groups using nuclear materials as radiological or nuclear weapons. A common belief is that the expansion of the nuclear industry would inevitably lead to clandestine weapon production facilities by the so-called "threshold" states – those that chose not to use their nuclear capabilities towards weapons production – using their civilian nuclear power program as a cover.¹ Even though the transfer of assembled nuclear weapons has not yet been recorded in the history of terrorism, but rather the transfer of technology, the nuclear materials could be acquired by a terrorist group and smuggled into the country or detonated in or near large port cities. In the face of political and social opposition created by these risks, the development and advancement of the nuclear industry is critically dependent upon the capabilities of nuclear detection and control to discourage potential proliferators.

1.1. The new players on nuclear arena

The threats of nuclear terrorism and proliferation have become the focus of the political and social arena in the 21st century. After the end of Cold War, the possibility of nuclear war decreased significantly. On the other hand, nuclear technologies, materials, and expertise have been spreading around the globe in the past few decades, increasing the possibility of a nuclear terrorist attack. In fact, the 2010 Nuclear Posture Review indicated that "today's most immediate and extreme danger is nuclear terrorism."² The non-state groups, for example al Qaeda and Aum Shinrikyo (currently known as Aleph), are seeking to obtain key nuclear weapons components.³ Nuclear proliferation has become a growing concern; the active involvement of Iran and the Democratic People's Republic of Korea (DPRK) in nuclear programs and their aspirations to become nuclear weapons states created international pressure towards the two countries to comply with the Nonproliferation Treaty (NPT).⁴

The best way to manage a problem is to prevent it, in this case by knowing what is being done at nuclear facilities, such as power plants or enrichment plants, and by monitoring materials entering the country. The ultimate question is not whether the possession of special nuclear material (SNM) is being sought by terrorist organizations, but rather how they could be prevented from acquiring and using them. The problem of material accounting has been a driving force in the development of detectors for measuring penetrating radiation from fission and radioactive decay. The ability to find SNM using an advanced detection setup and to identify its origin using nuclear forensics is an effective countermeasure against an attacker, preventing them from even considering bringing a weapon into the country. Nuclear detection and forensics have a role of discouraging nuclear terrorism by increasing the chance of failure of a terrorist plot.

1.2. Comparison of SNM

SNM is a broad term for fissile materials which by definition can sustain an explosive chain reaction. SNM includes ^{233}U , ^{235}U , ^{239}Pu , and ^{237}Np . Of these, ^{235}U is the only naturally occurring isotope. The other isotopes can be produced in a nuclear reactor or by using an accelerator. The IAEA definition of a "significant quantity" of SNM is the amount of fissile material required to make one nuclear weapon equivalent to first generation, which amounts to 25 kg of uranium 90% enriched in ^{235}U or 8 kg of ^{239}Pu .⁵ Globally, the stockpiles of highly enriched uranium (HEU) and separated plutonium are estimated to be 1670 ± 300 and 500 metric tons, respectively.⁶

What is considered a significant amount of SNM for a proliferator, and what is the best way to "import" it into the country? The answer depends on the capabilities of the nuclear actors^a and the capabilities of the U.S. to address the threat.⁷ Building a weapon is not as difficult as it was a few decades ago due to the extensive knowledge base and the wider availability of experts on the subject. The size of the device that can be constructed depends on the type and enrichment level of the acquired SNM. Investment in weapon-grade uranium (WGU) or plutonium (WGP) may not be necessary since a weapon can be produced with much lower enrichment levels. For example, the critical size of a bare sphere of 20% enriched uranium is 21.1 cm in radius and 746.3 kg.⁸ This is shown on Figure 1-1 along with other examples. The device made with such uranium would not be compact or easy to fit into an artillery shell, but delivery to a port as a sea cargo or smuggling by land is feasible.

^a Nuclear actors is a comprehensive term for nations, rogue regimes and terrorist groups as defined by Hynes et al.

^b TEU stands for twenty-foot equivalent unit (container), a measure used for capacity in container transportation.

^c Such gamma rays are characteristic of ^{235}U photopeak and are easily attenuated by lead

1.3.Susceptibility to SNM smuggling

In his testimony before a Senate subcommittee in 2002, Capt. W. Schubert, the Maritime Administrator for the US Transportation Security Administration, stated that U.S. seaports experience particular “susceptibility of container shipments as a delivery system for an enemy's weapons, with over 12 million TEU's/year^b arriving at our shores.”⁹ In 2003, the Megaport Initiative aimed at internationally enhanced “detection capabilities for special nuclear and other radioactive materials in containerized cargo transiting the global maritime shipping network”¹⁰ was launched. However, even if the search was completed at the port of embarkation, this does not prevent a transfer mid-sea or at an intermediate stop en route. As part of the initiative, active interrogation standoff systems are currently under development.

1.4.New methods for the detection of new threats: an overview of passive and active techniques

In order to provide adequate protection against nuclear material misuse, seaport detection systems are envisioned to be one piece of a multilayered defense.¹¹ The two primary approaches to detecting SNM are passive detection and active interrogation. Passive techniques¹² rely on the detection of radiation naturally emitted by SNM. Active interrogation¹³⁻¹⁷ uses external radiation sources (for example, gamma or neutron beams) to induce fission to detect, identify, and characterize SNM. The choice of a particular

^b TEU stands for twenty-foot equivalent unit (container), a measure used for capacity in container transportation.

technique depends on the range of detection as well as the type of SNM, requiring an optimization between usability and performance issues.

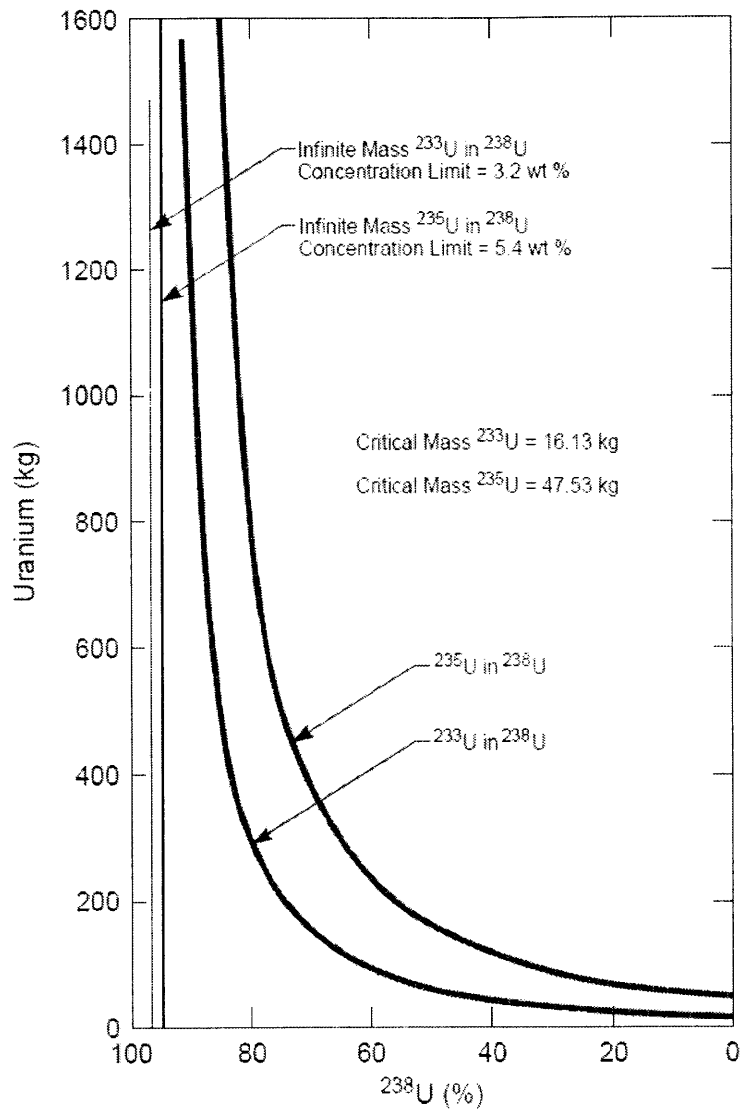


Figure 1-1. Critical masses of ^{233}U in ^{238}U and ^{235}U in ^{238}U for a bare metal sphere. Figure is taken from Forsberg et al.⁸

Passive techniques are simple and safe in use, but only perform well when the detector can be placed in the vicinity of the suspicious object surrounded with a minimum amount of shielding. For example, characteristic gamma radiation of HEU not contaminated with impurities such as ^{232}U is 0.186 MeV^c, making shielding rather straightforward for the smuggler and complicating the detection of above-background levels with a low false positive rate. In addition, there is a significant self-shielding associated with non-irradiated nuclear materials.

Ziock et al. have reported one important example of successful long-range passive detection of fissile materials.¹² A combination of imaging and detection allowed for the detection of isolated radioactive objects by estimating the local background signal. The detector used a one-dimensional coded aperture based on 19-element uniformly redundant array (URA) pattern.

Active interrogation systems have been receiving special attention from the Department of Defense because of their superior detection and material characterization capabilities over passive systems. Background radiation significantly limits the sensitivity of passive detectors, which rely on naturally emitted radiation from SNM. On the other hand, substantial shielding would be required to attenuate high-energy interrogating gammas and emitted fission neutrons and gammas. Active interrogation systems are thus more effective because they use gamma rays or neutron beams to induce desired nuclear reactions. Figure 1-2 illustrates the approach used in active interrogation. Both gamma and neutron beams are capable of inducing fission in SNM, and the choice of one over the other depends on application. Interrogating radiation is collimated into a beam and directed onto an object of interest. The response of the SNM is then measured by the detectors. Detailed descriptions of active interrogation systems along with interrogation methods are provided in Chapter 2.

^c Such gamma rays are characteristic of ^{235}U photopeak and are easily attenuated by lead shielding. Decay of ^{232}U results in the thorium decay chain final radioactive nuclide in which is ^{208}Tl , producing 2.62 MeV gamma rays that are significantly harder to attenuate by shielding.

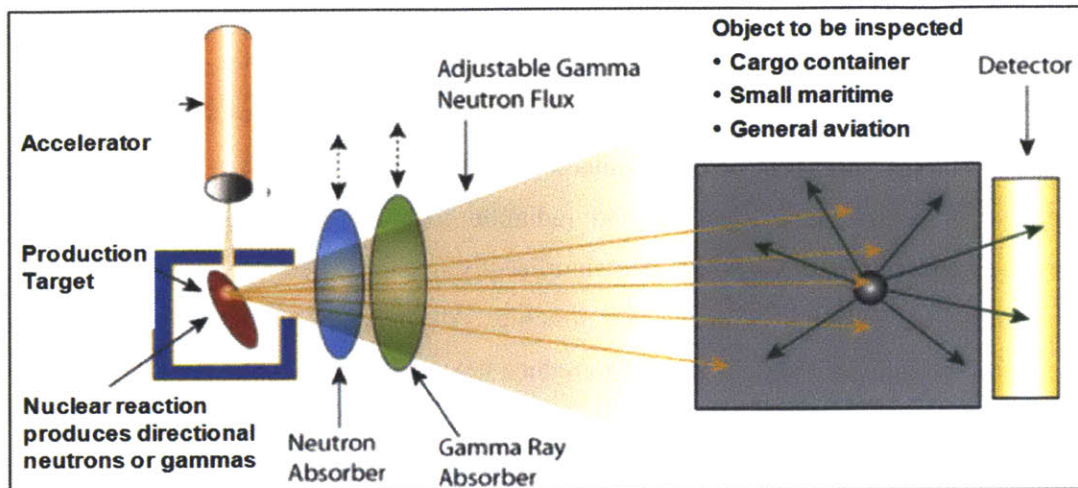


Figure 1-2. Schematic describing an active interrogation technique. A gamma or neutron beam is directed onto an object of interest, inducing fissions if SNM is present. Detectors are used to measure the increase in radiation intensity.

Examples of beam-induced nuclear reactions include fission and nuclear fluorescence resonance. In addition to enhanced penetration abilities, high-energy gammas are able to induce signature (γ, n) and (γ, f) reactions with ^{235}U and ^{239}Pu making it faster to detect SNM.¹⁴ The gamma rays produced as a consequence of delayed β decay of fission products have high yields and characteristic high energies, which distinguish them from background photons.¹⁷ It is interesting to note that the energy spectrum of these gammas is typically a continuum-like spectrum in the energy range of 3 to 10 MeV rather than characteristic spectral lines.

1.5.Motivation for this thesis: detectors for active interrogation applications

Currently, the detectors used in nuclear security applications suffer from three main problems: high background radiation, operational difficulties, and shortage of detector medium supply. Background radiation includes terrestrial and cosmogenic neutrons and gamma rays, which can significantly impact the sensitivity of the detector and must be reduced as much as possible. All detectors inevitably suffer from background radiation, and the goal is to reduce it as much as possible. Ease of operation of most detectors in the field is limited. For example, high purity Ge detectors require cryogenic cooling, and liquid scintillators can be hazardous. In active interrogation applications, scalability of the detectors and their ability to recover quickly from radiation flash near pulsed systems, for example electron accelerators, is also important.

Existing SNM detection systems used in Radiation Portal Monitors (RPM) are generally scintillators for detecting photons and ^3He tube¹⁸ for detecting neutrons. Radiation detection equipment needs to be capable of detecting both gammas and neutrons. This is because the two types of radiation require very different shielding, making it harder for SNM to be concealed. ^3He detectors are widely used because of the high thermal neutron cross section (5330 b)¹⁸ which also has $1/v$ behavior, which means that ^3He tubes exhibit strong neutron energy dependence. The dependence of cross section on energy allows embedding the detectors in moderating materials to maximize their counting efficiency. One of the main drawbacks of such detectors is their high cost due to the limited supply of ^3He . Presently, there are no good alternative options for ^3He detectors. Scintillators, which convert the energy of incident radiation into detectable light, can be organic, such as aromatic hydrocarbon compounds, or inorganic, such as NaI or CsI doped with Tl.¹⁹ Plastic scintillators are generally expensive to build and cannot easily be doped with neutron-capturing additives such Gd or ^6Li without a substantial reduction in light output.²⁰ Liquid scintillators can be toxic, posing operational

hazards. In application to active interrogation techniques that rely on prompts radiation counting, one of the main limitations of scintillators is their sensitivity to gamma bursts near the output of a linear accelerator. Pulsed electron linear accelerators are typically used as radiation sources for high-energy gamma rays, which induce large signals in nearby scintillators that may take very long times, up to minutes, to decay.

SNM detection requires a simple, low cost, scalable, non-hazardous system with an inherent threshold for the detection of both gammas and neutrons. Finding a detector that meets all of these requirements is a challenge. In this thesis, the limitations of current detectors are addressed by investigating Cherenkov counters for the detection of gamma rays and in the energy range applicable to national security needs.

1.6.Objectives and significance of this thesis

The purpose of this research is to investigate the principles of design and applicability of the use of water-based Cherenkov detectors for gamma detection and their use in an active interrogation system. The work focuses on gamma interrogation of SNM and photon-induced fission.

An optimization study of Cherenkov detector design was performed using the Monte-Carlo-based code Geant4. The model was further refined and validated using experimental benchmark data. The model was also used to predict performance and scaling of these detectors for other large-scale applications.

The main objective of this research was to determine whether water Cherenkov detectors are suitable for gamma detection. It was shown that the detector is sensitive for gamma rays of energies as low as 1.1 MeV (^{60}Co check source.)

1.7. Overview of this thesis

The thesis is organized into eight chapters. The first chapter provides an overview of the need for active interrogation systems. Currently employed active interrogation techniques as well as long-range standoff active interrogation system specific to this thesis are discussed in Chapter 2. Chapter 3 focuses on the physics of Cherenkov light and detectors based on the phenomenon. Chapter 4 describes the computational model created using the Geant4 code. Results of optimization studies are also explained in Chapter 4. The experimental setup, data acquisition system and water filtration system are described in Chapter 5. A description of detector calibration and its response to various sources are provided in Chapter 6. Chapter 7 brings computational and experimental results together in the form of event reconstruction and selection methodology. Finally, the conclusions of this study and future recommendations are summarized in Chapter 8.

2. Overview of standoff interrogation systems

As was briefly mentioned in Chapter 1, active interrogation techniques are based on the use of an external radiation source, for example neutrons or photons, to induce fission or photofission, respectively. An active interrogation system would undergo the following steps in order to detect and potentially characterize the SNM:

1. A linear accelerator (LINAC) produces a beam of electrons which are incident on a production target.
2. Depending on the accelerator target, photons and secondary neutrons are produced.
3. After going through a gamma or neutron “filter”, the radiation is collimated into a beam.
4. The beam is directed towards the interrogation target, inducing fission or photofission if SNM is present. Note that the beam undergoes a spread as a function of the square of the distance separating the LINAC and the target.
5. The products of induced (photo)fission reactions are emitted in 4π geometry. The intensity of the feedback radiation decreases as the inverse of the square of the distance separating the target and the detectors.
6. Large-size detectors are installed near the LINAC or away from the interrogation setup to detect the radiation feedback from fission or photofission.
7. The response of the detectors may be used to determine whether the feedback is from SNM or background.

8. Depending on the detector, the energy or timing (or both) of the detected particles can be used to potentially characterize the material.

While the focus of this work is on the detection systems, it is important to review the overall interrogation setup as well as induced fission and its products, prompt and delayed, in order to understand the detector behavior in various scenarios.

2.1. Going active: comparison of background and SNM spectra

Detecting SNM at a distance is a challenge. One of the main difficulties associated with long-range detection is the presence of background, which may mask SNM signatures. Figures 2-1 and 2-2 show spectra taken with high-purity germanium (HPGe) detector for unshielded HEU and weapons grade Pu (WGPu) at 1 m distance.²¹ Note that in the case of HEU, the radiation given off by the source is barely above the background. In the case of WGPu, most of the characteristic radiation lies below 1 MeV, making it practically impossible to detect WGPu at a distance using passive techniques.

2.2. Beam and induced photofission

The focus of this thesis is on detection of the feedback radiation from photon-induced fission. Photons can undergo various interactions in matter, including photoelectric effect, Compton scattering, and pair production.

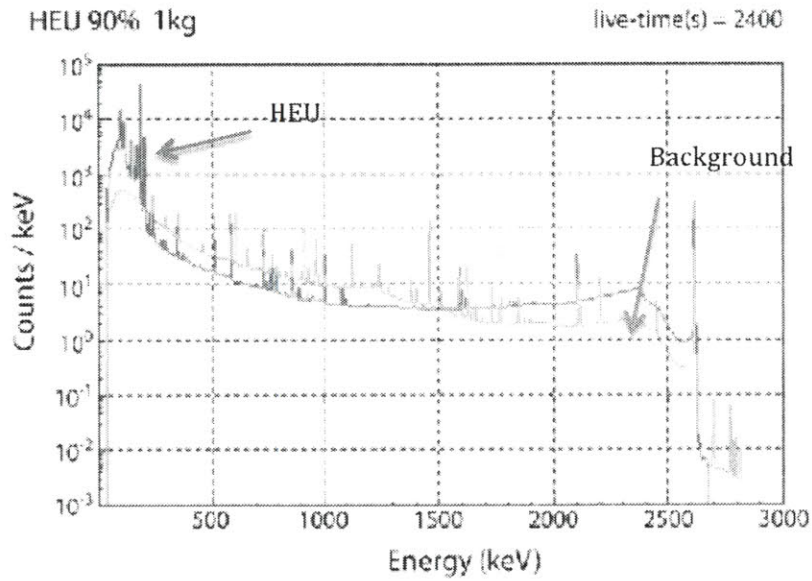


Figure 2-1. Spectra of 90% ^{235}U (red) vs. background (green).

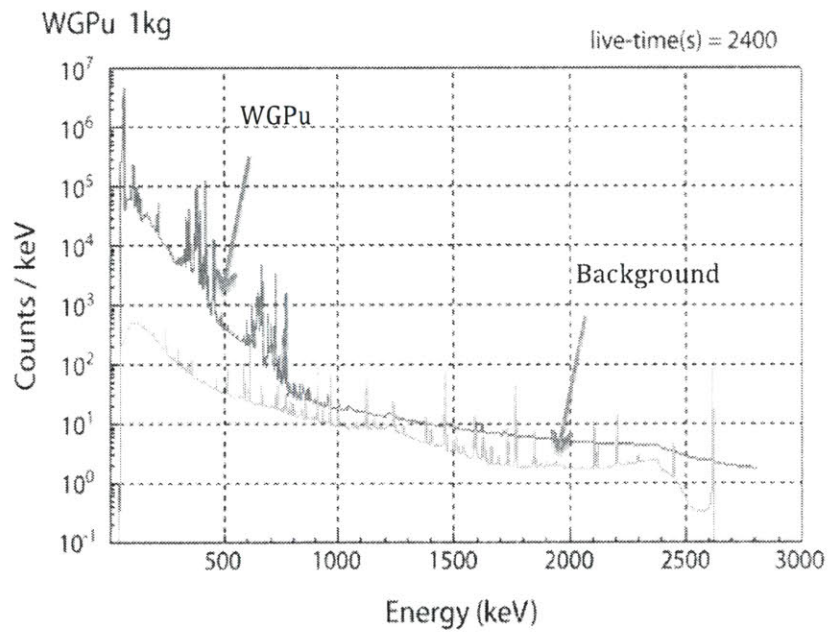


Figure 2-2. Spectra of WGPu (red) vs. background (green).

In addition, high-energy photons can undergo additional reactions, such as ejection of a photoneutron (γ, n), photofission (γ, f), and double-neutron production ($\gamma, 2n$). The six aforementioned reactions are illustrated in Figure 2-3.

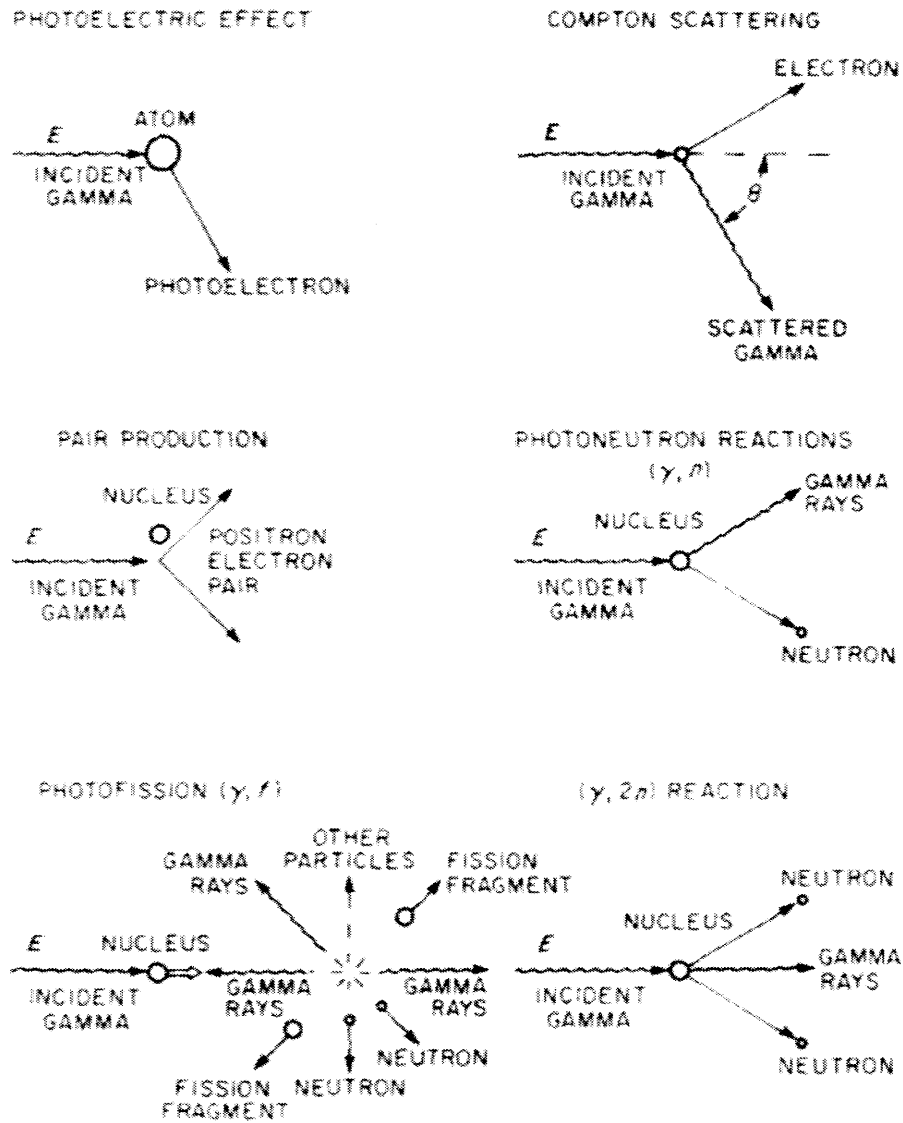


Figure 2-3. Gamma ray interactions. Figure is taken from Gozani.²²

The energy of such interrogating photons is an important metric in active interrogation applications. First, the interrogating beam must be energetic enough to induce photofission. Table 2-1 summarizes the energy thresholds for select materials. Note that photoneutrons can be created in all materials. Table 2-1 lists SNM isotopes as well as elements frequently encountered in structural and background materials. Second, the cross section of photoneutron ejection and photofission is energy-dependent. Figure 2-3 shows dependence of photofission cross section of ^{233}U , ^{235}U , and ^{239}Pu on photon energy. Note that for these isotopes, the cross section decreases when the energy of the interrogating photon beam rises above 15 MeV. On the other hand, attenuation of gamma rays is also energy dependent: higher energy photons are more penetrating. Thus, the choice of beam energy in active interrogation application is about the trade-off between the beam penetration abilities and the photofission cross section.

Table 2-1. Selected photonuclear energy thresholds.

| Nuclide | (γ ,f) [MeV] | (γ ,n) [MeV] | Notes |
|-------------------|----------------------|----------------------|----------------------------------|
| ^2H | | 2.22 | From IAEA ²³ |
| ^{12}C | | 18.72 | From IAEA |
| ^{14}N | | 10.55 | From IAEA |
| ^{16}O | | 15.66 | From IAEA |
| ^{27}Al | | 13.06 | From IAEA |
| ^{56}Fe | | 11.20 | From IAEA |
| ^{232}Th | 5.40±0.22 | 6.44 | From Koch et al. ²⁴ |
| ^{237}Np | 5.6±0.3 | 6.628 | From Berman et al. ²⁵ |
| ^{233}U | 5.7±0.3 (Berman) | 5.74 (IAEA) | |
| ^{235}U | 5.31±0.25 (Koch) | 5.30 (IAEA) | |
| ^{238}U | 5.08±0.15 (Koch) | 6.15 (IAEA) | |
| ^{239}Pu | 5.8±0.2 (Berman) | 5.65 (IAEA) | |

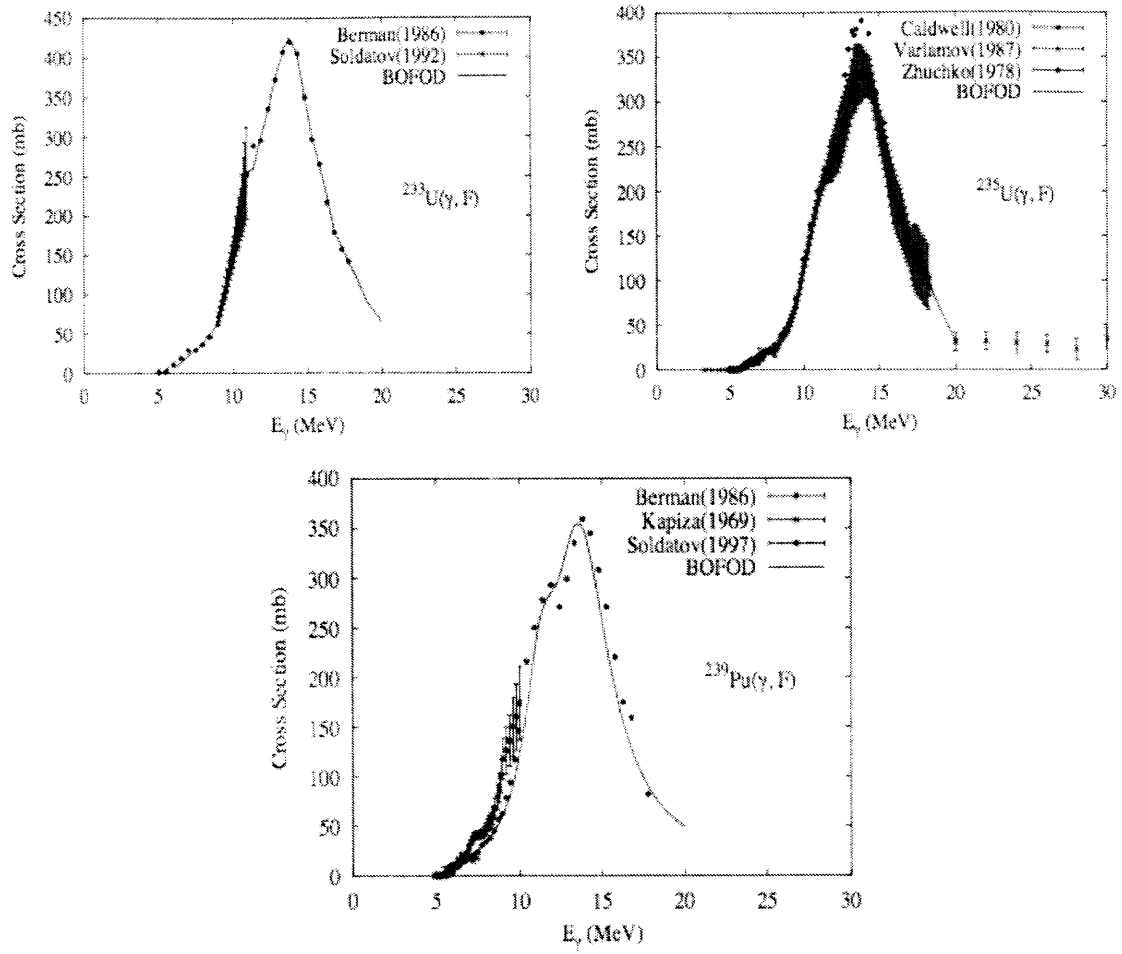


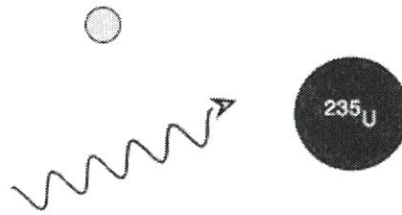
Figure 2-4. Photofission cross section as a function of energy for ^{233}U , ^{235}U , and ^{239}Pu . Figures are taken from IAEA.²³

2.3. Products of photofission and their signature classification in the detector

A significant advantage of active interrogation detection of SNM over passive methods is an abundant, energetic and time-dependent radiation feedback, in the form of both gamma rays and neutrons. Regardless of the fissile or fissionable nucleus, the fission or photofission process undergoes the same steps through a timeline as illustrated in Figure 2-4. After the interrogating particles (photons or neutrons) initiate fission events (original nucleus is shown as ^{235}U , but can be any other SNM nuclide), prompt neutrons and gamma rays are released. Depending on the nucleus, there are on average 2-3 prompt neutrons per fission and about 8 photons. In 0.1-100 seconds following the prompt radiation release, delayed particles are emitted. The number of delayed emitted neutrons is two orders of magnitude less than that of the prompt release. However, the number of delayed gamma rays is nearly the same. Thus, detection of delayed gamma radiation plays an important role in active interrogation applications.

It is interesting to note that photons of sufficiently high energy can induce photoneutron emission in non-fissile materials, for example in structural components. Some threshold energies are shown in Table 2-1. However, interrogation of non-fissile materials will result in “prompt” radiation (γ, n) release only. Delayed radiation is characteristic only of fissile materials.

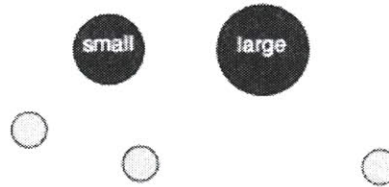
1. Initial condition
Neutron or gamma
incident on a nucleus



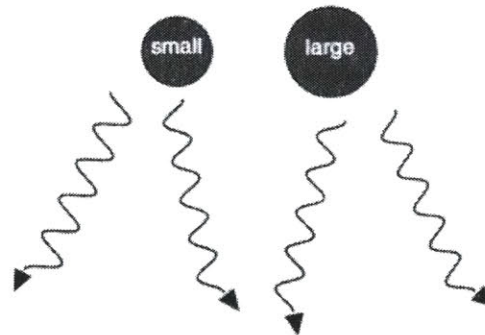
2. 10^{-15} seconds after
irradiation.
The nucleus is split into
two independent fission



3. 10^{-20} seconds after
step 2.
2 to 3 prompt neutrons
per fission



4. 10^{-17} seconds
following step 2.
 ~ 8 prompt gammas per
fission



5. 0.1-100 seconds
following step 2.
 $\sim 10^{-2}$ delayed neutrons
and ~ 8 delayed gammas
per fission

Figure 2-5. Timeline of a fission process. Figure is adopted from Gozani.²²

2.3.1. Prompt radiation

Prompt fission neutrons are those emitted 10^{-12} - 10^{-13} seconds after the nucleus is split. Prompt radiation feedback consists of energetic and abundant neutrons and gamma rays. Measurement of prompt neutrons can provide information regarding the original nucleus. While neutron detection is possible using Cherenkov counters, and some aspects of neutron detection will be discussed in this thesis, the focus is on gamma ray detection. ^{10}B detectors are used in addition to gamma Cherenkov detectors to provide information about neutrons.

2.3.2. Delayed radiation

In the fission process, the original nucleus decays into fission fragments, which are radioactive and have specific decay products. Even though the feedback from delayed radiation is less energetic and abundant than from prompt radiation, the time signature allows identification of SNM rather than mistake it for other materials, for example structural components. While delayed neutrons can be a better representation of the original nucleus, their rather low number makes detection difficult.

Walton et al.²⁶ reported that when ^{238}U , ^{235}U , and ^{232}Th were bombarded with 20 MeV x-rays, “components of short-lived gamma rays, which are attributed to the decay of isomers formed either in fission or, less likely, by other photoreactions, contributed markedly to the gamma activity for times up to 800 μsec after the beam pulse.” Gamma ray emission rate per fission as was obtained experimentally by Walton et al. is shown in Figure 2-6. The main difference between ^{235}U and the other two nuclides is that gamma ray emission rate during first 200 μsec is much higher for ^{235}U . Note that all three curves

have similar shapes including early (before 600 μsec) decay constant supporting the suggestion that all three curves are associated with beta decay of fission fragments.

Griffin²⁷ attempted to describe the behavior of delayed gammas from fission fragments of ^{235}U , with extension to other isotopes, using theoretical understanding of beta decay. The theoretical results reproduce the shape of experimental curves obtained by Walton et al.

Recent studies by Beddingfield and Cecil²⁸ and Swanberg et al.²⁹ showed that it is possible to identify SNM and to distinguish between different SNMs using delayed gamma ray signatures. Beddingfield and Cecil developed a method of distinguishing between fissile materials based on gamma ray intensity measures and their comparison with theoretical calculations. Swanberg et al. used low-resolution gamma counters to detect beta-delayed gamma rays from ^{235}U and ^{239}Pu neutron-induced fissions. The main difference between their studies of beta-delayed gamma rays and others³⁰ is their use of low-resolution scintillators which do not allow for photopeak identification. Thus, broad features were used for the analysis by examining energy spectra and temporal behavior.

Large-area Cherenkov detectors are designed for high-efficiency gamma detection done mostly through Compton interactions. It is rather difficult to characterize material with Cherenkov detectors because of the poor energy resolution of such detectors. Based on the study by Swanberg et al., it may be possible to differentiate between various SNM; however, the challenge is in long-distance away from the source which may smear any characteristic spectral and temporal features of SNM. Nonetheless, it is possible to detect SNM and to distinguish it from background.

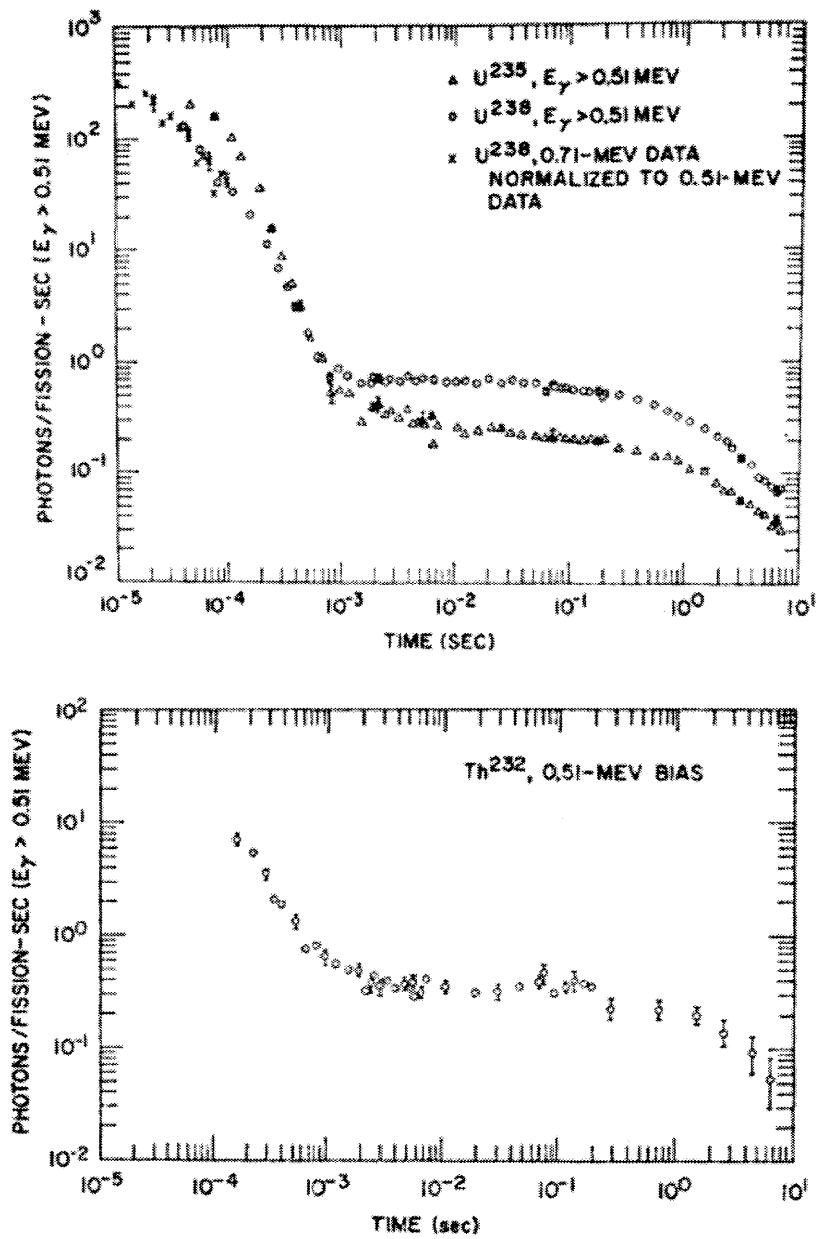


Figure 2-6. Delayed gamma rays with energies greater than 0.51 MeV from photofission of ^{233}U and ^{235}U (top), and ^{232}Th (bottom). Figures are taken from Walton et al.²⁶

2.4. Detector specifications and requirements

The detectors for long-range active interrogation techniques have to possess special features, including large area available for detection (large solid angle), scalability, relatively low cost, robustness, transportability, and low operational hazards. National security applications of detection have imposed additional demands on gamma and neutron detection. For instance, a detector located near the LINAC must be able to withstand significant radiation fluence without experiencing degradation from an intense gamma background. In addition, there are currently many restrictions associated with neutron detectors. Thus, alternative materials and detector designs must be pursued for neutron detection.

2.4.1. Scintillator near beam

One of the main concerns about detectors in active interrogation applications is using them in a high-intensity accelerator beam environment. First, most materials exhibit radiation damage when they are operated near high-intensity beams. Second, materials such as scintillators can experience a large light “flash” from such accelerators, which can blind them for milliseconds or more. In active interrogation applications, fast recovery from the LINAC is essential as timing can provide important information about the target.

2.4.2. Shortage of He-3

^3He is a byproduct of tritium production for nuclear weapons. Tritium decays into ^3He through β^- decay with a half-life of 12.3 years. One of the major applications of ^3He ,

besides the prediction of how much nuclear weaponry was produced in the world, is in detection of neutrons. Currently, only the U.S. and Russia are producing significant amounts of ^3He , and the global amount of available ^3He stock is about 20 kliter/year.³¹

Most SNM emits detectable quantities of neutrons indicating that prompt neutron detection can have a significant impact on material characterization. In addition, most detector systems must have an ability to discriminate between neutrons and gamma rays. ^3He would be an ideal candidate for a neutron detection system in active interrogation application, if it were not for its limited availability. National security applications require a system that can detect neutrons, but be widely available to cover a large solid angle. This means a safe, inexpensive, and readily available detector medium is required.

Practically, the only other commercially available option for large-area detection is ^{10}B and ^6Li tubes. Compared to ^3He detector, ^{10}B and ^6Li have about 70% and 17% of the absorption cross section of ^3He , respectively. ^{10}B detectors come in two most common varieties: $^{10}\text{BF}_3$ gas-filled detectors and ^{10}B -lined proportional counters. While $^{10}\text{BF}_3$ detectors provide excellent neutron-gamma separation, the lower cross section of ^{10}B and inability to operate at pressures close to atmospheric result in significantly lower efficiency than ^3He . In addition, $^{10}\text{BF}_3$ detectors operate at high voltages, and the gas is toxic creating transportation and operation hazards. The efficiency of ^{10}B -lined tubes is even lower than $^{10}\text{BF}_3$ detectors. However, there are no operational or health hazards associated with such tubes.

2.5. Cherenkov detectors

The focus of this research is on the development of non-traditional nuclear security detectors based on existing expertise with Cherenkov high-energy particle detectors. Cherenkov-type counters can fulfill the requirements of novel detection

systems for active interrogation applications. Cherenkov detectors have the ability to work in an intense low-energy background, for example near a linear accelerator. Cherenkov light pulses are extremely short, often sub-nanosecond, and do not possess the decay times associated with scintillators, which have very long decay times and as a result are essentially blind during the pulse (time scale of microseconds) and often for a long time afterward (time scale of milliseconds). Cherenkov detectors have inherent low energy sensitivity cutoff due to the threshold nature of Cherenkov light. In many active interrogation systems using electron accelerators, the bulk of the background from scattering is often below the threshold of the Cherenkov detector. In addition, such detectors can use almost any medium as a detector body, as long as light transparency is ensured. Water-based Cherenkov detectors are inexpensive to manufacture, and a variety of shapes can be configured.

One of the main problems with Cherenkov radiation is the limited intensity of the emitted light. More research regarding how to compensate for the effects of the low light emission is necessary. The light collection efficiency can be enhanced by increasing the number of photomultiplier tubes (PMTs) capable of detecting light, employing a highly reflective coating on the detector walls to preserve as much light as possible, and using water of high-purity to avoid photon absorption by impurities. Such enhancements are physical, and their applicability can be explored through experiment. In addition to the aforementioned enhancements, there is a possibility of exploiting inherent properties of Cherenkov radiation directionality and lack of self-absorption to enhance the light collection and to reduce the background. If proven to work at lower energies, directionality would allow significant background rejection. In active interrogation application, a target location is directionally predicted, and the photon energy of interest is between 3 and 10 MeV. In this range, forward Compton scattering is dominant allowing for directionality exploration. As an alternative to directional methods of background rejection, wavelength-shifting (WLS) dopants can be used. Cherenkov light emission is maximized in the ultraviolet region, which is outside of the sensitive range of most PMTs. Because of the absence of self-absorption of the light in the detector

medium, WLS chemicals can enhance light in the PMT-sensitive region. Even though using WLS might be a faster path to background rejection, all of directional properties of Cherenkov light would be lost. It must be noted here that there is a difference between development of a total absorption counter (for example, for photon spectroscopy) and a directional counter (for enhanced background rejection) because multiple electron scattering will deteriorate directionality properties. In the current work, the focus is on the total absorption counter, and the Cherenkov directionality property is not used.

The choice of detector configuration depends on application. For active interrogation detection, resolution is not required and background rejection might be most important. For material characterization, spectroscopy is essential. Detection of gammas is straightforward through Compton scattering. It must be mentioned here that the detection of neutrons is possible by using dopants in the detector medium with high neutron capture cross sections. Gadolinium salts have been successfully used as dopants for neutron detection.^{20,32-35}

3. Cherenkov radiation phenomenon and its application to water-based detectors

Cherenkov radiation was first observed and described by A. P. Cherenkov in 1932.^{36,37} The original formal classical theory of Cherenkov radiation was developed by Tamm and Frank in 1937.³⁸ Extensive review of Cherenkov radiation history is provided by.³⁹

Cherenkov radiation is most well known as the phenomenon causing the blue glow in nuclear reactors and spent fuel pools. It is a response of matter to the motion of a charged particle traveling at a speed exceeding the phase velocity of light in that matter. Cherenkov light has unique properties distinguishing it from luminescence, which is the basis for the operation of scintillators: directionality, ultraviolet spectrum, and energy threshold. Unlike isotropic scintillation light, Cherenkov photons are directional along the axis of polarization. The light is emitted in the direction of the charged particle in a cone whose opening angle depends on the velocity of the particle and the index of refraction of the medium. The spectrum of light is continuous with a maximum of intensity in the ultraviolet region. Most importantly, Cherenkov radiation has a threshold character implying that only particles with particular speeds, which are greater than the speed of light normalized by the refractive coefficient of the medium, can create Cherenkov light in that medium as described by Equation 3-1.

$$v > c/n(\omega) \qquad \text{Eq. 3-1}$$

where n is refractive coefficient of the medium, and ω is angular frequency of the photon.

The threshold property of Cherenkov radiation also makes it an attractive tool in distinguishing between various particle types and energies using the correlation between the particle velocity and the amount of generated light. The threshold property of Cherenkov radiation makes it possible to significantly suppress low-energy background, for example from a linear accelerator in a close proximity, and to nearly eliminate high-energy background, for example cosmic neutrons, without adversely affecting the response of the detector in the desired energy range, whereas for scintillators, energy discrimination must be performed as post-processing.

3.1. Properties of Cherenkov radiation: threshold and directionality

The derivation of the physics of Cherenkov radiation can be approached using classical electrodynamics and quantum mechanical derivation. Appendix A introduces the ideal case originally derived by Tamm and Frank using classical electrodynamics theory. A summary of physics of Cherenkov radiation phenomenon is briefly reviewed here.

Consider a charged particle moving from left to right, as illustrated in Figure 3-1, through a polarizable medium. The particle is a source of energy emitted in the form of electromagnetic waves, creating a non-vanishing Poynting vector. The particle produces spherical wavefronts moving at characteristic speed defined by their wavelength and frequency. If the particle is moving at a speed close to the speed of wavefront propagation in the medium, then the particle simply moves with its own spherical wavefronts as shown in the top diagram of Figure 3-1. The propagation speed of the wavefront

is equal to the phase velocity of light in the medium c/n . When the speed of the particle increases *beyond the phase velocity of light*, the waves radiated from the points of motion travel a shorter path than the particle itself in a given time period t as shown in the bottom diagram of Figure 3-1. All of the spherical waves have a common envelope with the particle being at the apex. According to Huygens principle, the surface of the envelope is the front of the wave radiated by a charged particle. Correlating the angle of the front θ with the speed of the particle, we get Equation 3-2.

$$\cos\theta = \frac{c}{n(\omega)v} \quad \text{Eq. 3-2}$$

Equation 3-1 can be obtained from Equation 3-2 by imposing the requirement for $\cos\theta$ to be less than unity for all real angles.

The observation that the emitted radiation is perpendicular to the wavefront explains the directionality of Cherenkov light. Note that the refractive index $n(\omega)$ depends on the frequency of the photons traveling through medium. This leads to the direct dependency of the angle θ on the frequency of the wave. The refraction coefficient for photons in the blue part of the spectrum is larger than the refraction coefficient for the red part.

Figure 3-2 illustrates the effect of threshold kinetic energies for Cherenkov radiation for different particles in various media. Note that the threshold kinetic energy is in units of rest mass. Thus, the phenomenon of Cherenkov radiation is independent of particle mass and is a function of the refractive coefficient of the medium.

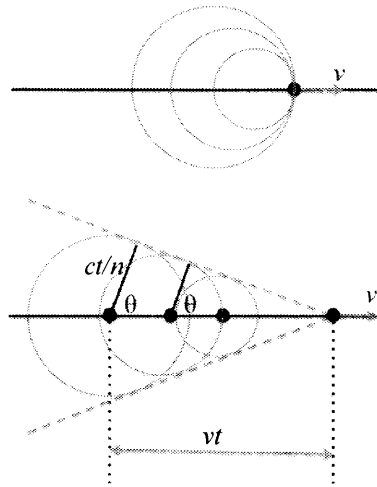


Figure 3-1. Schematic of charged particle's motion at the speed of light in the medium (top) and faster than phase velocity of light (bottom).

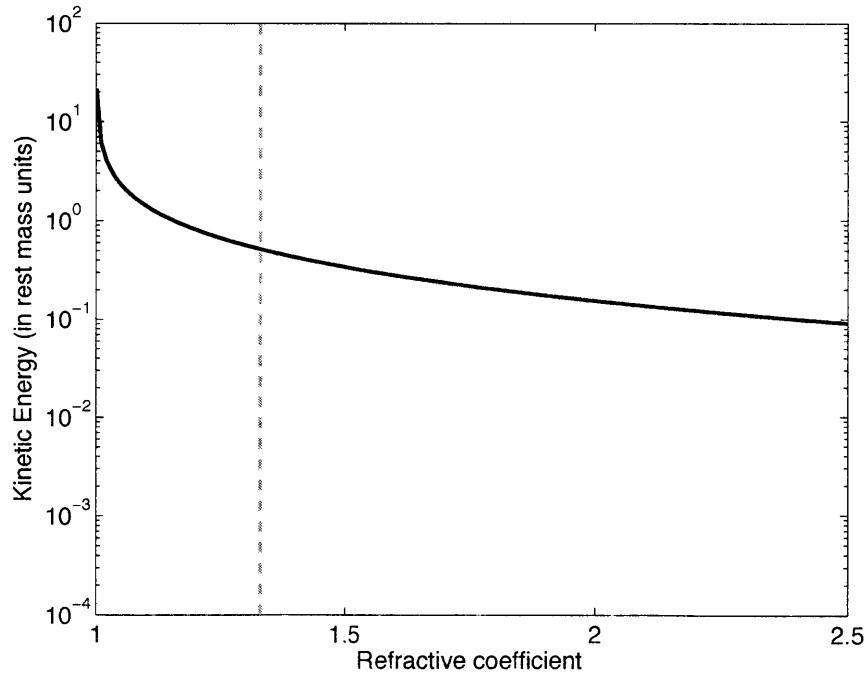


Figure 3-2. Dependence of threshold kinetic energy (in units of rest energy, $E_0=mc^2$) on refractive coefficient of the medium. Dashed line illustrates the case for water ($n=1.33$).

Table 3-1. Threshold kinetic energy for various particles.

| Particle | Rest energy (MeV) | Threshold kinetic energy (MeV) | | |
|----------|-------------------|---|--|---|
| | | n=1.003 (gas) $\beta=0.997$ $KE_{th}=12E_0$ | n=1.33 (water) $\beta=0.75$ $E_{th}=0.52E_0$ | n=2.42 (diamond) $\beta=0.41$ $E_{th}=0.1E_0$ |
| Electron | 0.511 | 6.10 | 0.26 | 0.05 |
| Muon | 106 | 1265.53 | 54.78 | 10.40 |
| Proton | 938 | 11198.76 | 484.72 | 92.06 |

3.2. Light yield and spectral distribution

As was pointed out in the previous section, Cherenkov light has two major properties that serve to its advantage in detector applications: threshold and directionality. However, the big problem of Cherenkov radiation is the modest light output. Moreover, Cherenkov light is concentrated in ultraviolet range, the region in which most photomultiplier tubes (PMT) have rather low efficiency. The famous formula of Cherenkov light yield per unit path per unit wavelength interval originally derived by Frank and Tamm is shown as Equation 3-3. Details of the derivation of Equation 3-3 are provided in Appendix A.

$$\frac{d^2N}{dx d\lambda} = \frac{2\pi\alpha}{\lambda^2} \left(1 - \frac{1}{\beta^2 n^2}\right) dx d\lambda \quad \text{Eq. 3-3}$$

where α is the fine structure constant, and β is the particle's velocity. In this equation, it was assumed that the refraction coefficient is constant with photon wavelength. In fact, such assumption is fairly accurate for water. Integrating Equation 3-3 over a wavelength region of $\lambda_1 - \lambda_2$ Equation 3-4 is obtained.

$$\frac{dN}{dx} = \int_{\lambda_1}^{\lambda_2} \frac{2\pi\alpha}{\lambda^2} \left(1 - \frac{1}{\beta^2 n^2}\right) dx d\lambda = 2\pi\alpha \sin^2\theta \left(\frac{1}{\lambda_2} - \frac{1}{\lambda_1}\right) \quad \text{Eq. 3-4}$$

Here we rewrote the $\left(1 - \frac{1}{\beta^2 n^2}\right)$ as $\sin^2\theta$ by employing Equation 3-2. To illustrate the typical light yield, substitute 400-700 nm, which corresponds to a typical PMT sensitivity region, for the limits of integration in Equation 3-4:

$$\frac{dN}{dx} \approx 490 \sin^2\theta \text{ photons/cm} \quad \text{Eq. 3-5}$$

3.3. Review of WCD applications

Cherenkov detectors have been primarily used in particle physics applications, often in neutrino physics and dark matter physics. Since the discovery of Cherenkov radiation in 1934 and the development of photomultiplier tubes capable of recording light splashes as low as a single photon, Cherenkov detectors have been employed to discover

and study various types of radiation, from low-energy gammas to cosmic showers and neutrinos. Some of the well-known high energy physics application include Super-Kamiokande in Japan and Milagro near Los Alamos, New Mexico.

Super-Kamiokande is an underground neutrino observatory which consists of a cylindrical stainless steel tank holding 50,000 tons of clean water. The detection of Cherenkov photons is done through 11,146 20" photomultiplier tubes supplied by Hamamatsu. Milagro was a ground-based Cherenkov telescope for gamma and cosmic ray detection. The pool consisted of 5 million gallons of water with three layers of PMTs.

The high-energy particle detection community was first to appreciate the special role of Cherenkov detectors. However, the technology can also be considered for reactor safeguards and monitoring as well as remote detection and identification of special nuclear material. One of the greatest challenges of remote power monitoring or standoff detection is the limited number of events because the intensity of radiation decreases as the inverse of the square of the distance. This means that the detector design becomes a compromise between the efficiency and the footprint.

At high energies and in large (kiloton to multi-kiloton scale) water detectors, Cherenkov imaging is a well-proven technique. For example, Cherenkov detectors are excellent electromagnetic calorimeters in high-energy physics application. Large detectors are designed to do antineutrino astronomy in the energy range of 10^{10} - 10^{18} eV. At lower energies relevant for nuclear material screening or reactor monitoring, the implementation is more difficult, and still remains to be demonstrated as a practical approach. Key research and development considerations of this application include suppressing background, studying effects of dopants, and lowering energy thresholds. Monte Carlo studies and experimental verification of this effect can help inform the design of low energy gamma and neutron detectors.

3.4. Gamma detection with water Cherenkov counters

Gamma rays are uncharged particles; thus, the only way Cherenkov light can be created by these particles is through indirect interaction of gamma rays with a charged particle. One of most common reactions for Cherenkov light production is through Compton interaction of gamma rays with electrons. Compton interactions are preferred to other reaction, for example photoelectric absorption and pair production, for high-energy (greater than 0.5 MeV) gamma rays.

Energy threshold for gamma detection can be related to Compton interaction. Recall from Section 3.1 that the Cherenkov energy threshold for electrons in water is 262 keV. Using Compton scattering formula, we can calculate the Cherenkov energy threshold for gamma rays to be 420 keV. Figure 3-3 illustrates the dependence of threshold energies on refractive index. Note, that as the refractive index approaches 1.0 (gases), the energies approach infinity asymptotically.

Another question is whether directionality of Cherenkov light can be preserved in gamma detection. In Compton scattering, when gamma energy is above 1 MeV, the scattering of electron is forward-peaked. Higher energy of the photon leads to anisotropic scattering of the electron. Thus, directionality of high-energy gammas can be translated into directionality of Cherenkov light. Figure 3-4 illustrates the dependence of the scattering angle of the Compton electron on the energy of the incident gamma ray.

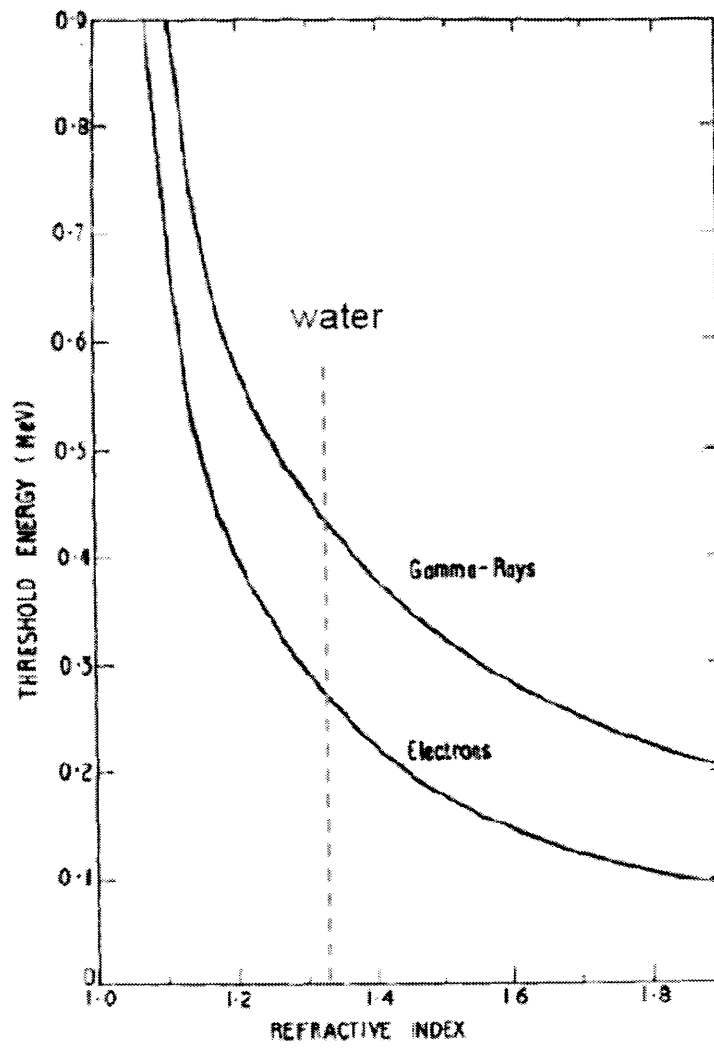


Figure 3-3. Comparison of threshold energies for electrons and gamma rays. Figure is taken from Sowerby.⁴⁰

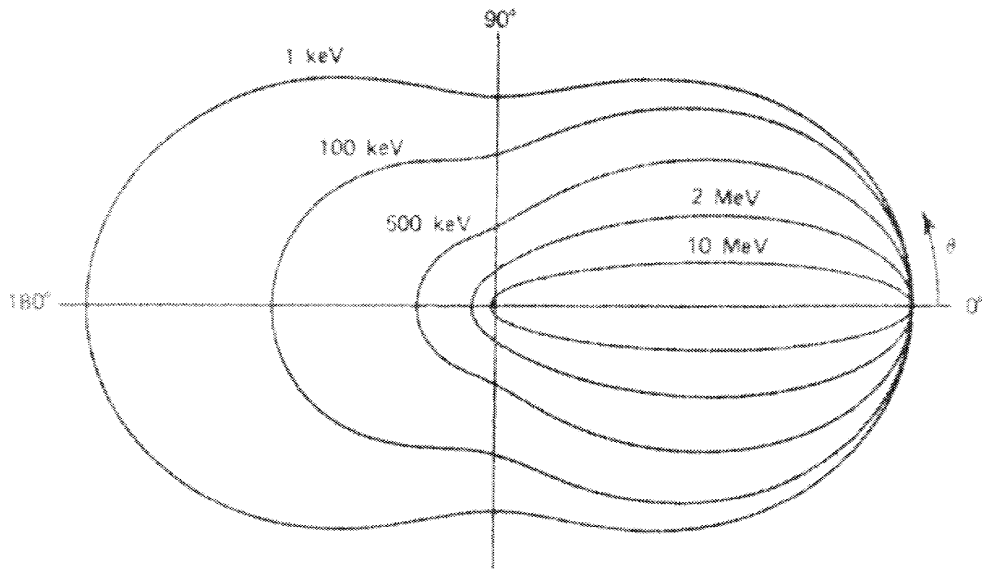


Figure 3-4. Polar plot of Klein-Nishina formula. The plot shows dependence of scattering angle of the electron on energy of the incident gamma ray. Figure is taken from Knoll.⁴¹

4. Modeling of the detector with Geant4

In order to determine whether Water Cherenkov Detector is suitable for long-range gamma detection as well as for detector optimization purposes, a full detector simulation has been developed in Geant4. This chapter provides a summary on the code capabilities and major findings of the detector optimization studies. Using Geant4, all relevant physical interactions are modeled in detail including nuclear and electron interactions and optical performance of the detector components. Specific examples and details of the code are provided in Appendix C.

4.1. Overview of the code capabilities

The Geant4^{42,43} toolkit provides a flexible framework for the simulation of particle transport and interaction with matter. The software suite is most well known by its application in high-energy physics, medical device simulation, and radiation detection. The acronym comes from GEometry ANd Tracking. One of the main advantages of using Geant4 over other toolkits (for example, MCNP) is the flexibility of its kernel, which allows for construction of detector geometries of arbitrary complexity, construction of particles and physics processes, and setup of application-specific sensitive detectors and counters. Geant4 is based on C++, and the source is freely available⁴⁴. Geant4 is a Monte

Carlo method-based code, which means that high-precision calculations require a large number of simulation histories.

Generally, the following steps are followed when the code is used for modeling and analysis. The mandatory classes^d that must be overridden by the user are provided in parentheses.

- The particles of interest are specified, for example gamma rays or neutrons (G4VUserPhysicsList).
- The processes which the particles will undergo are described (for example, Cherenkov or scintillation).
- The geometry of the system is specified (G4VUserDetectorConstruction virtual class).
- The materials are assigned to each component. Geant4 allows for specific material definition including optical properties.
- Sensitive detector is defined. Sensitive detector is a useful feature of Geant4 which allows the user to provide his or her own implementation of the detector response to a physical interaction of radiation with the sensitive volume.
- Primary events are generated. Geant4 provides a user with multiple options to generate a primary event. Examples include using a particle gun which is able to generate momentum and position, but does not provide any sort of randomizing, or specifying a general particle source which allows control of spectrum, spatial and angular distribution, and inclusion of many sources (G4VPrimaryGeneratorAction).
- Particle transport is implemented including secondary event simulation.
- The results of an event are either stored or output.

^d Geant4 is based on C++, and a class is C++ concept of a data structure, which is capable of holding both data and functions associated with it.

There are also a number of user-specified classes that are not mandatory but often necessary to specify more complex settings. Some of these classes are necessary if a user wishes to track particles throughout the detector and to record select events.

When applied to Cherenkov detectors, Geant4 has the capability of triggering and tracking optical processes, which include the generation of photons by scintillation process, Cherenkov photon production by a charged particle, and transition radiation. Rayleigh scattering, bulk absorption and reflection-refraction media-boundary interactions are also part of the optical processes and are wavelength-dependent. Conceptually in Geant4, a photon is qualified as "optical" if its wavelength is much greater than the interatomic spacing of a simulated material.

4.2. Modeling of geometry and materials

The detector was simulated with Geant4 (version 4.9.3). A schematic of the model geometry along with sample particle tracks is shown in Figure 4-1. Modeling of geometry in Geant4 consists of defining two main types of volumes: the "World" volume and the daughter volumes. The purpose of the "World" volume is to simulate the environment settings (for example, the laboratory). This volume also contains the reference frame for the rest of the model. All other components are defined with respect to the center of the "World" volume.

When the geometry of the volumes is defined, every component of the system is assigned a material. Geant4 allows a user to specify each material individually including isotopic composition of the elements or to select a predefined material or element from the library. This feature is especially useful when complex alloys are used in system components.

The initial geometry of the detector was selected based on the availability of the space in the interrogation system container and was later optimized to find the best compromise between spatial constraints and efficiency. The detector consists of an aluminum alloy body lined inside with a polypropylene shell with an attached reflector and filled with high-purity water. High reflectivity of the walls is achieved by using 0.5 mm thick diffuse reflector (Gore DRP). Six 8" hemispherical Hamamatsu R5912-02 PMTs with maximum quantum efficiency of 25% at 375 nm are located in the top portion of the tank facing downward.

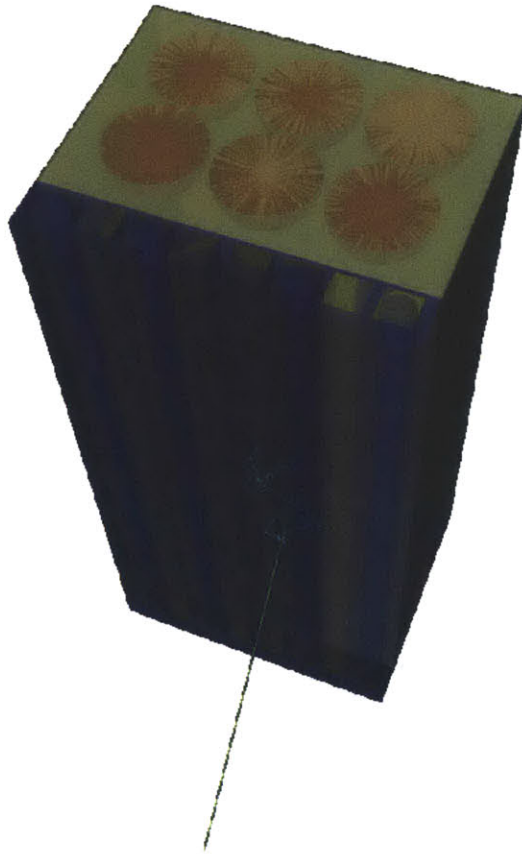


Figure 4-1. Detector model in Geant4.

4.3. Modeling of optical processes

One of the most important elements of the modeling of Cherenkov processes in Geant4 is the user-defined optical property of the simulated medium. Properties are generally expressed as a function of photon energy. Cherenkov photons are generated only in the material for which a refractive coefficient has been provided. In addition, bulk optical absorption has the ability to "kill" a photon. For this process, a detection medium, for example water, is assigned a wavelength-dependent absorption coefficient. Boundary processes possess certain flexibility, for example allowing the user to specify whether the optical surfaces are polished or rough and made out of dielectric or metal. Reflectivity of the surface can also be specified as a function of photon wavelength allowing for reflection, refraction or absorption of a photon.

4.3.1. Reflectivity of the walls

Reflectivity is generally differentiated between specular and diffuse. Specular reflection is a reflection from a smooth surface with the incident and reflected angles being the same. Diffuse reflectivity, also referred to as Lambertian, causes the incident light to scatter in many directions. Figure 4-2 illustrates the difference between specular and diffuse reflectors.

High-efficiency reflectivity of the walls is important for photon collection. A diffuse reflector Gore was chosen to surround the water medium because of its chemical stability, hydrophobic water resistance, lack of fluorescence, and highly Lambertian diffuseness. Figure 4-3 compares Gore DPR with various materials of similar reflectivity.

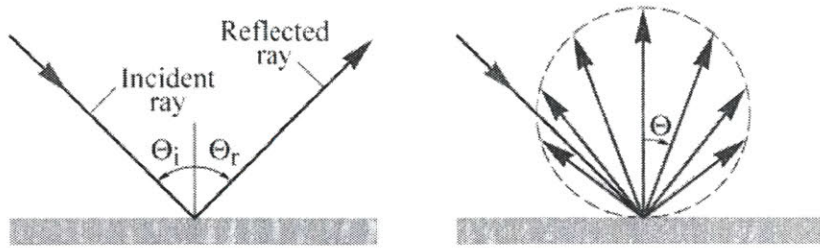


Figure 4-2. Specular (left) vs. diffuse (right) reflectivity. Figure is taken from Schubert.⁴⁵

The diffuse reflectivity was modeled as a function of photon wavelength. The photons bounce off the walls until they are either absorbed in water or structural materials or reach a PMT.

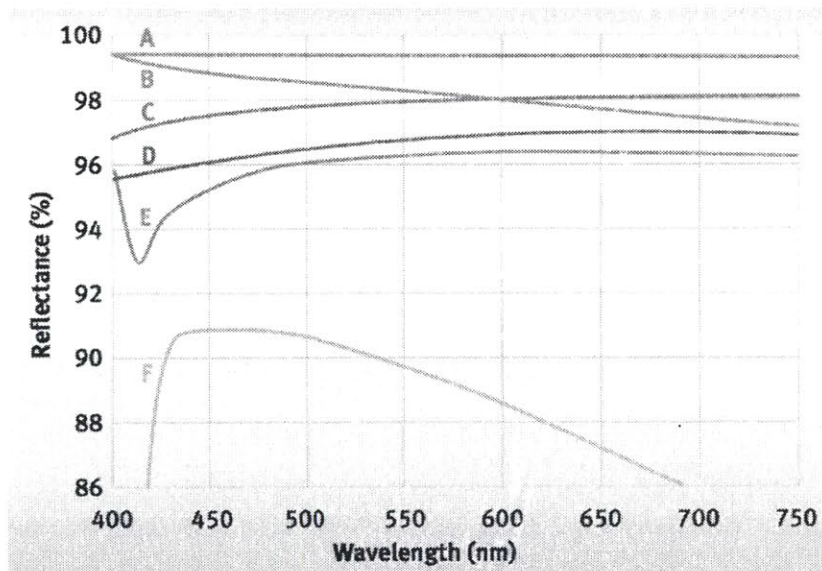


Figure 4-3. Comparison of reflectance of various materials. Curves A and B correspond to 3.0 and 0.5 mm Gore DRP, respectively. Curves C, D, E, and F stand for granular PTFE, barium sulfate, microporous polyester, and powder coating.

Figure is taken from Gore.⁴⁶

4.3.2. Water absorption coefficient

The optical quality of water can significantly affect the performance of a Cherenkov detector. Higher quality water results in collection of more Cherenkov photons. The optical quality of water can be evaluated by assessing its light transmittance. Light transmittance is defined as the ratio of transmitted (unabsorbed) to total intensity of incident light as shown in Equation 4-1.

$$T = \frac{I}{I_0} \quad \text{Eq. 4-1}$$

Light absorbance, $A = -\ln T$, can be related to the optical path of light, x , using Beer-Lambert law:

$$A(\lambda) = \sigma(\lambda)Nx \quad \text{Eq. 4-2}$$

where N is the number density of light-absorbing species in the medium and $\sigma(\lambda)$ is the absorption cross section of a single particle. Absorption coefficient is then defined as:

$$\alpha(\lambda) = \sigma(\lambda)N \quad \text{Eq. 4-3}$$

Absorption length is taken as an inverse of the absorption coefficient.

A literature survey has been conducted in order to estimate water absorption coefficient. The main conclusion is that there is no agreement in data between various sources. One of the most promising datasets was the one measured at Lawrence Livermore National Laboratory (LLNL). The LLNL water absorption curve along with three other datasets (Hale and Querry⁴⁷, Querry⁴⁸, and Smith and Baker⁴⁹) are shown in Figure 4-4. Comparison of LLNL curve with other datasets illustrates the spread in data regarding water absorption properties.

The assumed water absorption coefficient was modeled in detail and as a function of photon energy because it influences how many photons will be absorbed in the water. A quantum efficiency (QE) curve consistent with Hamamatsu R5912-02 PMT specifications was also plotted in Figure 4-4 as a function of photon wavelength to illustrate the overlap in QE and absorption length for various datasets.

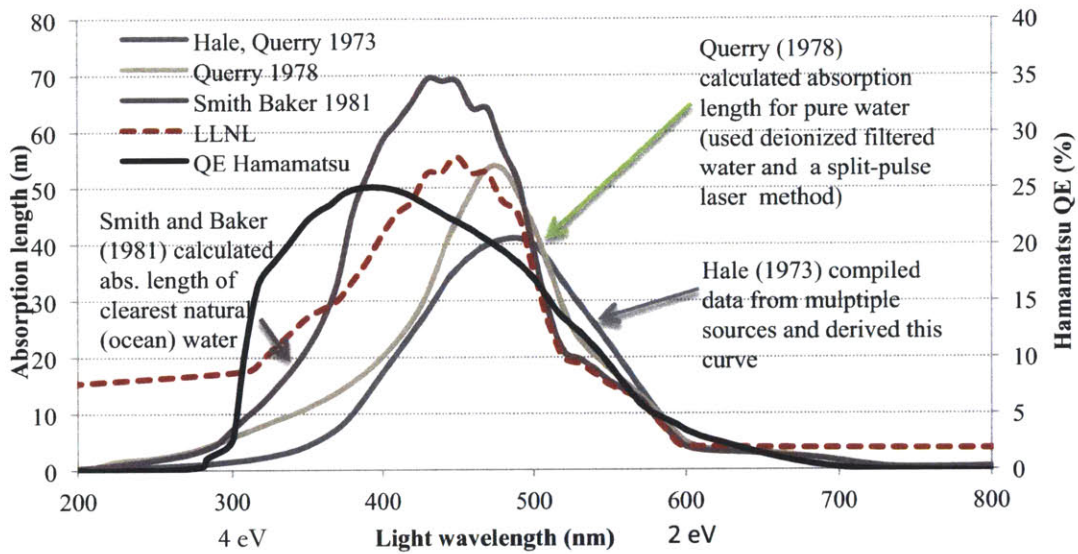


Figure 4-4. Comparison of water absorption lengths as a function of light photon wavelength. Quantum efficiency of Hamamatsu tubes is also shown (in black).

4.3.3. Effect of water absorption length and reflectivity of the walls on detector efficiency

The efficiency of the detector depends on how well the cascade gammas are converted into Compton electrons above the threshold for Cherenkov production (mainly

determined by the volume of the detector water) and how well the Cherenkov photons are detected by PMTs (depends on the water quality, reflectivity of the detector surface, PMT characteristics, and photocathode area). The main sources of uncertainty in our detector simulation are from reflectivity of the walls and quality of water. Figure 4-5 illustrates the effect of water absorption length (figures on the left) and wall reflectivity on the detector's response (figures on the right). The central figure shows the results with originally assumed conditions. The assumed water absorption length (LLNL) as shown in Figure 4-4 was scaled down in magnitude to simulate poorer water quality while keeping reflectivity at 99.5%. The reflectivity of the walls was decreased from 99.5% (3 mm Gore DRP) to 80% and 90% reflectivity while other parameters were held constant. It is evident that the double-peak feature of the pulse height spectrum disappears as the water absorption length and reflectivity of the walls decreased.

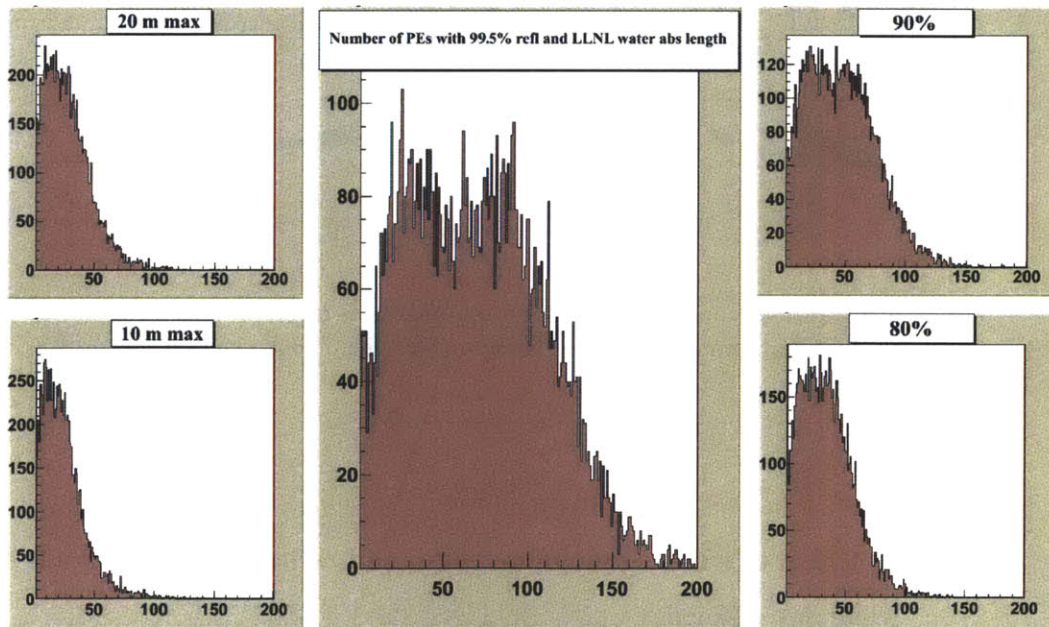


Figure 4-5. Effects of detector wall reflectivity and water absorption length on detector's response.

A reduction in the diffuse reflectivity of the liner can result in a decrease in the number of photons reaching the PMTs as can a decrease in the transmission length of the Cherenkov photons, particularly in the ultraviolet region of the Cherenkov spectrum. The exact effect depends critically on the geometry of the detector, the numbers and arrangements of the PMTs and the reflectivity of the walls and is shown in Fig. 4-6. The number of PMT hits by photons increases exponentially with reflectivity, but it increases nearly linearly (for non-large reflectance) with the number of tubes or even slower when reflectance reaches $\sim 90\%$. The reflectivity of the tank coating appears to be very important to the photon collection efficiency, and employing a reflector with higher efficiency can help reduce the cost of the detector associated with the PMTs.

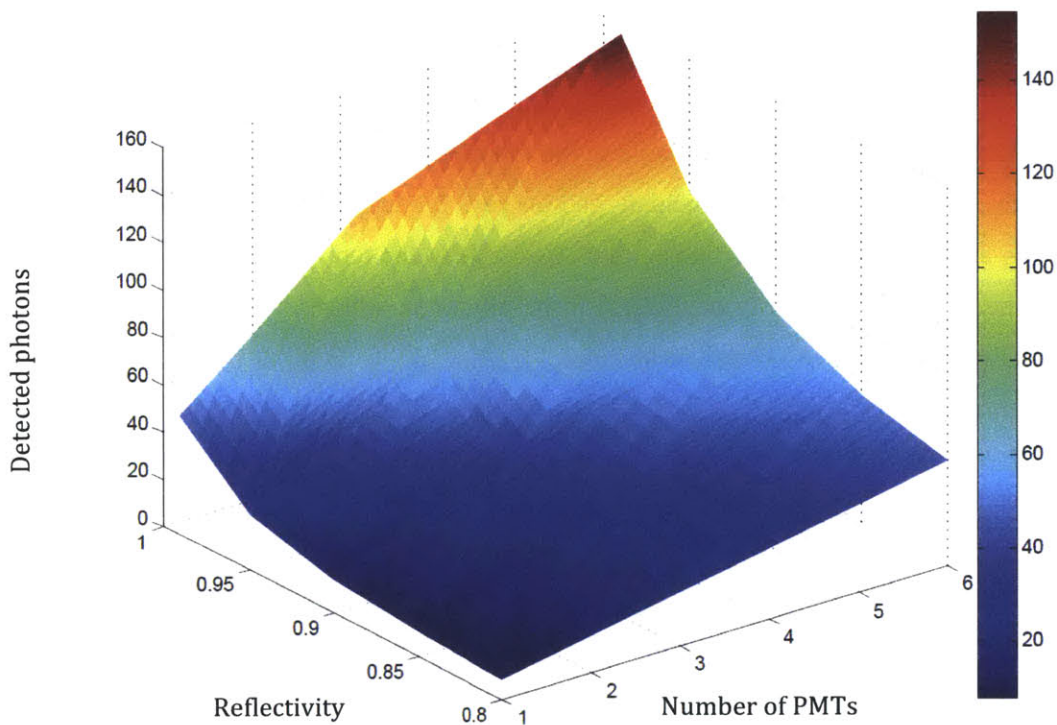


Figure 4-6. The number of Cherenkov photons detected as a function of the number of PMTs (1 to 6) and the diffuse reflectivity of the wall material (0.8 to 1.0).

4.4. Computational Results and Discussions

The results are organized into two following categories: (1) optimization of the tank design, and (2) simulation of tank performance with ^{232}Th . Additional simulation results, for example detector response to $^{241}\text{AmBe}$ source, are described in Chapter 7 as an illustration to the event reconstruction discussion.

4.4.1. Optimization of the tank design

Optimization studies were performed to determine the ideal dimensions of the detector tank. The size of the detector is a compromise between the volume of water available for the entering gamma rays to interact with electrons and to produce Cherenkov light and the space available in the interrogation system container. Figure 4-7 illustrates the percentage of the incident gamma rays producing Compton electrons with energies above the Cherenkov threshold (~ 270 keV) in the tank versus the depth of the tank. The depth of the tank was selected to be 50 cm, at which about 80% of incident gamma rays are expected to produce a signal.

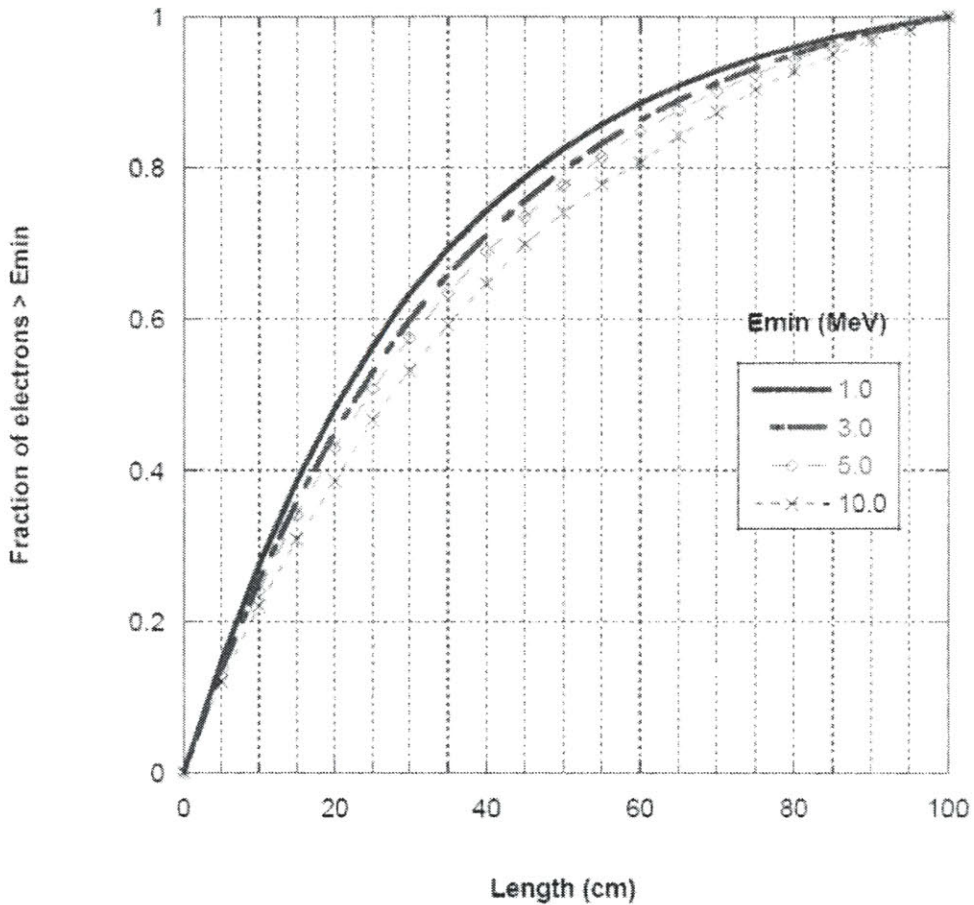


Figure 4-7. Fraction of gamma rays producing Compton electrons with energies above Cherenkov threshold vs. depth of the tank.⁵⁰

In the final design, the detector is capable of accommodating six 8" tubes facing downward. However, there are four ^{10}B neutron detectors that must be placed in front of or inside the tank. Two alternative concepts were proposed for consideration: (1) Centronics ^{10}B neutron tubes are placed inside the tank extending the depth dimension (in the direction of radiation) of the tank to 60 cm, and (2) Centronics ^{10}B neutron tubes are placed outside the tank in a block of polyethylene with tank depth dimension capped at 50 cm. Both concepts are illustrated in Figure 4-8. The reason for evaluation of two

designs was to determine if and how placement of ^{10}B tubes affects the performance of the Cherenkov detector. If the tubes are placed inside of the tank, an additional 10 cm of water (because of the extended tank depth) will result in increased production of Cherenkov photons by gamma rays. On the other hand, when the tubes are placed inside, Cherenkov photons will experience an increase in scattering off the tubes. Hence, more photons will be lost before they reach the PMTs.

Both scenarios were modeled in Geant4. As illustrated in Figure 4-8, in design 1 the ^{10}B Centronics tubes are placed inside with 1-cm-thick block of polyethylene in front of the tank; in design 2 the ^{10}B Centronics tubes are placed outside in a block of polyethylene. The block of polyethylene is capable of accommodating up to eight ^{10}B tubes. Four tubes were modeled; any additional slots are filled with air.

Two critical assumptions were made within the Geant4 model: (1) water absorption coefficient, and (2) Gore reflector performance. These two assumptions are important in evaluation of performance of both tank concepts. For water absorption length, LLNL curve shown in Figure 4-4 was used. The LLNL curve could be an overestimate of the actual Cherenkov tank water quality. In such case, a larger fraction of photons would be absorbed in the water, and placement of ^{10}B tubes inside of the tank would be undesirable. The second assumption is the reflectivity of the Gore liner. Inside of the tank is fully lined with Gore (in both concepts). In addition, in design 1 (tubes are inside) ^{10}B tubes are wrapped in reflector as well.

Comparison of the two designs was done using two metrics: (1) number of photoelectrons produced by an **incident** gamma, and (2) number of photoelectrons produced by an **interacting** gamma. The first metric, number of photoelectrons per incident gamma, is related to the detector's intrinsic efficiency. The number of photoelectrons per interacting gamma is a purely computational metric, which helps in conducting an assessment of how many photons interact with a photocathode when tubes are placed inside versus when tubes are not present in the tank.

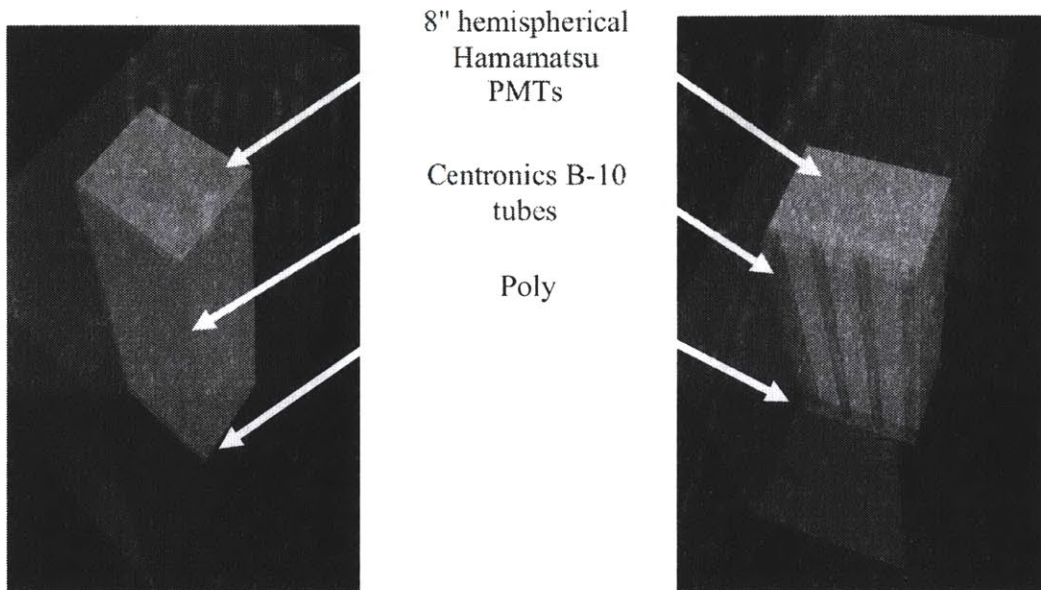


Figure 4-7. Two concepts of tank design. Left: design 1 - Centronics tubes are placed inside with 1-cm-thick block of poly in front of the tank. Right: design 2 - Centronics tubes are placed outside in a block of poly.

To summarize the metrics:

- When neutron tubes are inside, there is more water for gammas to produce Cherenkov photons through Compton interaction
- When tubes are outside, photons undergo fewer bounces and larger fraction of them makes it to the PMTs
- Two effects cancel each other resulting in basically same performance

A simulation of detector response using a planar source of monoenergetic gamma rays was completed for gamma rays of four various energies of interest: 3 MeV (lower

limit of interest), 5 MeV, 7 MeV, and 10 MeV. The results of analysis using the described metric are summarized in Table 4-1. Figure 4-9 illustrates spectral results for design #2 (tubes outside of the detection medium).

Table 4-1. Comparison of two designs.

| | Design #2: tubes are outside | | Design #1: tubes are inside | |
|--------------|---|--|---|--|
| Gamma energy | Number of Cherenkov photons produced in water (per gamma) | Average number of photo-electrons per gamma (all PMTs) | Number of Cherenkov photons produced in water (per gamma) | Average number of photo-electrons per gamma (all PMTs) |
| 3 MeV | 698 | 22 | 748 | 22 |
| 5 MeV | 1377 | 44 | 1493 | 43 |
| 7 MeV | 2012 | 64 | 2200 | 64 |
| 10 MeV | 2941 | 94 | 3154 | 91 |

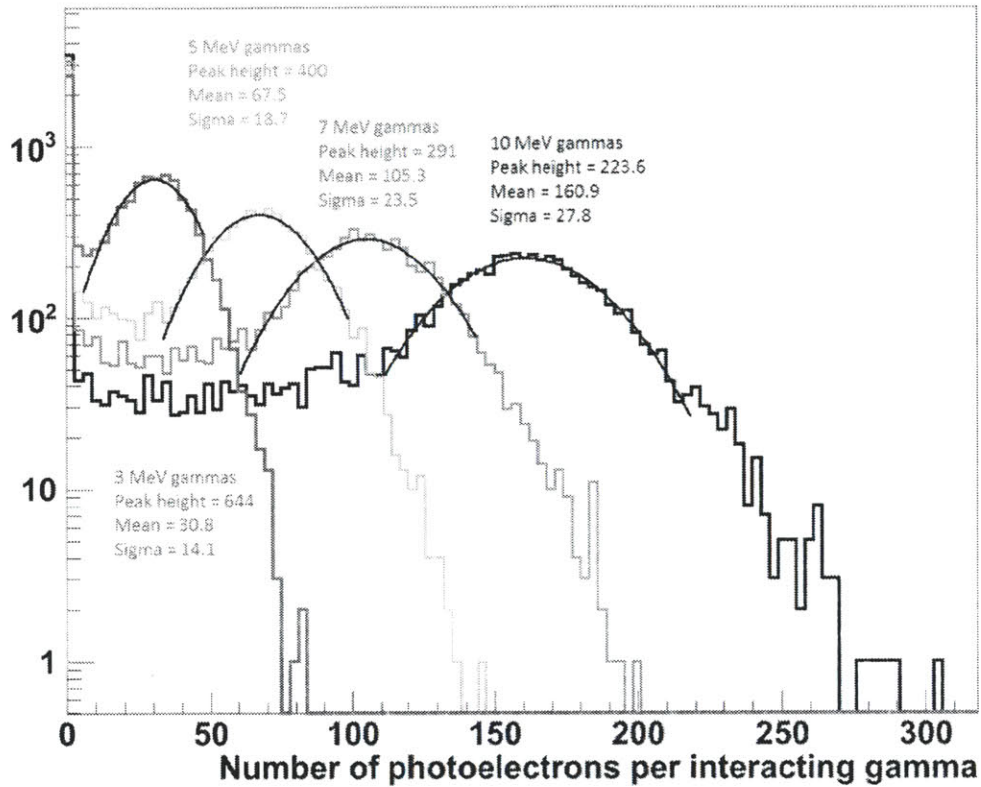


Figure 4-8. Change in detector (design 2) response as a function of gamma ray's energy.

Comparing the two designs, the differences in performance are not statistically significant. Design #2 shows very slightly better performance with respect to interacting gamma rays. Fewer bounces of the photons in the tank means that more photons will arrive to the photocathodes of the PMTs. Therefore, based on physics considerations, both designs are equally valid. However, if the properties of the water are poorer than assumed (recall the collection of data sets shown in Figure 4-4), design #2 would be preferred. In addition, if Gore DPR performance is not as good as quoted or degraded because of the structural materials in the tank, design #2 would also be preferred. Lastly, when ^{10}B tubes are inside the tank, there are concerns regarding humidity affecting their performance. Based on the above considerations, design #2 with ^{10}B tubes outside of the

tank was chosen as a final design for the experimental prototype water Cherenkov detector.

4.4.2. Simulation of ^{232}Th source

A ^{232}Th source was simulated to elucidate the response of the detector. The gamma spectrum of the actual source was experimentally obtained using a HPGe detector, and the results were converted into Geant4 input. The actual experimental spectrum is shown in Figure 6-1. The input to the Geant4 model is presented in Figure 4-10.

The Geant4 model of the detector-source system is illustrated in Figure 4-11. Note that the model of the source-detector system was approximated as closely to the laboratory setup as possible. The source was simulated as a slug of ^{232}Th with the dimensions approximately the same as the experimental source.

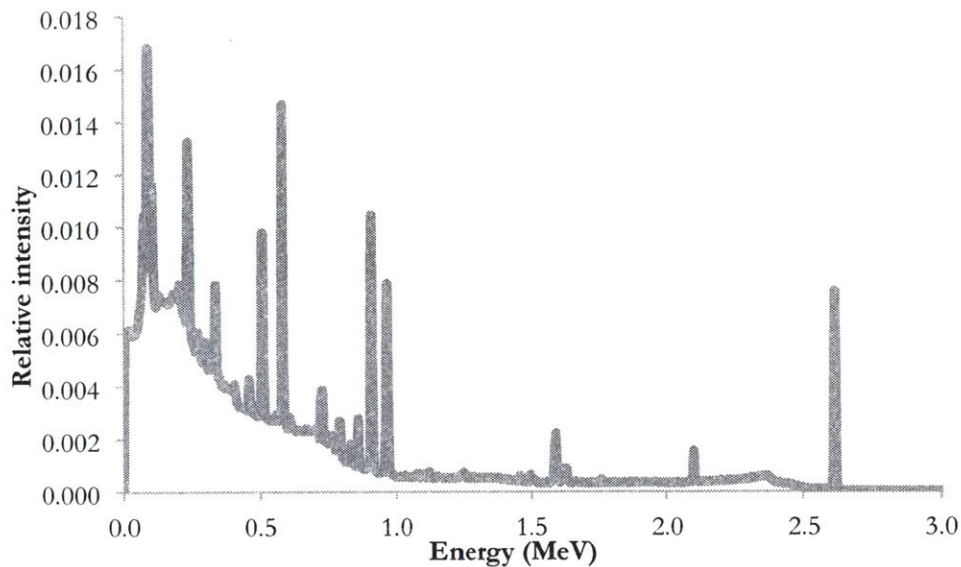


Figure 4-9. Spectrum of ^{232}Th as an input to the Geant4 model.

The source was simulated at four different distances away from the detector. The simulation was done for the same number of histories in all four cases. Such consistency allowed approximating the same “real” time of the experiment for all cases. As the source was moved away from the detector, the solid angle of the detector was decreased, and the number of interactions decreased as well.

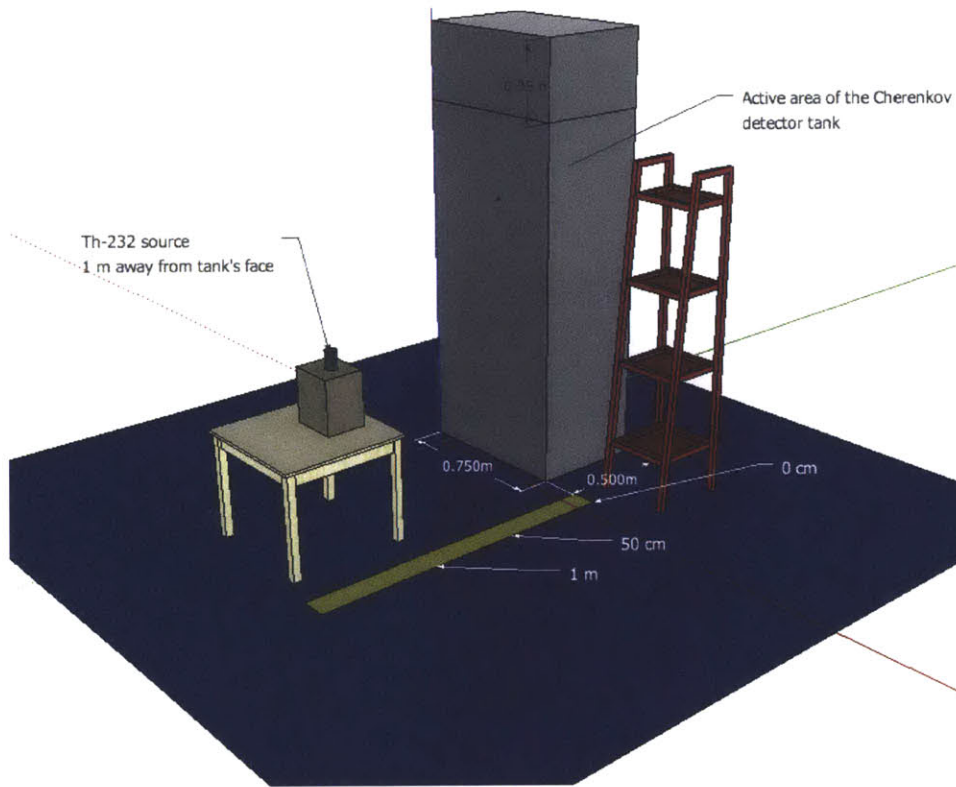


Figure 4-10. Illustration of the source-detector system.

Spectra for the same ^{232}Th source at various distances from the detector face is plotted in Figure 4-12. The abscissa is in number of photoelectrons ejected by Cherenkov photons after QE curve was applied to the photocathode. Note that the

ordinate is shown in log scale. Note that there is no definite peak as was observed in Figure 4-9. The energy spectrum of ^{232}Th has a desired high-energy peak (2.6 MeV), but other lower energy gamma rays are emitted. Thus, the spectrum of ^{232}Th appears continuous. ^{232}Th is an interesting illustrative case of the challenges active interrogation techniques are facing: material characterization by using continuous spectra feedback.

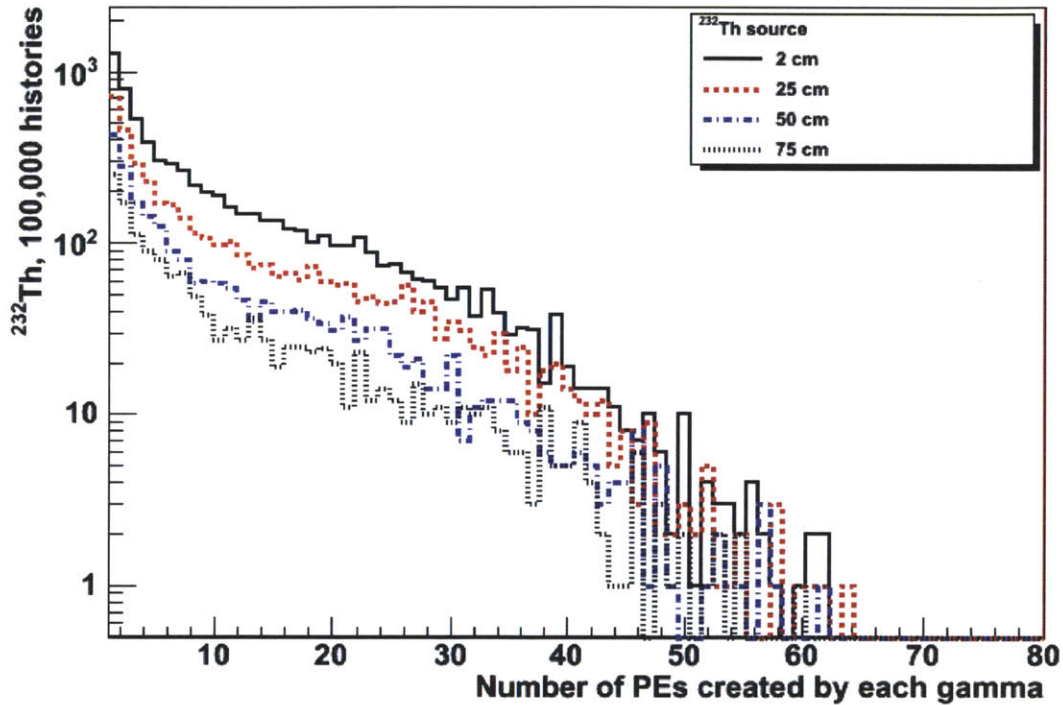


Figure 4-11. ^{232}Th spectra at various distances from the detector.

In order to further investigate the effect of low-energy part of the ^{232}Th spectrum on the Cherenkov detector response, the 2.6 MeV peak along with its Compton edge were removed from the simulation input. The results were subtracted from the spectra shown in Figure 4-12. Resulting curves are due to 2.6 MeV peak and its Compton edge

component. The results are shown for the 2 cm and 75 cm distances. The other two cases were removed for clarity. Note that the peak for the 2 cm case is very well pronounced. When the source is moved away from the detector, gamma rays have a smaller chance to deposit their full energy into the detector medium because of the decreasing solid angle. Thus, the other illustrated peak, when the source is 75 cm away from the face of the detector, appears smeared.

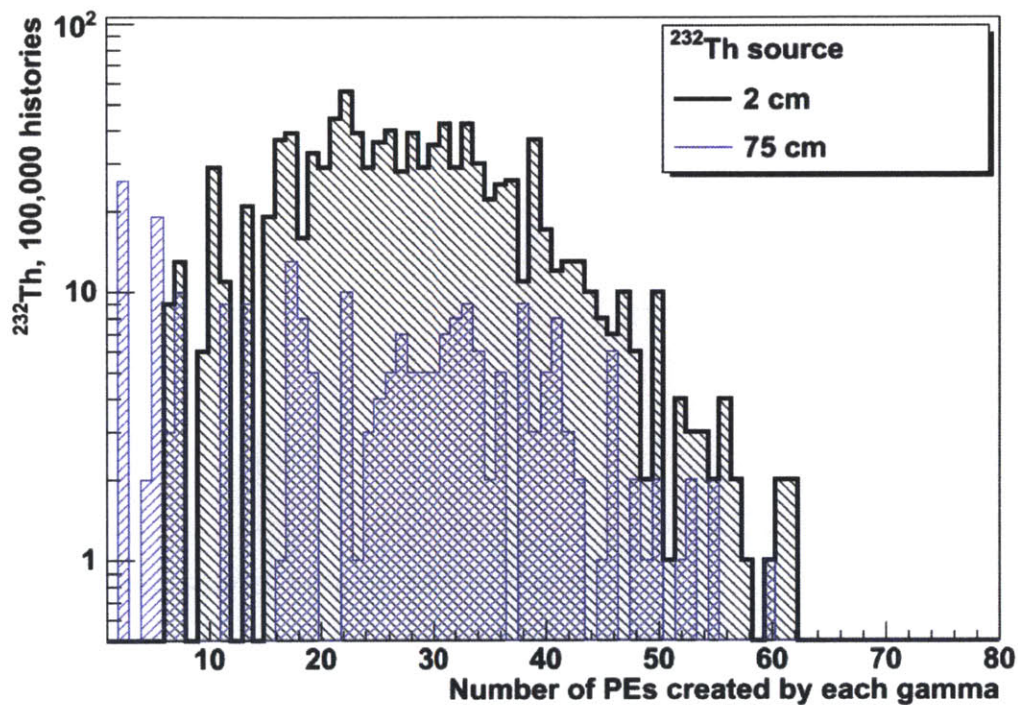


Figure 4-12. ^{232}Th source, peak only (other contributors subtracted).

Figure 4-14 shows the full spectrum from ^{232}Th source near the face of the detector (2 cm case) and the 2.6 MeV peak only after the other features were subtracted. It is evident from the plot that pulse height with 30 photoelectrons (p.e.) and above is the

result of 2.6 MeV gamma rays. Such peak deconvolution is useful in applying energy cuts in the actual detection when the radiation of interest is above a certain energy. For example, in the application, detection of gamma rays of 3 MeV and above is considered important to declare whether SNM is present in the target or not.

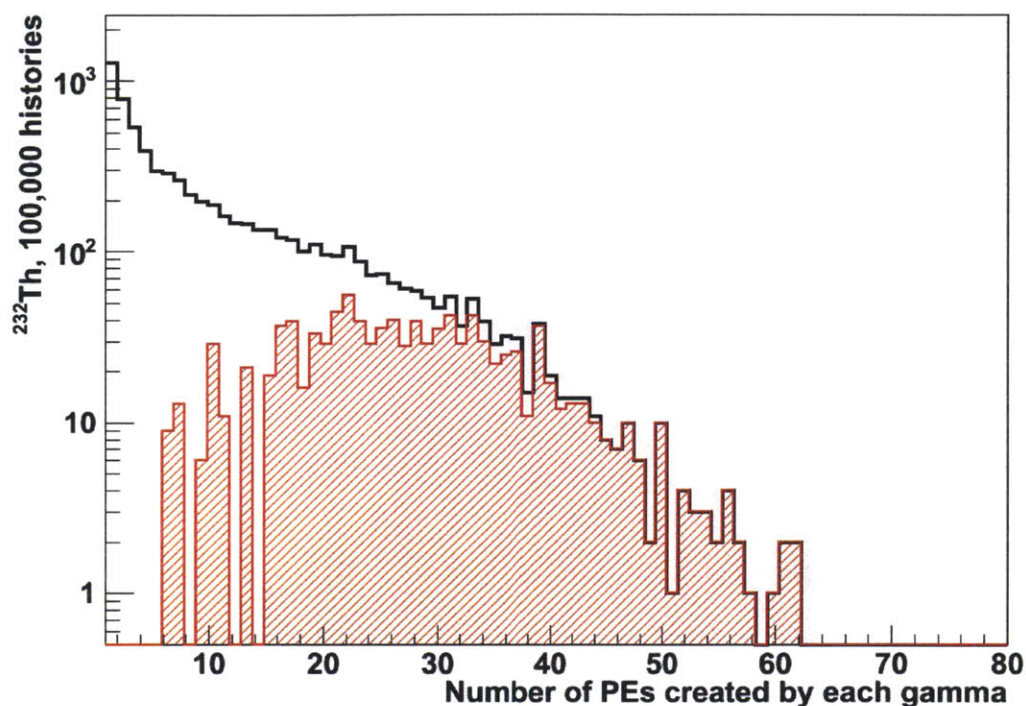


Figure 4-13. ^{232}Th source, full spectrum and peak only (other contributors subtracted).

Note from Figure 4-14 that even though the 2.6 MeV peak does appear as a peak, the full energy of a 2.6 MeV gamma ray corresponds to the right side of the peak. In a Cherenkov detector, discrete peak identification may not be possible due to poor resolution. Thus, energy cuts are applied. However, such an approach can lead to the removal of information related to the peak of interest. For example, if energy cut above 30 p.e. is applied, essentially half of the peak is discarded, and smaller signal is recorded.

Table 4-2 illustrates the effect of various energy cuts on the signal obtained from ^{232}Th source. The top part reports the results in terms of p.e., and the bottom part provides the percentage if full spectral integration was performed.

Table 4-2. Cuts applied to various distance cases.

| | >1 p.e. (total) | > 10 p.e. | > 20 p.e. | > 30 p.e. | > 40 p.e. |
|-------|-------------------------------------|-----------|-----------|-----------|-----------|
| | Integrated number of photoelectrons | | | | |
| 2 cm | 6890 | 2649 | 1289 | 516 | 140 |
| 25 cm | 3972 | 1554 | 800 | 332 | 98 |
| 50 cm | 2273 | 837 | 405 | 156 | 52 |
| 75 cm | 1441 | 522 | 257 | 120 | 40 |
| | Normalized to total | | | | |
| 2 cm | 100% | 38.4% | 18.7% | 7.5% | 2.0% |
| 25 cm | 100% | 39.1% | 20.1% | 8.4% | 2.5% |
| 50 cm | 100% | 36.8% | 17.8% | 6.9% | 2.3% |
| 75 cm | 100% | 36.2% | 17.8% | 8.3% | 2.8% |

5. Description of the Experimental Gamma Detector

Discussion of the detection methods and description of the experimental setup are provided in this chapter. This chapter focuses on the experimental aspects of data acquisition (DAQ). Two different acquisition chains are discussed: a traditional analog chain based on charge analog-to-digital converter (QDC) and a digital chain employing digital pulse processing algorithm (ADC). Review of the properties of PMTs, reflector and water as a detection medium and their effect on detector functionality are also discussed. All of the presented experimental results have been obtained with QDC data acquisition system unless stated otherwise.

5.1. Experimental Detector Design

The detector is composed of a light-tight 1/8-inch-thick aluminum body, which measures 0.75m x 0.5m x 2m, with a polypropylene insert for support of high efficiency (98.5%) diffuse reflector (Gore). Figure 5-1 illustrates the aluminum body of the detector as well as the insert.

The detector is filled with DI(deionized)-grade filtered water, which acts as a moderator for the incident radiation. Water quality is maintained through periodic checks and water re-circulation through an appropriate filtration system. Cherenkov photons are detected with six 8” hemispherical Hamamatsu PMTs. PMTs are calibrated using two

monoenergetic light emission diodes (LEDs). Figure 5-3 shows the water filtration and recirculation system (left) and LEDs positioned inside the detector (right).



Figure 5-1. Aluminum body of the detector (left) and polypropylene insert (right).

The PMTs are mounted to the ceiling of the tank. They are powered by a programmable external High Voltage (HV) power supply. The power supply provides and maintains desirable PMT gains. The tank cover is equipped with an array of waterproof feed-through connectors to bring in the high voltage and to take out the PMT signals. The PMT signals are processed through the front-end electronics, and the associated information is transmitted to the network through an HP Proliant USB server.

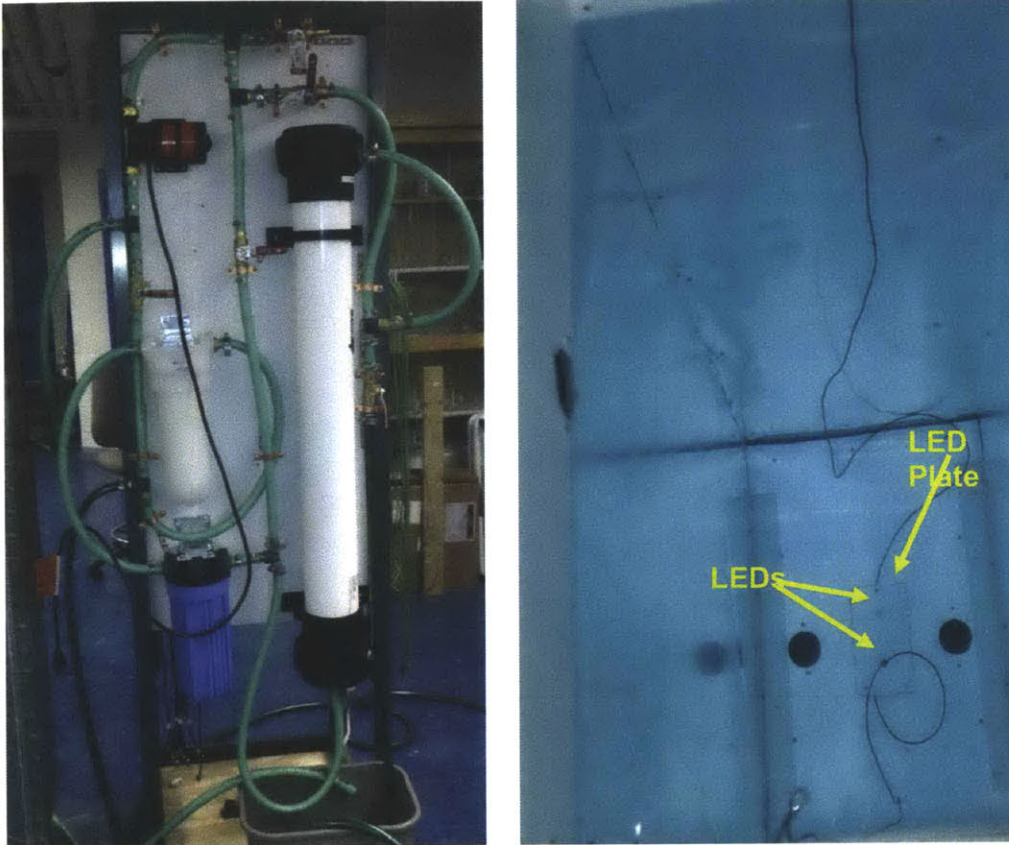


Figure 5-2. Water filtration and recirculation system (left) and LEDs positioned inside the detector (right)

5.2. Front-end electronics for fast signal processing

The purpose of front-end electronics in nuclear detection is to obtain and process the pulses acquired by the detector (in this case by the PMTs), to shape the time response of the system to process event rate and time of arrival information, and to push the data to

the server for further analysis.⁵¹ In case of the WCD, the quantities of interest are the energy and timing of the event. Figure 5-4 illustrates the principle of signal acquisition and processing.⁵² The sensor (PMT) converts the energy of a photon into an electrical signal. The magnitude of the signal is proportional to the charge deposited by the initial radiation and is subject to statistical fluctuations. In addition to statistical noise, the electronics noise contributes to the data fluctuations. One of the important elements of the data acquisition system is a digital logic unit that is capable of triggering on coincidence between data channels. Such coincidence triggering can be used to reduce the electronics noise.

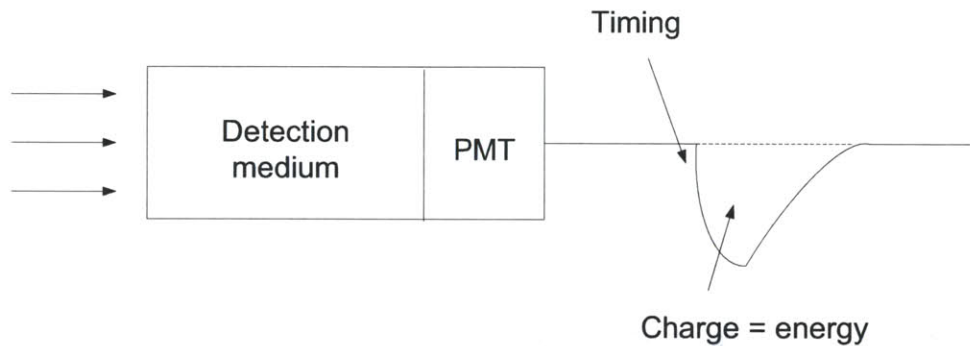


Figure 5-3. Electrical pulse generated by a detector. Figure is adopted from Tintori.⁵²

5.2.1. Electronics based on QDC

The original data acquisition setup for the detector was based on an analog v792 QDC. The QDC setup was used for preliminary testing of the detector performance. The QDC is based on charge integration and requires a gate signal in order to define an integrating window. Wiring diagram for QDC is shown in Figure 5-5.

In this particular application of QDC, the gate signal is not known in advance and must be generated by splitting a pulse from the PMTs into a prompt signal and a delayed signal, as shown in Figure 5-6. The prompt signal is the original signal from PMTs. The delayed branch of the signal arrives late compared to its prompt analog pulse because it is sent through a long cable. The prompt signal is sent through a low-level discriminator (LLD), CAEN v814, which only responds to pulses with amplitude higher than a certain threshold value. The advantage of using a LLD is in its ability to block a low-level noise. “Good” pulses, which are above the threshold, act as triggers. The output of the LLD is then sent to the field-programmable gate array (FPGA) and a scaler CAEN v830. The delayed signal is fed directly into the QDC.

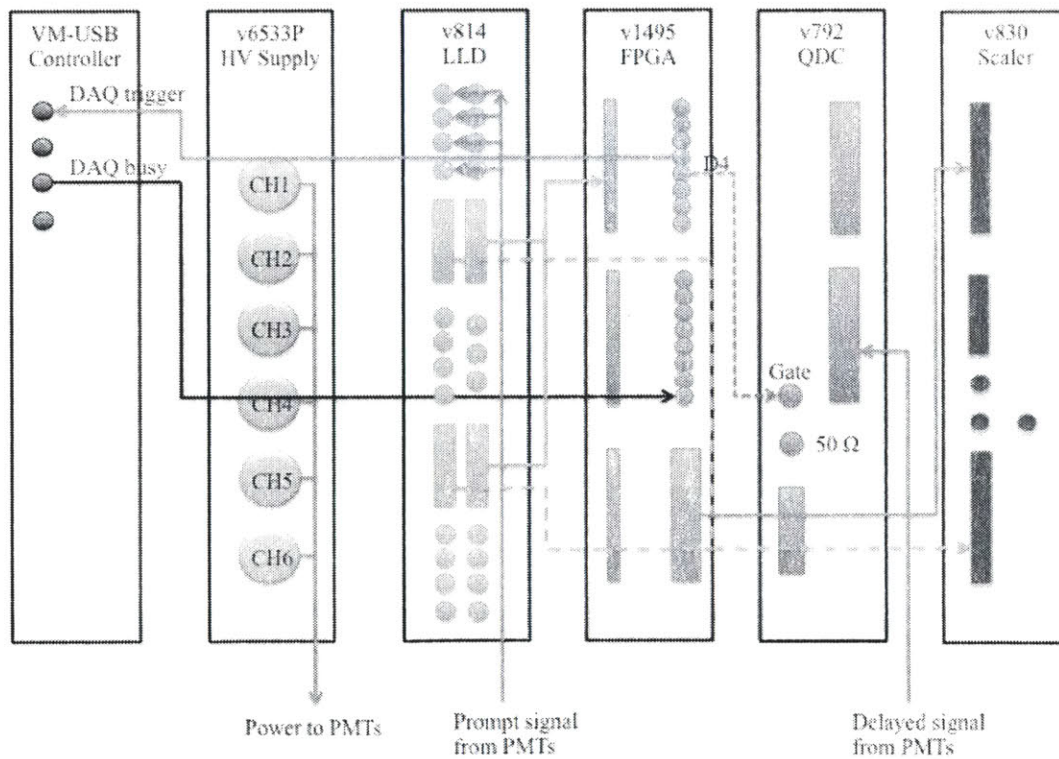


Figure 5-4. Wiring diagram for QDC.

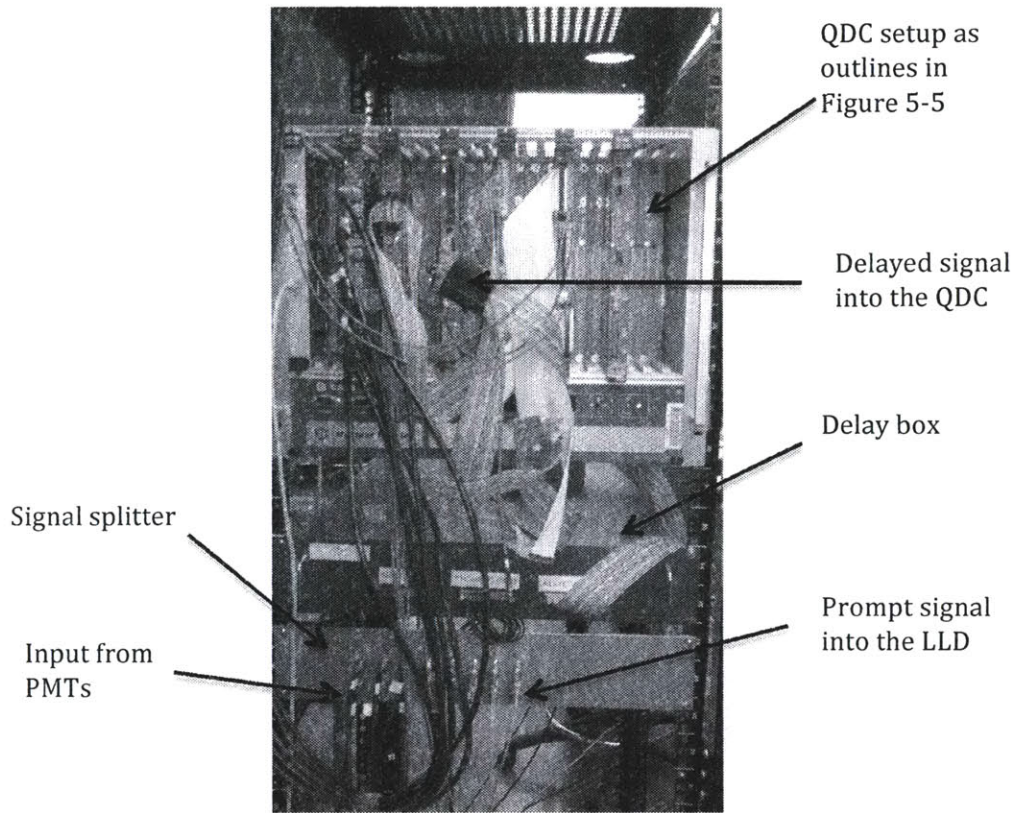


Figure 5-5. Data acquisition setup.

Field-Programmable Gate Array

The FPGA handles all logic necessary to recognize a valid event and to trigger data acquisition. FPGA is a collection of digital gates that can be configured to do a number of things. Specifically, v1495 houses three LVDS ports and three user-customizable mezzanine card slots. The cards used in WCD DAQ are two A395D (8 NIM/TTL input/output channels) residing in slots D and E and a A395B (32 LVDS output channels) residing in slot F. The block diagram of v1495 is shown in Figure 5-7.

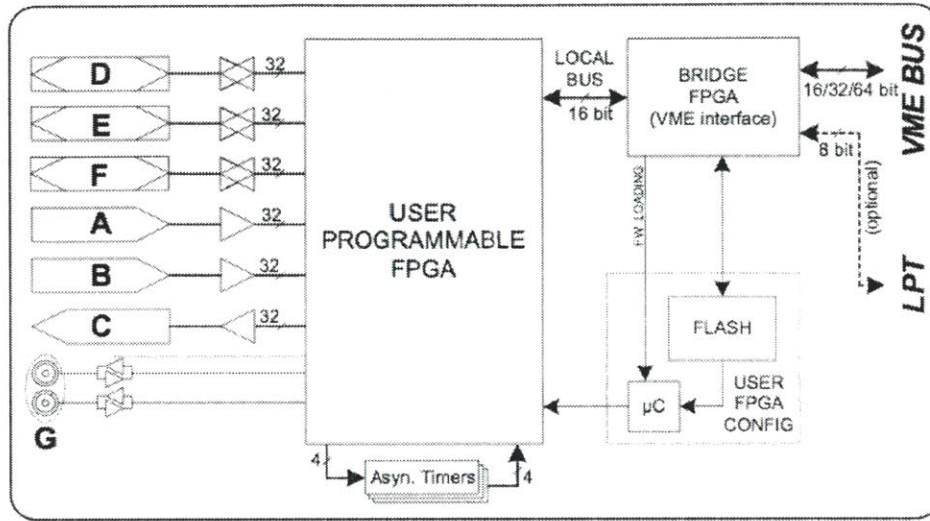


Figure 5-6. Block diagram of v1495. Figure is taken from CAEN.⁵³

5.2.2. Electronics based on ADC

In ADC operation, the analog signal waveform is digitized and then, using an internal FPGA, is digitally integrated and results in a single digitized charge number and then passed along to the computer for analysis. Unlike the QDC, which uses gate signal and threshold discriminators, ADC does not lose any data information. The errors associated with ADC are due to analog-to-digital conversion and the resolution of ADC. One of the main issues with using ADC is the large amounts of data that are generated for even a short experiment.

The ADC data acquisition system was based on a flash analogue-to-digital (FADC) converter and a FPGA. The system is housed in a CAEN crate. The high voltage is supplied by a CAEN N1470 High Voltage Supply. The signal from each PMT runs directly (no amplifiers or LLD unit are necessary) into a CAEN v1720 fast digitizer. The digitizer issues individual raw channel triggers on the front panel through an LVDS

ribbon connector. Charge integration of all enabled channels is triggered by the internal majority logic condition. Internal trigger output on the front panel TRIG OUT sends the trigger pulse to the FPGA through a LEMO connector. Acquisition is inhibited by low logic on S-IN front panel input. The trigger pulse from v1720 is received by a general purpose VME board v1495. The schematic of the hardware setup is pictured in Figure 5-8.

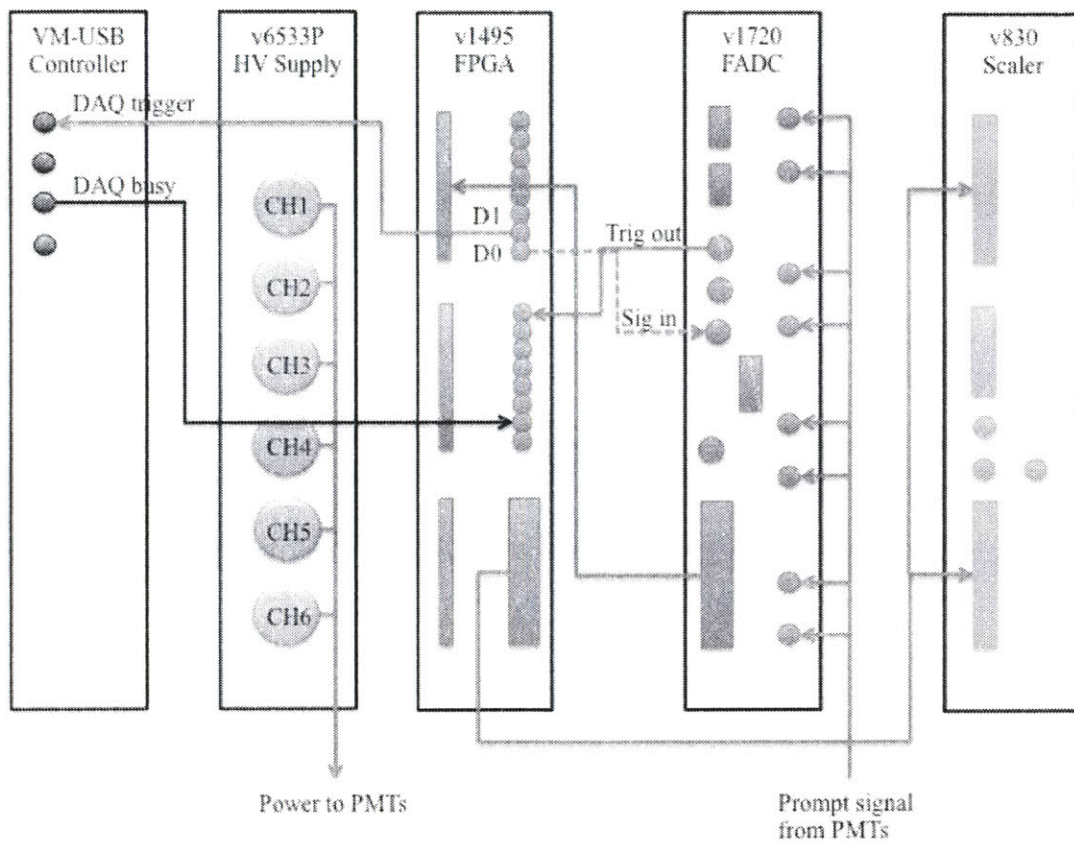


Figure 5-7. Fast ADC data acquisition setup.

Analogue-to-Digital Converter

The ADC used in the WCD data acquisition system is CAEN Mod. V1720, a 1-unit wide VME 6U module housing 8 Channel 12-bit Flash ADC Waveform Digitizer with threshold Auto-Trigger capabilities. The front face of the digitizer and its block diagram are shown in Figure 5-9.

The unit is capable of self-gating integration which implies that there is no necessity for a delay line, as was discussed for the QDC system, that delays the analog so that it appears within the gate interval. In addition, the ADC performs automatic pedestal subtraction.

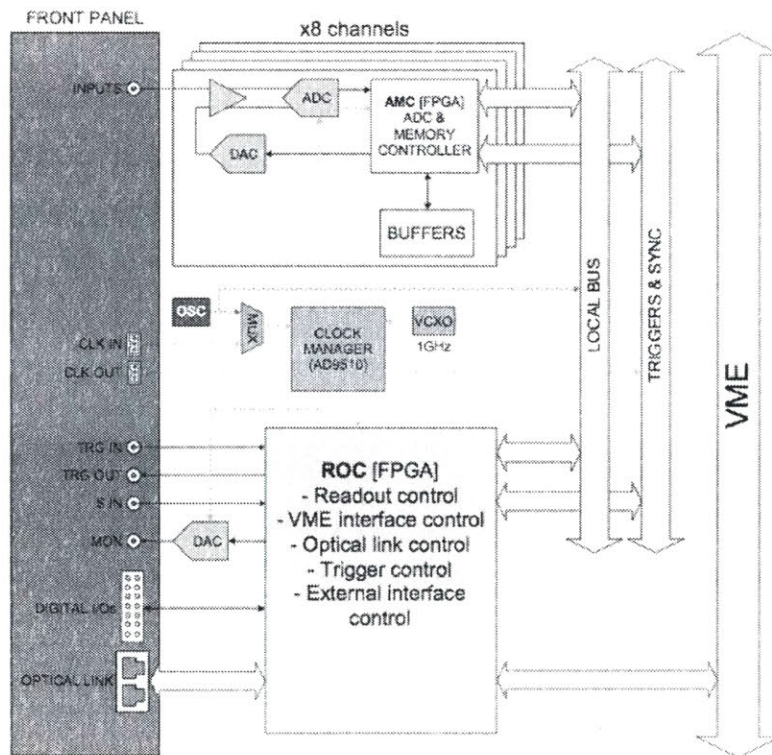


Figure 5-8. Block diagram of v1720 digitizer. Figure is taken from CAEN.⁵⁴

The digitizer uses flash conversion, which feeds the signals from the PMTs in parallel into a bank of threshold capacitors. One of the major advantages of instrumentation ADC is the speed of data conversion. The sampling rate of the v1720 is 250MS/s (megasamples per second), thus sampling the waveform every 4 ns. Each channel can generate its own trigger if the pulse height exceeds a digitally set threshold. In addition, the v1720 allows setting for a coincidence threshold level between channels. Specifically for WCD DAQ, the trigger from the digitizer is issued through TRIG_OUT LEMO output into v1495 mezzanine card A395D.

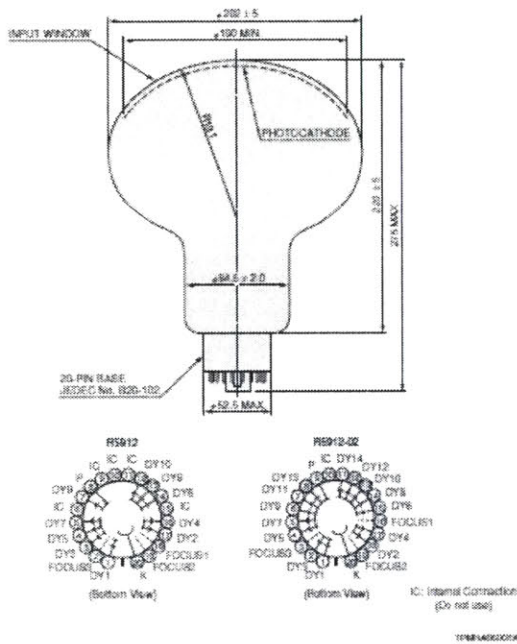
5.3. Photomultiplier properties

The principle of operation of a photomultiplier tube is based on two phenomena: photoelectric effect and secondary electron emission. A PMT converts photons incident on the photocathode into primary photoelectrons which are multiplied when they travel from dynode to dynode. The final electrons are collected at the anode, and the output pulse is produced. Performance of PMTs differs in different light collection scenarios. In multiple electron state, or high light level applications, pulse pile-up might occur masking signals as noise. Generally, such pulses are not handled individually, but rather as analog current. On the other hand, in low light level application or so-called single photoelectron counting, the output pulses can appear discreet. In the single photoelectron counting method, the number of events is proportional to the intensity of the incident light. This counting method is also called digital.

PMTs combine high gain, low noise levels, and high-frequency response. They are an essential tool in UV and visible photon detection applications. In this detector system, Hamamatsu R5912-02 tubes are used. The dimensions of the tube as well as the characteristics of the voltage divider are shown in Figure 5-10. R5912-02 are 14-stage

tubes with spectral response between 300 and 650 nm. The photocathode material is bialkali with borosilicate glass as window material. The gain curve of R5912-02 tubes is also shown in Figure 5-9 and shows that 14-stage tubes outperform 10-stage tubes (R5912 curve) for typical operational voltages of 1400-1800 V. Because the output pulse height depends on the supply voltage (gain), the higher gain of 14-stage tubes generally do not require an amplifier, leading to a simplified electronics setup and reduced noise.

●R5912, R5912-02



GAIN

●R5912, R5912-02

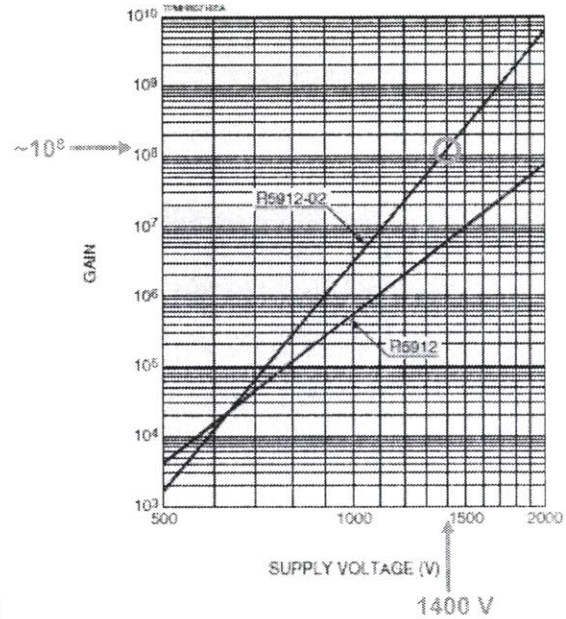


Figure 5-9. Hamamatsu PMT characteristics. From Hamamatsu.⁵⁵

5.3.1. Quantum Efficiency

The quantum efficiency (QE) of the photomultiplier tube is an essential quantity to characterize the performance of the tube. Generally, spectral response of the tube is

expressed in QE or radiant sensitivity of the photocathode. QE is defined as the probability that a photon incident on a cathode will eject a photoelectron. In single photoelectron counting, QE represents the ratio of ejected electrons to the number of incident photons. Radiant sensitivity is the photoelectric current from the photocathode divided by the incident radiant power at a given wavelength of photon as defined by Hamamatsu.⁵⁵

The QE is generally difficult to measure because calibrated light sources are necessary. Hamamatsu provides QE for each tube type. QE and radiant sensitivity of R5912-02 tubes are shown in Figure 5-11.

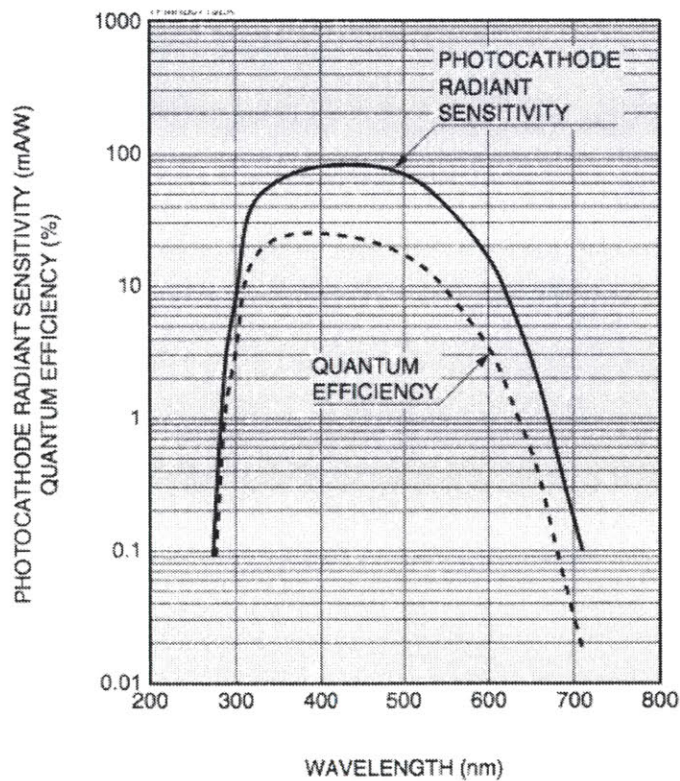


Figure 5-10. QE for Hamamatsu R5912-02 tubes.

5.3.2. Noise

Noise in PMTs is primarily a result of statistical fluctuations in dark current, which is thermal emission of electrons encountered even in the absence of light. Other sources of noise include glass scintillation, field emission, and electrical ringing. Noise affects the signal-to-noise ratio and can affect counting accuracy if the count rate is low.

Thermionic emission of electrons is temperature-dependent, and minimization of the noise can be achieved by cooling the PMT cathodes. PMTs with sensitivity in red and infrared regions are more susceptible to noise even at room temperatures. The PMTs used in WCD applications have bialkali photocathodes, which have relatively low dark current due to thermionic emission.⁵⁵

Glass scintillation occurs when electrons, whether in vacuum or more rarely outside of the tube strike the glass window. If the tube is operated with the anode grounded (negative voltage), primary electrons leaving the photocathode may be attracted to the glass bulb, deviate from their trajectory to the first dynode, and cause glass scintillation. In WCD application, the tubes are operated with positive voltage (cathode is grounded) because the photocathodes are submerged in water. Glass scintillation is less of an issue for WCD practice than in applications that use negative high voltage.

5.3.3. Single Photon Testing

Hamamatsu R5912-02 tubes are designed for single photoelectron pulse height distribution measurements. Pulse height distribution can be used to measure PMT efficiency and stability over time. For testing purposes, single photoelectron counting was performed on all Hamamatsu PMTs.

A light-tight box was built specifically to investigate single photoelectron event with the PMTs. The box was equipped with an optical bench, a PMT holder, and an LED holder as shown in Figure 5-12. A small 1" in diameter Hamamatsu tube is shown in the bench for illustrative purposes only.

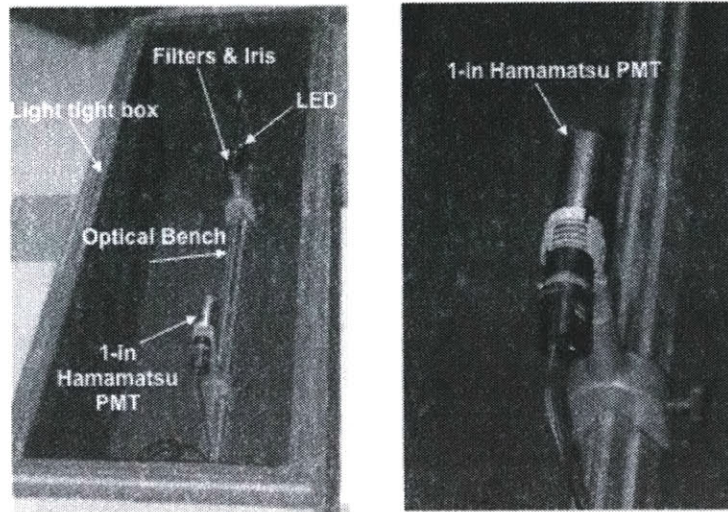


Figure 5-11. Black box testing

Schematic diagram of the experiment is shown in Figure 5-13. The pulse generator (Berkeley Nucleonics BNC 575-4c) was set to send out a signal to the LED and to send a gate to an ORTEC multichannel analyser (MCA). The LED emitted 365 nm photons incident onto a PMT. The photons were filtered through a set of optical filters in order to decrease the number of photons per pulse to an average of less than one. The amplitude of the generated pulses was selected such that only about 10% of the pulses would produce a signal in the PMT. The pulses from the PMT were then sent to a preamplifier to stretch the signal and to an amplifier to shape it. A digital 300 MHz oscilloscope was used to monitor the timing of the signals and Maestro (Ortec) software to plot pulse height spectrum.

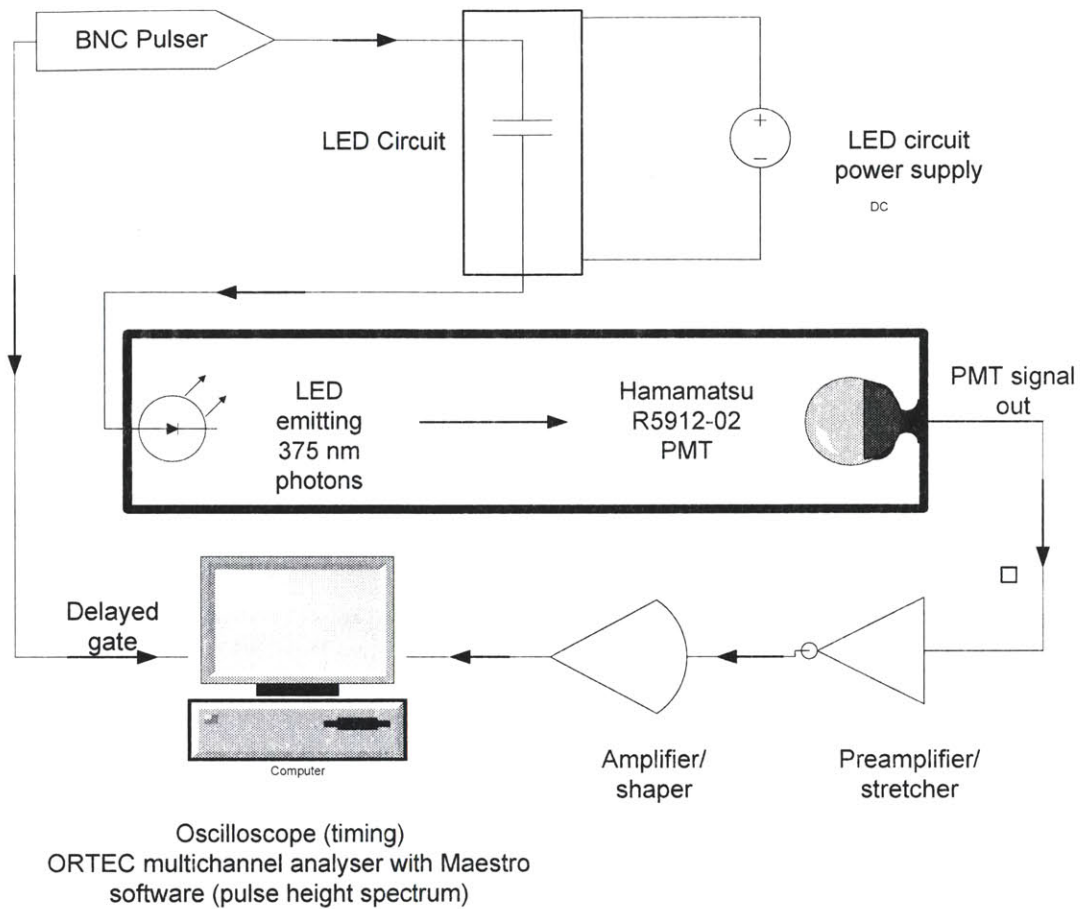


Figure 5-12. Schematic diagram of PMT testing with LED

Figure 5-14 shows an example of the LED input and pulse output. Note that two examples are plotted: “no event” and “a single event.” The first example shows that even when a photon is incident onto a photocathode, there might not be an event due to quantum efficiency of the photocathode. Second example shows the shape and timing of the single photoelectron signal.

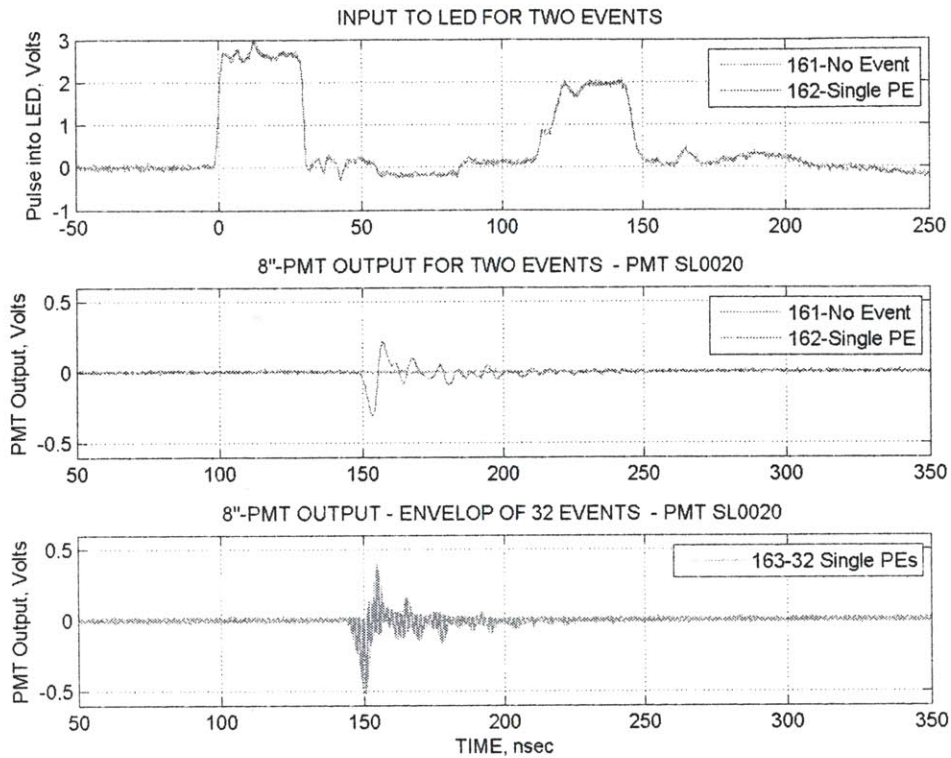


Figure 5-13. Observed single PE data with 8-in Hamamatsu PMT.

Test parameters and the results of an average test are summarized in Table 5-1. The high voltage was set to 1400 V in order to obtain a gain of 10^8 (as shown in Figure 5-10). Obtained pulse height was 200 mV on average with pulse width of 5 nsec. Corresponding charge was calculated to be 2×10^{-11} C assuming $50 \Omega^{\circ}$ impedance of the oscilloscope. This charge is an output of the last dynode of the PMT. Recall that the voltage was set such that 10^8 amplification of the signal was obtained. Thus, the corresponding photocathode charge was 2×10^{-19} . This is another indicator that the signal was produced by a single photoelectron since the charge of an electron is 1.6×10^{-19} C.

[°] The specifications were provided by the manufacturer.

Table 5-1. Test parameters and output values of single photoelectron testing.

| Test parameters | | Notes |
|--|--------------------|---|
| High voltage supplied, V | 1400 | PMT gain is 10^8 at the voltage shown in Figure 5-8 |
| Pulse width, ns | 11.25 | As supplied into the LED |
| Impedance, Ω | 50 | |
| Frequency, Hz | 10 | |
| Power supplied into LED pulse box, V | 8 | |
| Output | | |
| Pulse height, mV | 200 | As obtained from the PMT using oscilloscope (512 average setting) |
| Pulse width, nsec | 5 | |
| Total peak area, mV-nsec | 1000 | |
| Corresponding charge from last dynode C_{14} , C | $2 \cdot 10^{-11}$ | Charge from the last (D14) dynode into 50Ω |
| Corresponding charge at the cathode C_D , C | $2 \cdot 10^{-19}$ | C_D is a ratio between C_{14} and the corresponding gain (10^8) |

Single photoelectron peaks were obtained with ORTEC MCA. Figure 5-14 shows a single photoelectron peak as well as the pedestal.

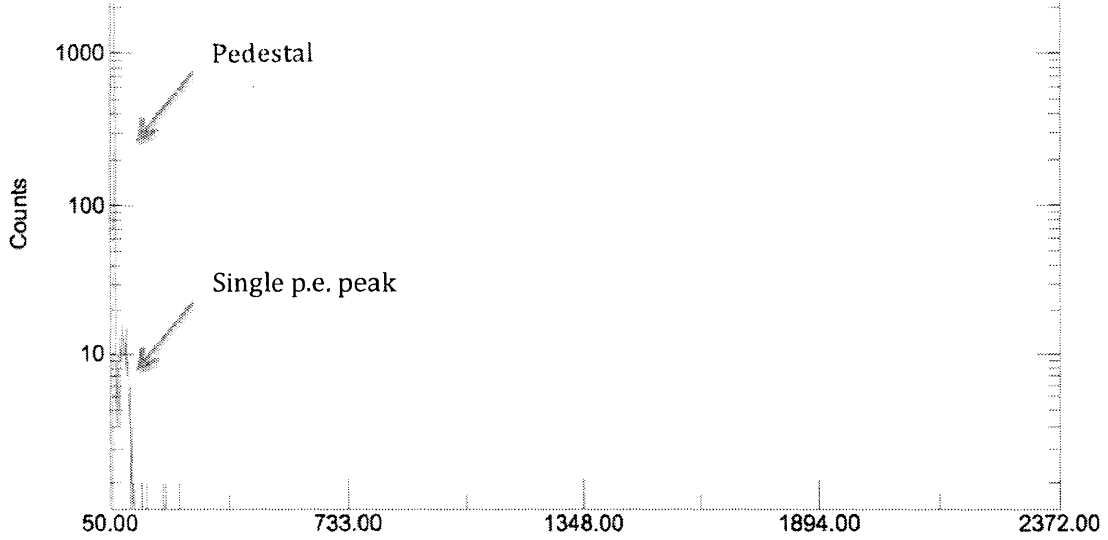


Figure 5-14. Single photoelectron peak observation. The abscissa is in arbitrary bin units.

Performance of each PMT was verified using black box testing, and the results were found to be in agreement with the specifications provided by Hamamatsu. Table 5-2 lists the operational voltages for the PMTs.

Table 5-2. Operational characteristics of PMTs.

| PMT | PMT serial number | Operational voltage, V |
|-----|-------------------|------------------------|
| 1 | SL0013 | 1352 |
| 2 | SL0019 | 1248 |
| 3 | SL0020 | 1216 |
| 4 | SL0015 | 1336 |
| 5 | SL0014 | 1376 |
| 6 | SL0017 | 1344 |

5.4. Detector response to LED pulsed at various frequencies

In an attempt to characterize the PMT response to the submerged LED, the LED was pulsed at several frequencies. The aim of this study was to determine if the LED is capable of producing a discrete signal that can aid in the calibration process. The LED was pulsed at 9.20 volts over four different frequencies (10Hz, 100Hz, 1kHz, 10kHz) and the PMT output was recorded and plotted in Figure 5-15. The DAQ system was based on QDC.

Note on Figure 5-15 that the detector response changes dramatically as the frequency of the LED increases. The abscissa of the graph corresponds to the QDC bin number, and the ordinate shows the number of counts collected over 10 minute periods. The background (BG) shows typical features of the spectrum collected with a Cherenkov detector: low-energy noise and high-energy cosmic ray peak. The muon peak is nearly constant for BG, 10 Hz and 100 Hz cases. In fact, BG and 10 Hz cases show nearly complete overlap except for an additional peak corresponding to the pulse signals. 100 Hz case starts to show some deviation from the BG which is seen as a shoulder rise in bins 1000-3000. This deviation is most likely because of the significant increase of the dead time of the detector. The dead time was calculated as the ratio of the number of live triggers to raw triggers in the DAQ. Table 5-3 shows the dead time as a function of LED frequency. When frequency reaches 1 kHz (1000 pulses per second), the dead time of the detector is 95%. Increasing the frequency beyond that causes the detection system to produce undesired results, shown in Figure 5-15, which cannot be used to monitor detector's performance.

LED Pulse Study

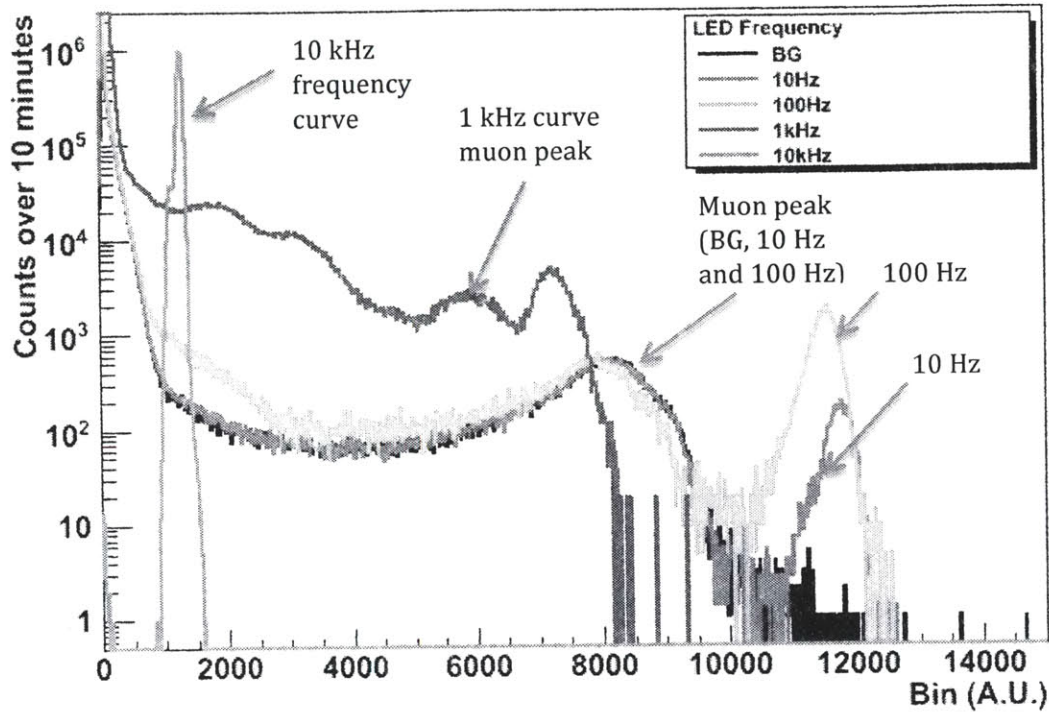


Figure 5-15. PMT response to LED pulsed at four frequencies, each increasing by a level of magnitude.

Based on this study, it was concluded that a LED frequency of 10 Hz produces a clearly identifiable peak as shown in Figure 5-16. This value is used in subsequent detector stability monitoring.

Table 5-3. Dead time of the detection system as a function of LED frequency.

| LED Frequency | % Dead Time of System |
|-------------------|-----------------------|
| 0 Hz (Background) | 17% |
| 10 Hz | 38% |
| 100 Hz | 82% |
| 1 kHz | 95% |

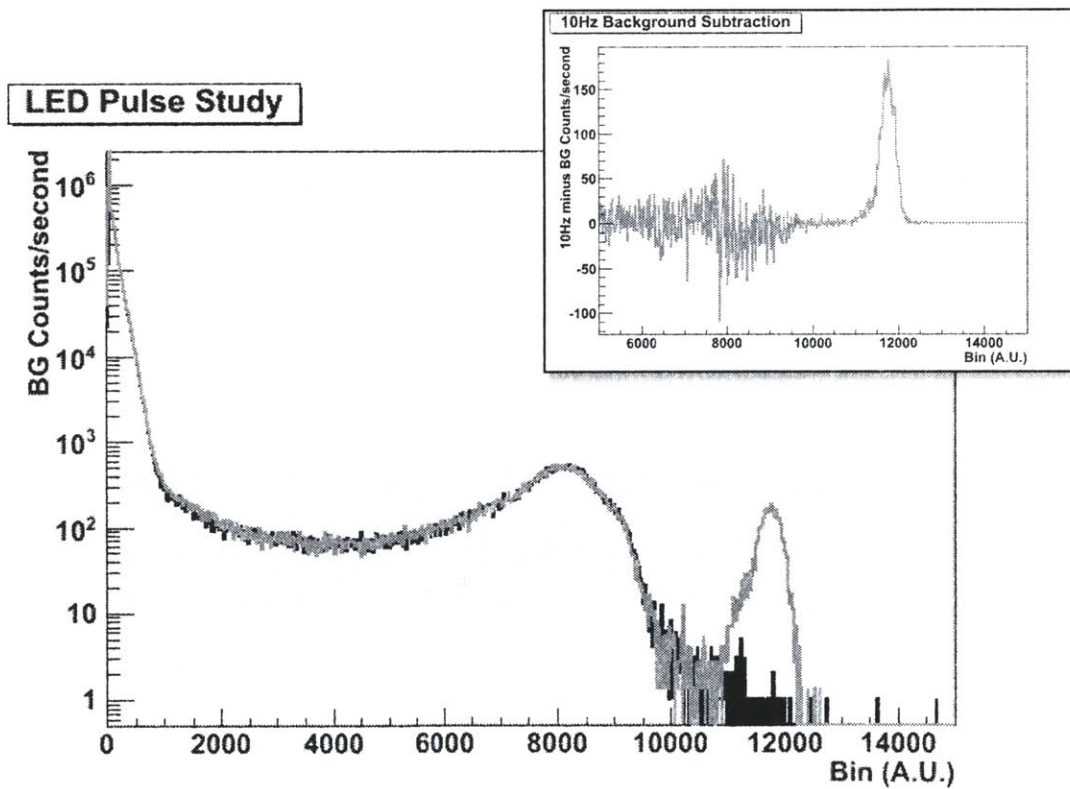


Figure 5-16. Comparison of background and 10 Hz spectra. The insert shows background-subtracted spectrum of 10 Hz LED pulsing.

5.5. Water filtration and recirculation system

Water quality affects Cherenkov photon collection efficiency to a large degree as was shown through simulation in Chapter 4. Photon absorption in water is a significant source of uncertainty both in simulation and experiment. Water purification can be done on multiple levels depending on a desired outcome: simple filtration to remove particulates, de-ionization to remove ions, UV light to kill bacteria, or a combination of any of the above. Ideally, all three methods would be used in order to obtain water of the best possible quality.

5.3.1 Experimental investigation of water purity effects on signal

Preliminary investigations of the effects of water clarity on signal were performed prior to filling the detector. An attenuation arm was constructed with a UV (365 nm) LED pulser on one end and a photomultiplier tube on the other. The 8' long arm was constructed out of 4" in diameter PVC pipe. The LED was excited by 35-ns pulses with a 100 Hz repetition rate. The output of the PMT was monitored using 300 MHz oscilloscope.

Three "types" of water were considered for comparison: tap water, tap water filtered with a combination of two filters (0.5 and 0.2 μm), and DI water. For each case, several samples were acquired in order to assess the variability between samples of the same water type. All data were averaged over 512 consecutive pulses using a built-in oscilloscope function. The input to the LED was recorded for each event to monitor changes, if any, in the driving pulse. No changes have been observed for all samples.

Figure 5-17 shows the PMT pulse outputs for various water samples. The metric for transmissibility was taken to be the peak height of each PMT pulse. Figure 5-17

shows that these peak heights vary with water type, but also vary between same type water samples. The variability between samples of the same type was attributed to the presence of bubbles in the tube, whose quantity cannot be effectively controlled without an on-demand re-circulation system.

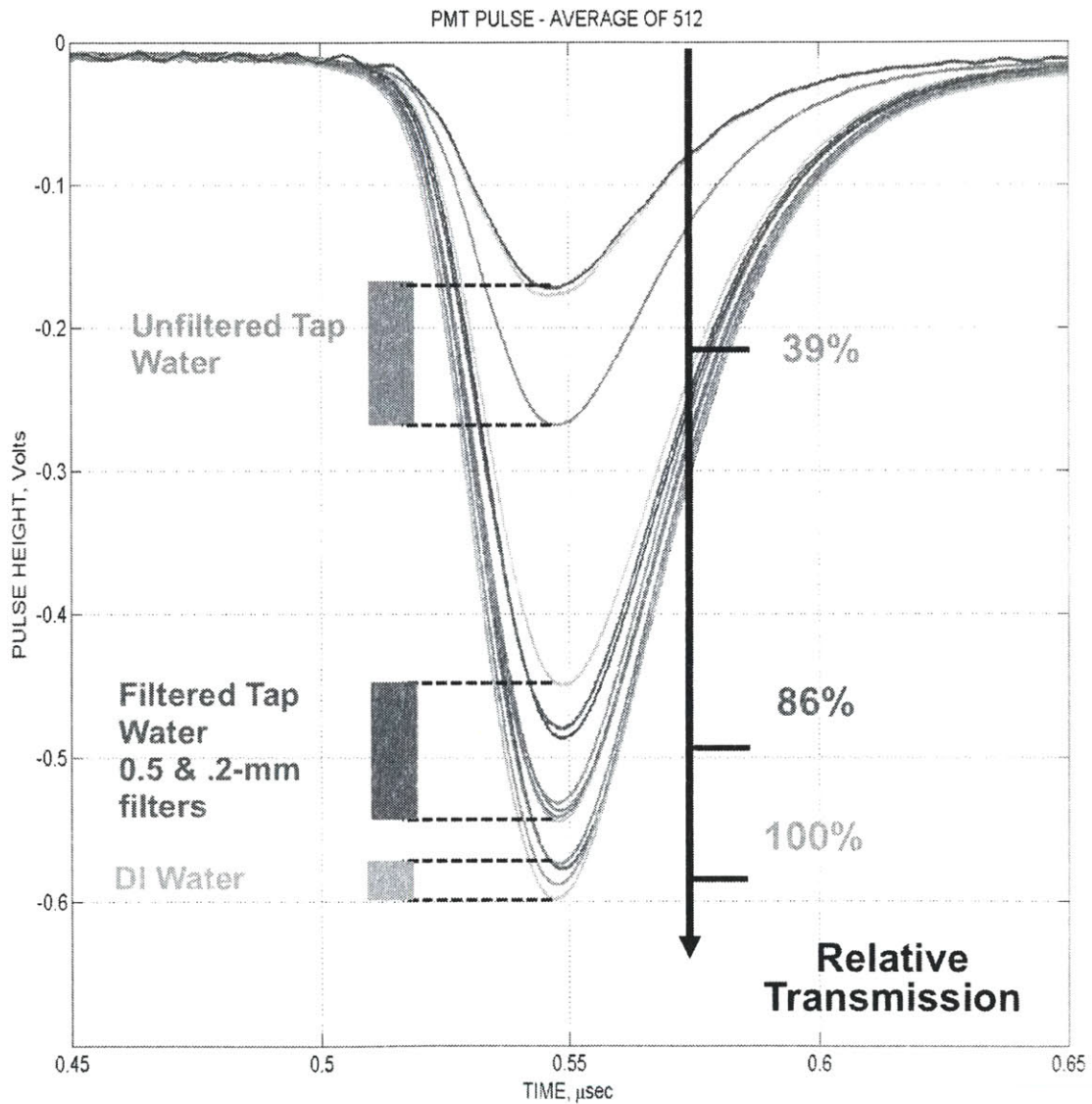


Figure 5-17. Comparison of pulse height changes for various water samples.

Relative comparison of the PMT signal outputs lead to the following observations:

1. The transmissibility is highest for the DI water, followed by the filtered tap water, and then the unfiltered tap water.
2. The DI water exhibits the minimum variability between samples, and the unfiltered tap water shows the greatest variability between samples.
3. Defining the DI transmissibility as 100%, the transmissibilities of the filtered water and the unfiltered water are 86% and 39%, respectively.

The data shown in Figure 5-17 provide information on the relative water transmissibility. They clearly indicate that the DI water is superior to all other two types. However, they do not necessarily imply that the filtered water is unsuitable for the operation of Cherenkov detector. To avoid complications that may arise with using the unfiltered water, a DI water filtration system was implemented in the water recirculation loop of the prototype tank. The water recirculation system is capable of removal of bubbles and maintenance of water quality over long test periods.

5.6. Detector response to variations in water purity

During the initial testing of the detector, electrolysis stains on the internal walls were noted. The detector was disassembled in order to further investigate the cause of the stains and their effect of the water quality. Once the tank was drained and the polypropylene liner supporting the Gore reflector was removed, a significant accumulation of rust was found on the LED plate. The rust was caused by the presence of a small (3 mm in diameter) piece of carbon steel from a drill. The drill was used to create

holes for the support of the plate. Figure 5-18 shows the location of the LED plate in the tank as well as the corrosion stains.

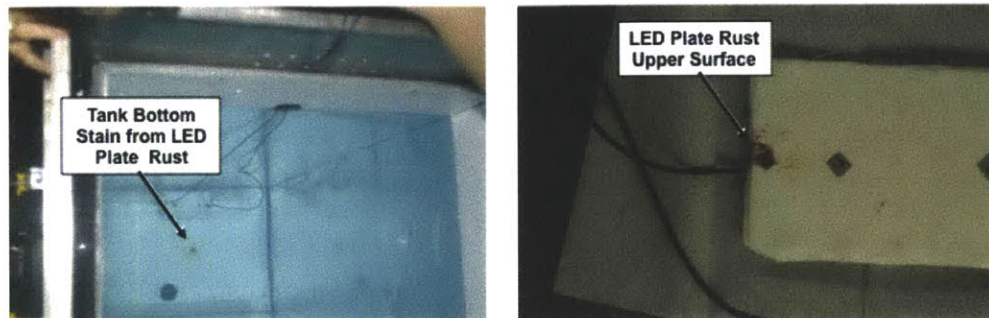


Figure 5-18. LED plate corrosion.

All of the components of the detector were thoroughly cleaned, and the plate and the reflector attached to the plate were replaced. The tank was refilled with DI water, and spectral measurements were retaken. Figure 5-19 shows the change in spectra before and after the tank cleaning. Note that muon peak moved after the water in the tank was replaced indicating that larger signals were being collected. It must be noted here that an important assumption about the detector was made: the performance of the PMTs did not change, and all other parameters except for water transmissibility were the same. The following observations and conclusions were derived from this experiment:

1. Water purity has an effect on detector stability of operation. The water quality must be maintained at a constant level in order to avoid variations in the spectral response of the detector. It was shown with simulations that the quality of the water has a definite effect on the performance of the detector. Assuming that the assumption about the PMTs was true, this experiment supports this observation.

2. Introduction of dissimilar metals in the detector must be avoided, as the DI water tends to increase corrosion rates.
3. Gore reflector can be easily cleaned without damaging its properties.

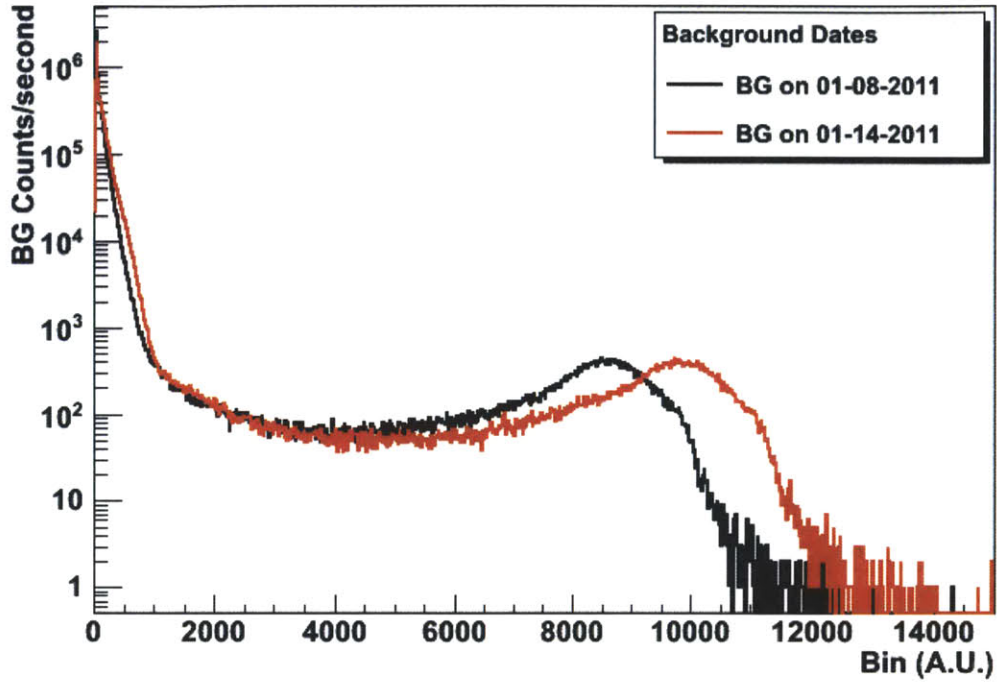


Figure 5-19. Background spectra before and after the tank cleaning.

6. Calibration and efficiency of the detector

Energy calibration of the detector is a crucial part of the detector development. The calibration cannot be achieved by Monte Carlo simulation alone due to the uncertainties associated with the water optical transmission coefficient, reflectivity of the walls, and PMT quantum efficiency. Thus, the overall energy calibration must be performed *in situ* while using simulation as a supplemental verification tool.

Calibration of a water Cherenkov calorimeter as applied to remote detection is not necessarily about the energy resolution, but rather about where to place an energy cut. The goal of the detection is to determine whether high-energy (3-10 MeV) gamma rays appear as a result of interrogation. The characteristic radiation from fission or photofission is mostly continuous in the range from 3 to 6 MeV.¹⁷ In addition, the effect of Cherenkov radiation modulates the linearity of the energy scale since the size of the signal is not directly proportional to the energy of the interacting particle, especially in the lower energy region. However, the size of the signal is proportional to the detection medium. This includes effects of the water clarity and reflector properties, which may impair the resolution of the detector. Another source of resolution loss in Cherenkov detector is drift in the operating parameters associated with the PMTs. We expect the contribution of electronic noise to be negligible, especially since preamplifiers and amplifiers are not used, and the PMTs can resolve single photoelectrons.

In this particular detector setup, the reflectivity is assumed to be constant. However, the quality of water is considered to be variable. This is because the detector is designed to be transportable and to be deployed at various locations, and even though the

detection system is equipped with a water purification system, the transmissibility of water cannot be assumed constant.

The detector was calibrated using multiple radiation sources in order to determine lower level of sensitivity as well as to study the detector response to gamma rays with various energies. The signals are collected as digitized data. Converting MCA scale to energy scale is possible, but the peak does not correspond to the energy of the particle, but rather to the average number of Cherenkov photons produced by the particle.

Calibration of the detector using cosmic muons is less straightforward because the cosmic rays arrive at a distribution of angles and momenta. In addition, the calibration of Cherenkov detectors at a higher energy range may not be representative for the low-energy, 3-10 MeV, range. However, the muons and the peak they produce in the spectrum are very useful for monitoring the stability of the detector.

6.1. Computational evaluation of detector resolution

Energy resolution of Cherenkov detectors is dominated by photoelectron statistics. Unlike solid-state detectors and conventional scintillators, the resolution of Cherenkov detectors is quite low which results in broad peaks that are sometimes undistinguishable especially for low-energy events.

There are several reasons for this low energy resolution. The most important is the small number of Cherenkov photons created during particle interactions in the detector. Table 6-1 summarizes results of simulation for monoenergetic gamma ray interactions in the Cherenkov detector. The simulation was done for six cases of gamma rays with energy varying between 1 and 10 MeV. Each case included 10,000 histories. Recall that

the Cherenkov threshold for a gamma ray is 0.42 MeV. The average number of photons produced in our Cherenkov counter per 1 MeV gamma is ~65. This number corresponds to optical photons of energy between 1 and 4.5 eV. This energy span is equivalent to selecting photons with wavelengths between 270 and 1200 nm in order to reduce computational time. Note that the Cherenkov spectrum continues in UV (wavelengths less than 270 nm), but the PMTs are essentially insensitive to light with wavelengths in that region. These 65 photons result in 2.4 photoelectrons produced in all PMTs (summed response). As the energy of the gamma ray increases, the ratio of photoelectrons to Cherenkov photons stays relatively constant indicating signal linearity with deposited energy. Note that as the energy of the gamma rays approaches the Cherenkov threshold, this linearity becomes no longer valid. This observation was useful when detector calibration was performed.

Table 6-1. Average photoelectron production as a function of gamma ray energy.

| Energy of incident gamma, MeV | Average number of produced photoelectrons, per gamma, summed response in all PMTs | Average number of Cherenkov photons, per gamma, summed response in all PMTs | Ratio |
|-------------------------------|---|---|-------|
| 1 | 2.4 | 64.4 | 0.037 |
| 2 | 13.1 | 365.7 | 0.036 |
| 3 | 26.4 | 725 | 0.036 |
| 5 | 51.0 | 1404 | 0.036 |
| 7 | 67.2 | 1860 | 0.036 |
| 10 | 100.1 | 2760 | 0.036 |

Graphical results of Table 6-1 are presented in Figure 6-1. The monoenergetic peaks were fitted with a Gaussian distribution. The peak corresponding to a monoenergetic gamma ray moves as the energy increases. In addition, there is a significant broadening of the peak. Figure 6-2 shows the dependence of pulse height and energy resolution on gamma ray energy. The parameters were calculated by fitting the peaks shown in Figure 6-1 with a Gaussian function. Note that the error bars corresponding to the peak locations are $\pm\sigma$, where σ is the standard deviation. The resolution was calculated using Equation 6-1, where FWHM is the full width of the peak at half maximum, and H_0 is the location of the peak centroid.

$$R = \frac{FWHM}{H_0} \quad \text{Eq. 6-1}$$

The energy resolution of Cherenkov detector approaches 37% as the energy of the incident gamma ray increases. Such poor energy resolution makes distinguishing between gamma rays of similar energies, for example 3 and 5 MeV, very difficult, if not impossible. Figure 6-3 illustrates the case when gamma rays with energies of 2, 3, and 5 MeV are incident and perpendicular to the detector face. All cases of simulation assumed the same number of histories (10,000 incident particles).

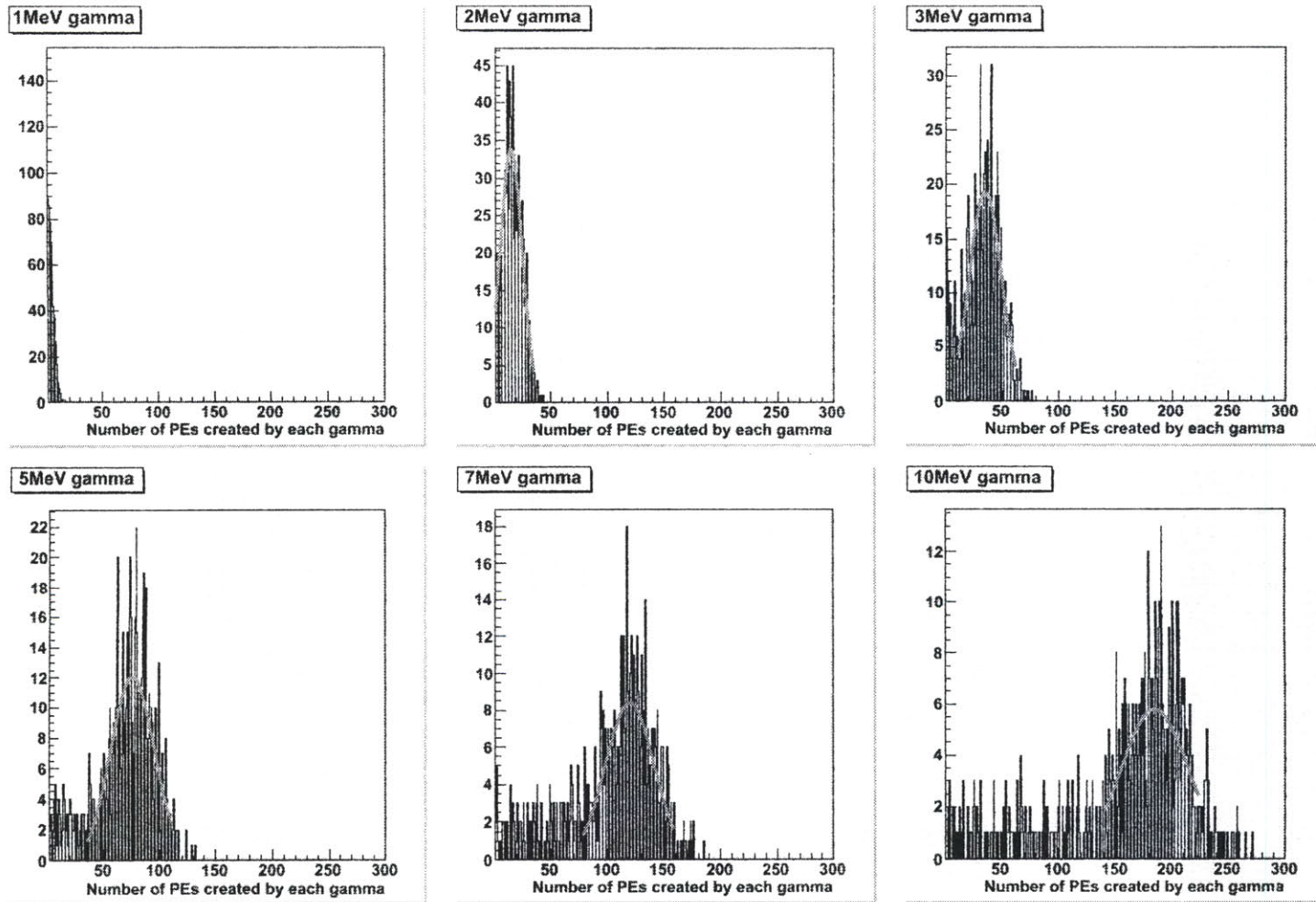


Figure 6-1. Pulse height spectra of gamma rays of various energies.

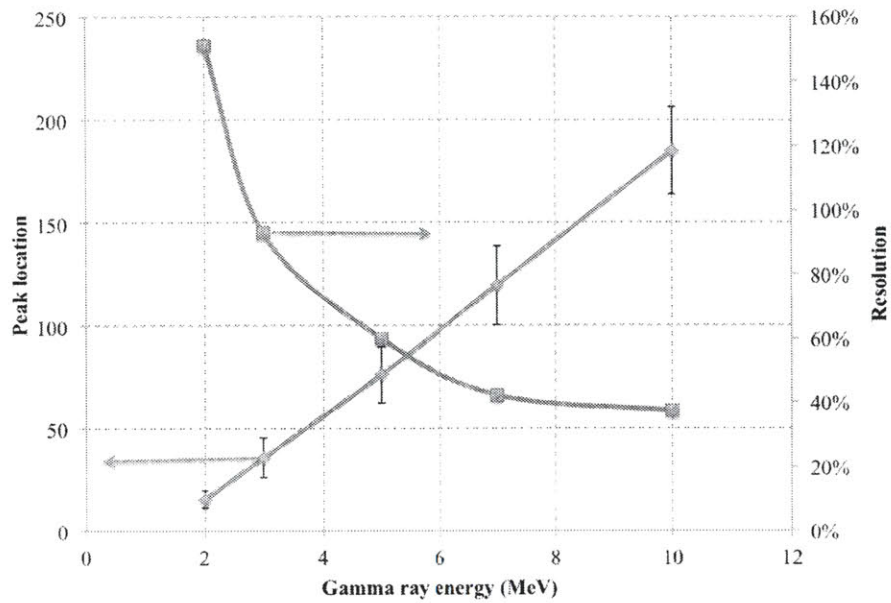


Figure 6-2. Pulse height (peak location) and resolution of the detector as a function of gamma ray energy (MeV). The error bars correspond to $\pm\sigma$.

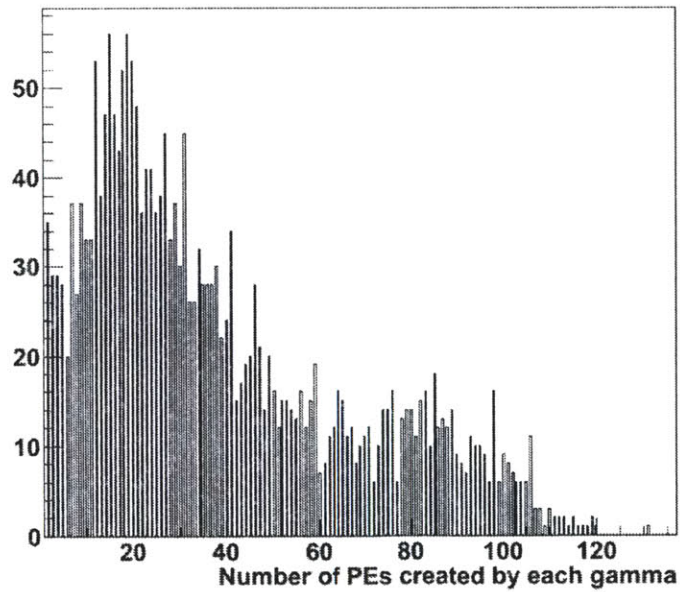


Figure 6-3. Detector response to gamma rays with energies of 2, 3, and 5 MeV.

The pulse height spectra showed in Figure 6-1 are the product of effects due to both electron recoil energy spectrum and detector resolution (Cherenkov light scatter and absorption in the detector medium.) In order to describe detector behavior for sources of various energies, one must take into account both of the contributors, deconvolution of which experimentally is a difficult task. The relationship between the resolution of the detector and Cherenkov light output was determined using computational model results, presented in Figure 6-2. The energy spectrum of the detector was represented as a Gaussian function, and the peak location was calculated; the dependence of peak location on gamma energy is nearly linear. The resolution follows $1/E$ dependence, where E is the energy of the incident gamma rays. These two functions can be folded into a model that describes the resolution change with energy of the gamma rays, as shown in Figure 6-4.

The model function for the resolution curve was fitted using least squares. The equation for the function is provided on the plot. As light output increases, the resolution of the detector becomes smaller, as expected. The behavior at larger energies is similar to one of scintillators. Note that the model includes the contribution from recoil electron spectrum and detector resolution, but the contribution due to electronics was not accounted for. As the energy of the incident particle approaches Cherenkov threshold, and the light output becomes small, the slope of the curve changes.

Increasing the resolution of the detector can help improve signal-to-noise ratio. The noise is generated by PMTs and in electronics. As was mentioned above, the electronic noise does not significantly affect the resolution of the detector, and most of the resolution loss comes from the photoelectron statistics. One of the critical issues is how sensitive the detection is to the thresholds. The threshold is set high enough that most of the noise is ignored by the DAQ.

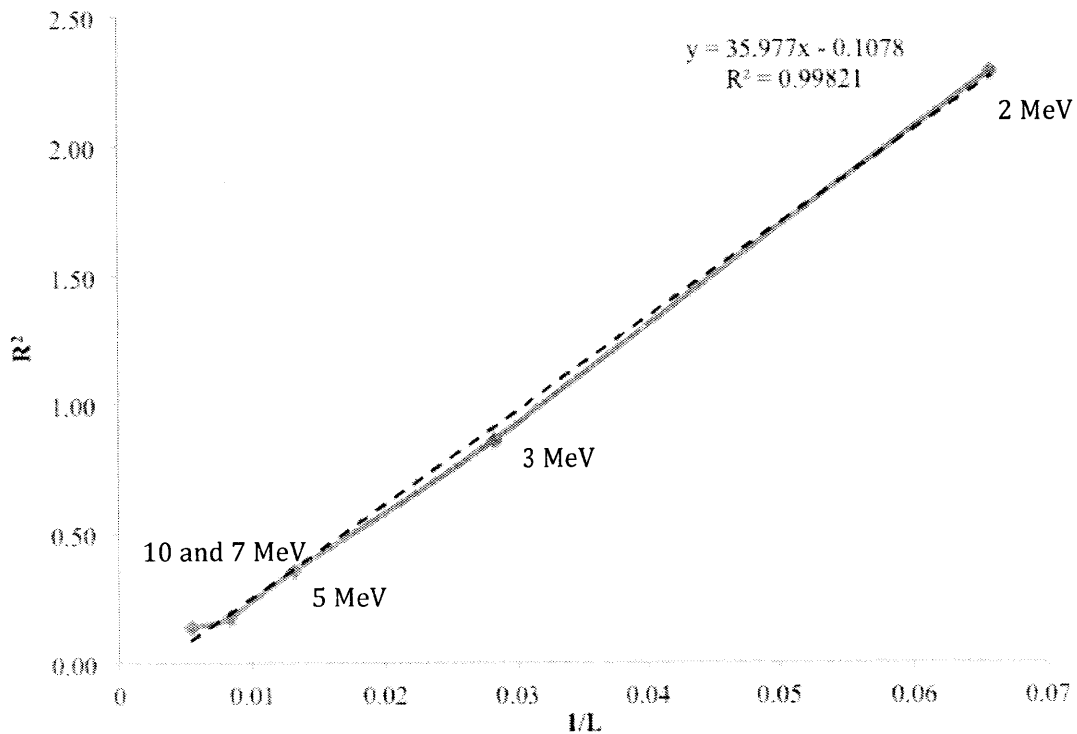


Figure 6-4. Square of resolution vs. inverse of light output (solid line). Results of least square fit (dashed line) are also shown on the plot.

6.2.Sources of error and photoelectron statistics

As with any detection system, the physical quantities measured with the Cherenkov detector require uncertainty assessment. In the current analysis, we differentiate between systematic and statistical uncertainties. Systematic errors arise from mis-calibration of the detector or due to some other effects that are not taken into account during the experiment, but could be corrected for. The systematic errors, once corrected for up to a reasonable degree by adjusting experimental setup, for example PMT calibration, are irreducible. Systematic errors along with random fluctuations dictate the

accuracy of the experiment. Statistical errors are also called random errors or noise. The fluctuations in observation, for example, energy loss by a particle, will affect the precision of the experiment. In Cherenkov detector, the noise arises from uncertainty associated with photon production. Theoretically, the rate of energy loss by a charged particle through Cherenkov light emission can be predicted. In reality, such prediction is not necessarily the actual energy loss by a particle going through the detector. The actual energy loss follows a distribution the mean value of which can be derived (our theoretical prediction), but individual experimental measurement would yield fluctuations around that value. This is well illustrated in Cherenkov pulse height spectra shown in Figure 6-1: each incident gamma ray has the same energy, but the light yield has a distribution. Some correction for random errors is possible by making repeated measurements as well as through refining the experiment. However, once the random errors cannot be reduced beyond the systematic, it is impractical to conduct more measurements.

One of the main objectives of error analysis is to determine the accuracy and precision of the measurement. The measurement takes a finite amount of time, which inevitably introduces an uncertainty in the results. Another reason for uncertainty analysis is to determine whether the equipment, both the detector and the data acquisition system, are working correctly and according to expectations.

6.2.1. Systematic uncertainties

One of the main sources of systematic uncertainty in this experimental setup is from the calibration of the PMTs. The sources of uncertainties specific to PMTs are discussed in Chapter 5. The signal from each PMT is integrated separately and then summed to obtain the pulse height spectrum specific to a source. In order to obtain a good spectrum, each PMT was normalized. However, the calibration of PMTs can affect the peak broadening and the location of the centroid. It is important to realize the effects

of uncertainty introduced by the calibration because the resolution of the detector is already expected to be quite poor as was discussed in Section 6.1.

Figure 6-5 shows the pedestal and the background as obtained by each PMT. The PMTs were originally calibrated using an ORTEC MCA. The CAEN data acquisition system was used to obtain the results shown in Figure 6-4 and the rest of the figures discussed in Chapter 6. Figure 6-6 illustrates pedestal-subtracted background data. The PMTs appear to produce nearly identical spectra including the muon peak location.

Figure 6-7 shows the zoomed-in spectra of Figure 6-6. The PMT individual spectra are plotted along with the average of the six spectra. The bin location of the peak and the average are shown in Figure 6-8. Note that there are two outliers: PMT0 and PMT3 which deviate from the average; the rest of the points are within one standard deviation of the average.

Even though the PMTs were calibrated prior to their installation in the tank, change in data acquisition electronics from ORTEC to CAEN as well as PMT locations in the tank affect relative calibration of the PMTs. Note that the positions of PMTs in the tank can affect the light collection. Identification of the outliers after the PMTs have been installed in the tank can help in calibration of PMTs in the low energy region. Precise calibration of the PMTs will potentially result in decreased systematic uncertainties and in increased resolution.

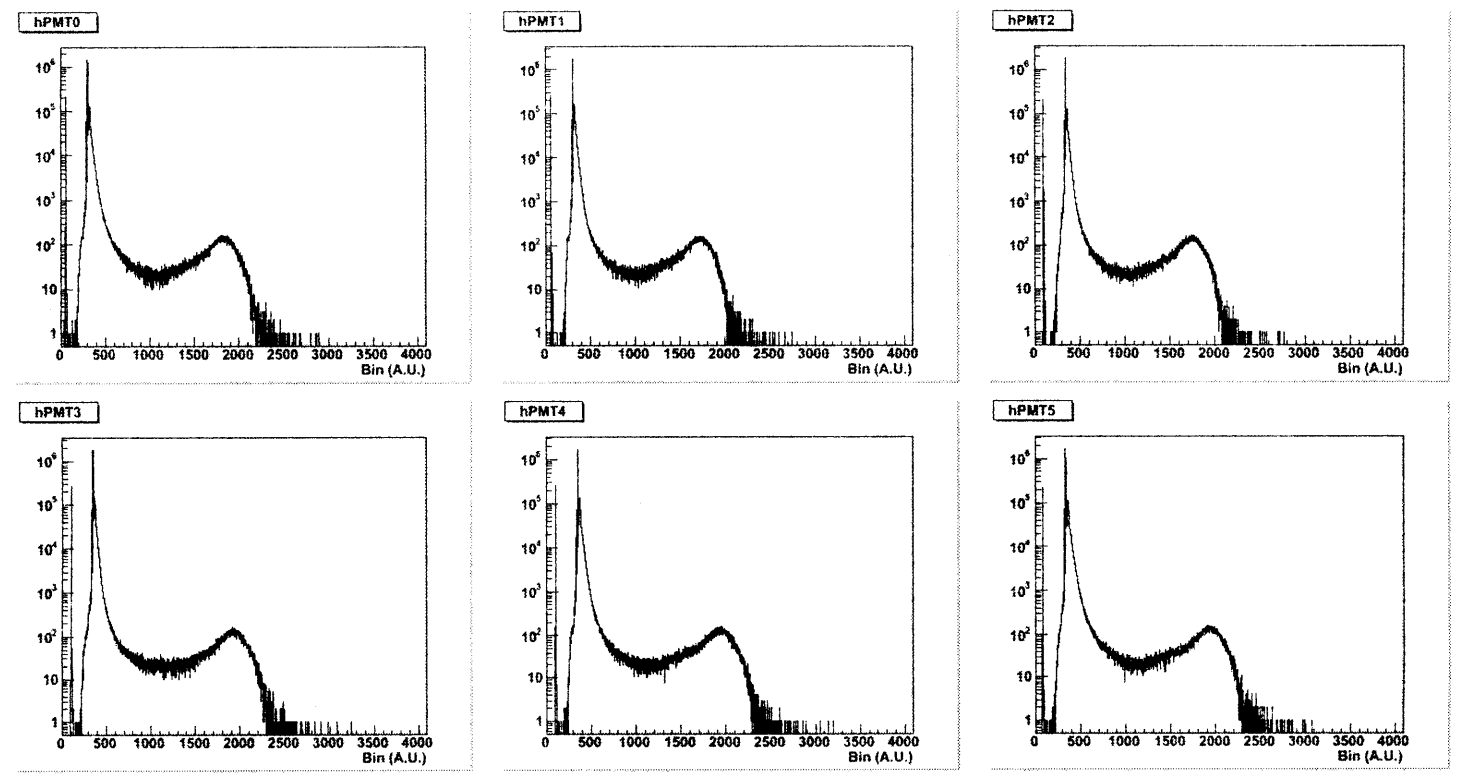


Figure 6-5. Pedestal and background spectra for all 6 PMTs.

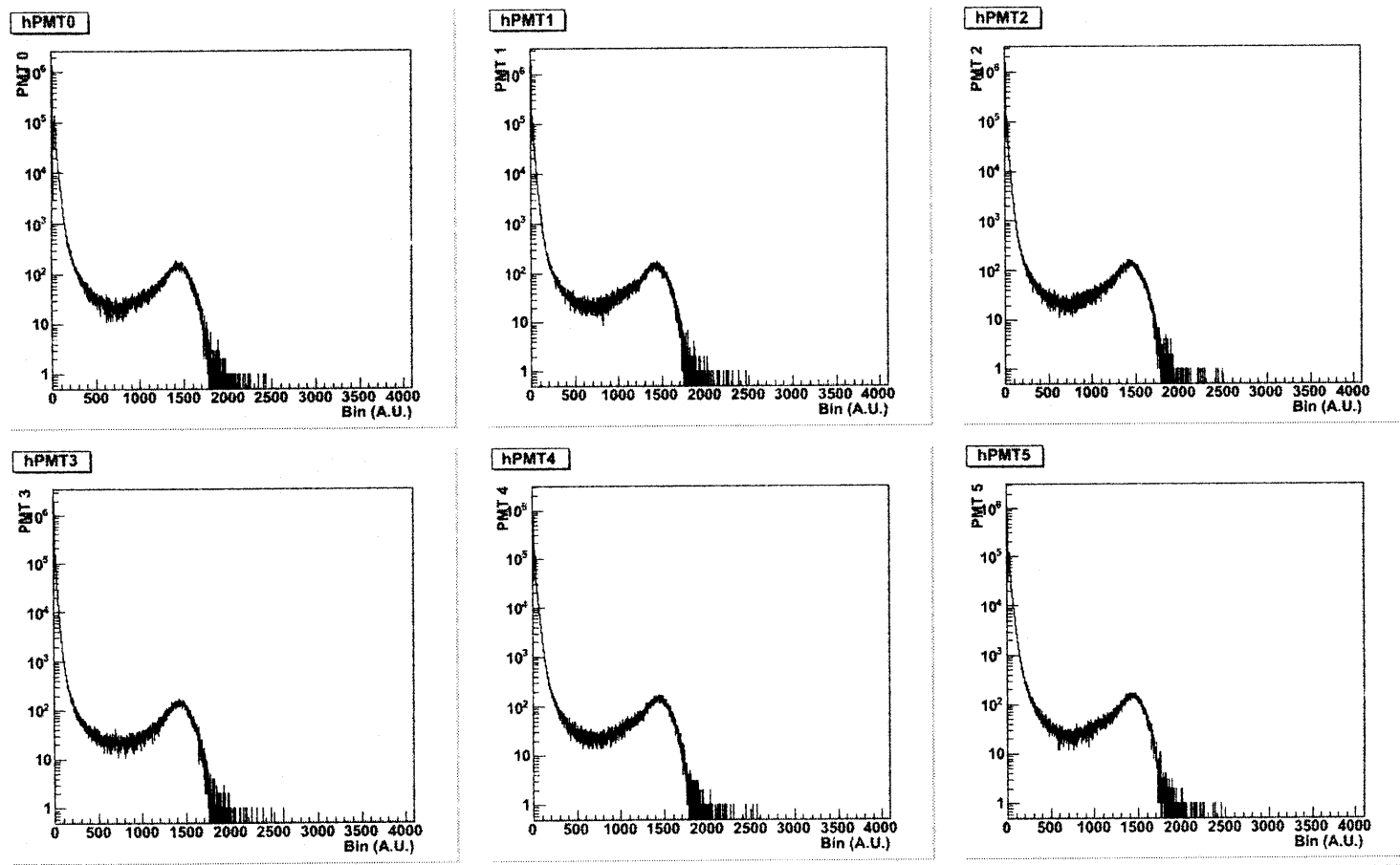


Figure 6-6. BG spectra after pedestal subtraction and normalization.

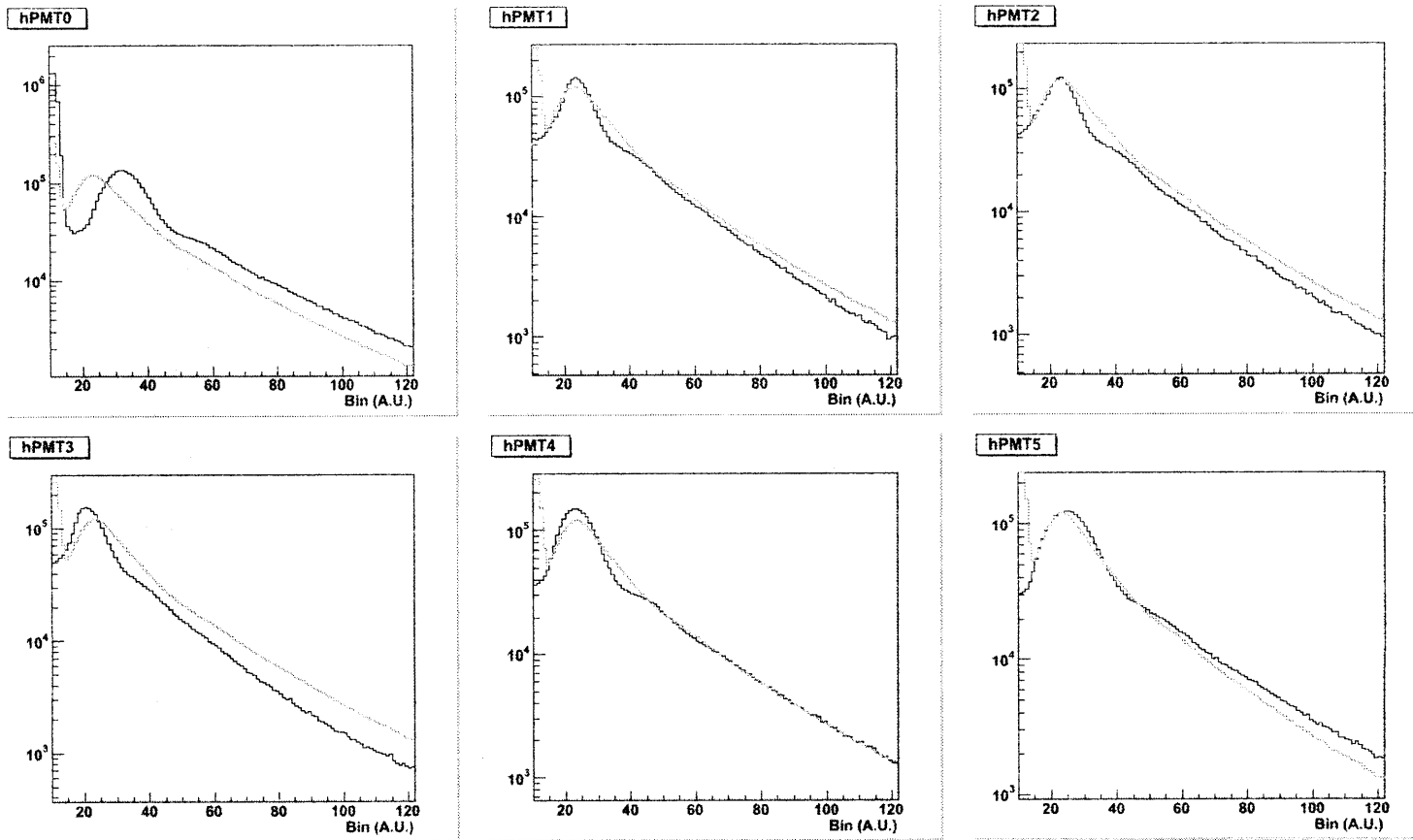


Figure 6-7. Spectra vs. average spectrum.

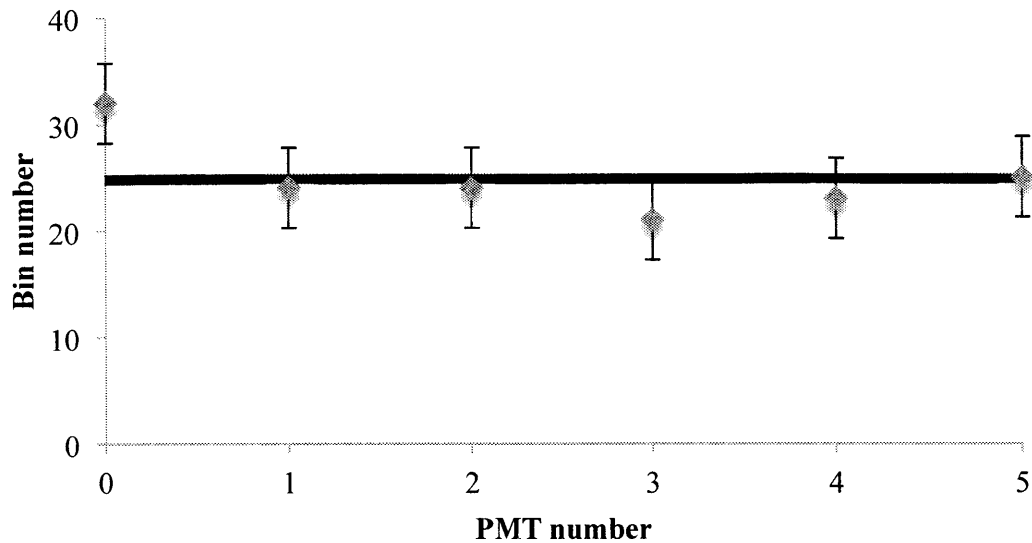


Figure 6-8. Distribution of low-energy peaks. The line represents the average of the six.

6.3. Calibration sources

The calibration sources were selected to be as close to the experimental conditions as possible. Doing so is difficult for WCD application to long-range detection because the gammas from photofission are expected to have energies between 3 and 10 MeV, although as has been previously noted, there are essentially no individual spectral lines in this region. Thus, sources with energies close to or above 3 MeV are necessary. Calibration was conducted using the following sources: ^{60}Co , ^{232}Th , and $^{241}\text{AmBe}$.

A ^{137}Cs source was also used, but it was found that the energy of emitted gamma rays is too close to the Cherenkov threshold. Thus, the error effects were found to be too large. A 5 μCi ^{137}Cs source, which is a 661.7 keV gamma emitter, was used to verify the threshold properties of the detector. The ^{60}Co source emits a cascade of two gammas of energy 1173 and 1332 keV. ^{232}Th contains ^{208}Tl , which is a 2.6 MeV gamma emitter. The

full spectrum of ^{232}Th measured experimentally with HPGe detector is shown in Figure 6-9. Note that there are a variety of gamma rays in addition to the 2.6 MeV gamma. Characteristics of the check sources along with high-intensity sources used in the experiments are provided in Table 6-2. The detector-source setup is illustrated in Figure 6-10. Note that the source position remained constant along the detector plane and was only moved perpendicular relative to the detector face.

Table 6-2. Summary of calibration sources.

| | Initial Activity Level | Half-Life (years) | Activity as of 1/06/2011 | Characteristic Radiation |
|------------------------------|-------------------------------|--------------------------|---------------------------------|---|
| Check Sources | | | | |
| ^{137}Cs | 5.0 μCi | 30.02 | 1.57E+05 dps | $\gamma_1 = 661.7 \text{ keV}$ |
| ^{60}Co | 1.0 μCi | 5.27 | 1.44E+04 dps | $\gamma_1 = 1332.5 \text{ keV}$ $\gamma_2 = 1173.2 \text{ keV}$ |
| High Activity Sources | | | | |
| ^{137}Cs | 800 μCi | 30.02 | 2.82E+07 dps | $\gamma_1 = 661.7 \text{ keV}$ |
| ^{60}Co | 1.8 mCi | 5.27 | 6.66E+07 dps | $\gamma_1 = 1332.5 \text{ keV}$ $\gamma_2 = 1173.2 \text{ keV}$ |
| $^{241}\text{AmBe}$ | 10 mCi | 433 | 2.44E+04 dps (neutrons) | Neutrons with $\gamma = 4.4 \text{ MeV}$ (70% of the time) |
| ^{232}Th | 0.3 mCi | 1.40E+10 | 1.11E+07 dps | $\gamma_1 = 2614.5 \text{ keV}$ (and other gamma rays, see Figure 6-2) |

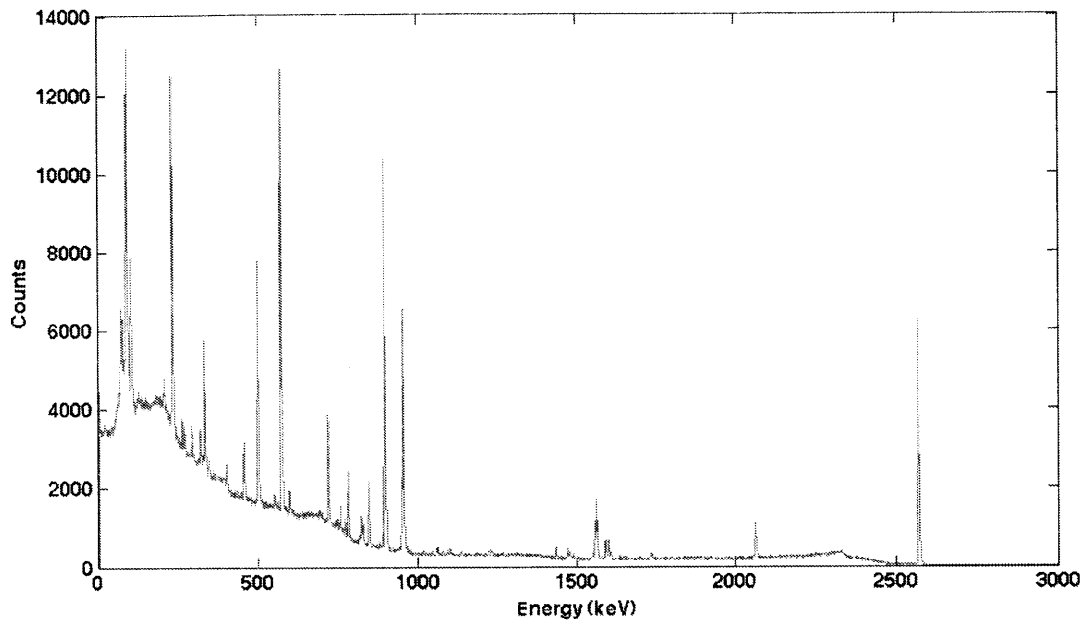


Figure 6-9. A spectrum of thorium slug using an HPGe detector showing the many gamma ray lines originating from daughters of ^{232}Th . The 2.6 MeV gamma ray originates from the decay of ^{208}Tl to ^{208}Pb , but ^{208}Tl is only reached about 30% of the time. (100 second run)

A combination of the above sources can help with monitoring energy linearity, detector stability and resolution. ^{232}Th was also used to set initial energy cutoff because of its 2.6 MeV gammas.

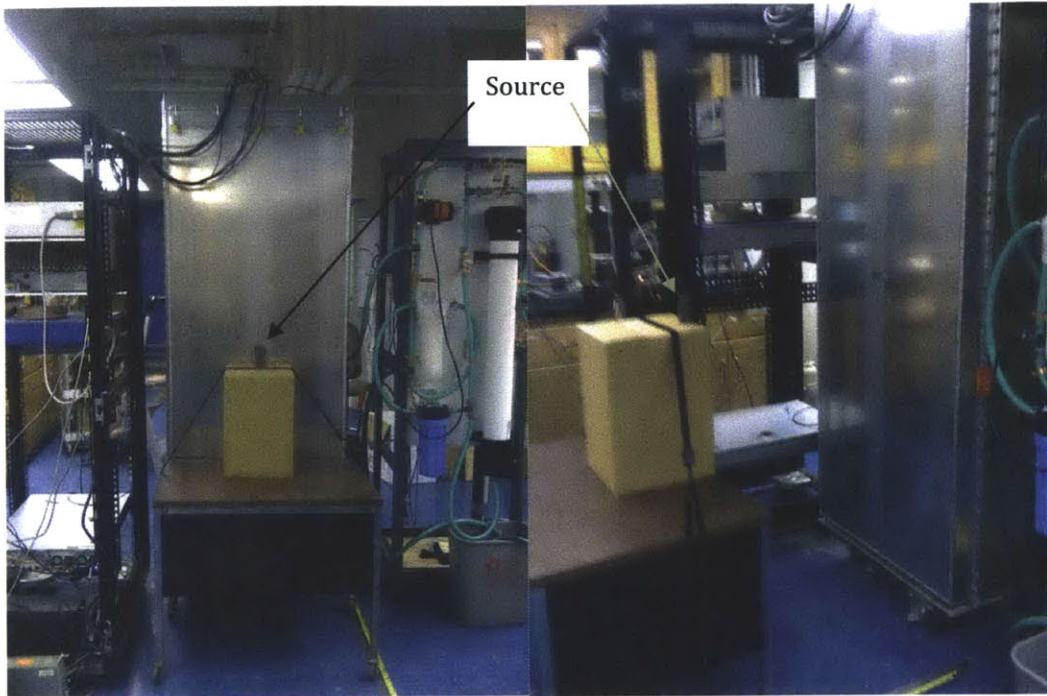


Figure 6-10. Detector and source setup. Source can be moved perpendicularly to the detector surface.

6.4. Results of detector calibration

The detector was calibrated using the sources described in Table 6-2. The responses of individual PMTs were integrated to produce a pulse height spectra corresponding to each source. The experimental background-subtracted spectra are plotted in Figure 6-11. The spectra shown are the total-absorption peaks. Similar sources were simulated using a Geant4 model. The results obtained are presented in Figure 6-12. There is a similarity between the two sets of results, especially for higher-energy part of the spectrum.

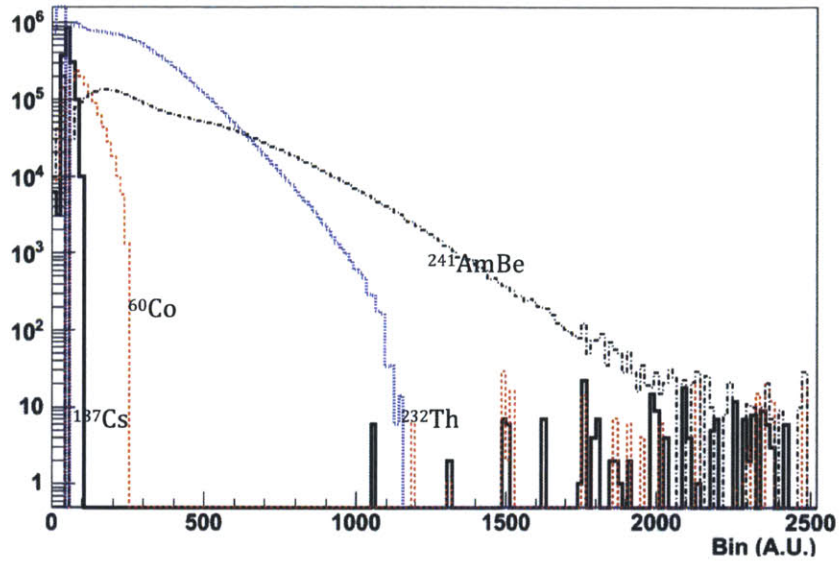


Figure 6-11. Experimental integrated spectra of four sources.

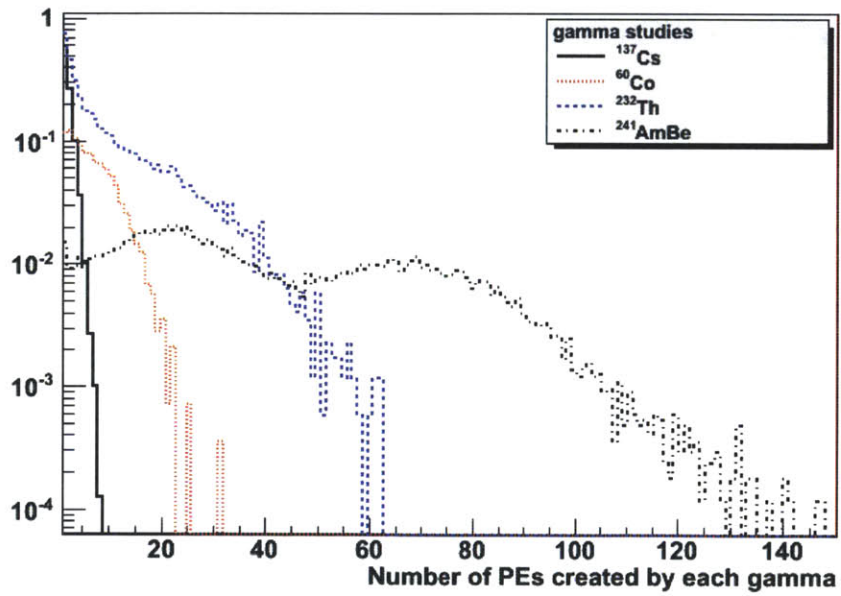


Figure 6-12. Computational (Geant4) integrated spectra of four sources (normalized).

One of the main issues for the water-based Cherenkov detector calibration is determining which feature to use for calibration purposes. The energy of the maximum of the peak is unknown because of the nature of Cherenkov photon production in the tank. The problem with using the peaks becomes even more pronounced when the calibration sources do not emit monoenergetic gamma rays, but rather produce radiation with a variety of energies, as in case of ^{232}Th . However, one feature of the Cherenkov spectrum that can be used for energy calibration is the highest energy in the spectrum, the terminal end of the peak. The terminal end corresponds to the maximum possible energy deposition in the detector by muons.

Figure 6-13 illustrates the potential technique of Cherenkov detector energy calibration. The terminal energy (MCA bin or computational number of photoelectrons) of the peak is estimated. The estimate can be plotted against the corresponding energy of the particle. The slope of the line can be used to calculate the calibration parameters. Besides the convenience of this method, using the terminal energy guarantees that when the detection threshold is placed, it will not be exceeded by a particle of lesser energy.

The terminal energy was estimated by fitting the peak by a Gaussian distribution, and the extrapolation to x-axis was taken as the end of the peak. Note that the error bars shown in Figure 6-13 correspond to $\pm\sigma$, where σ is the standard deviation of the fitted peak. The reason for such a conservative estimate of the error associated with the terminal energy is the fuzziness of the data in the tail of the pulse height spectrum. The peaks broaden as the energy of the incident particles increases.

The experimental calibration of the detector is shown as Equation 6-2, where energy is in MeV and ADCBin is the ADC bin corresponding to the terminal bin of the peak.

$$E = 565.8 \cdot \text{ADCBin} - 452.4 \quad \text{Eq. 6-2}$$

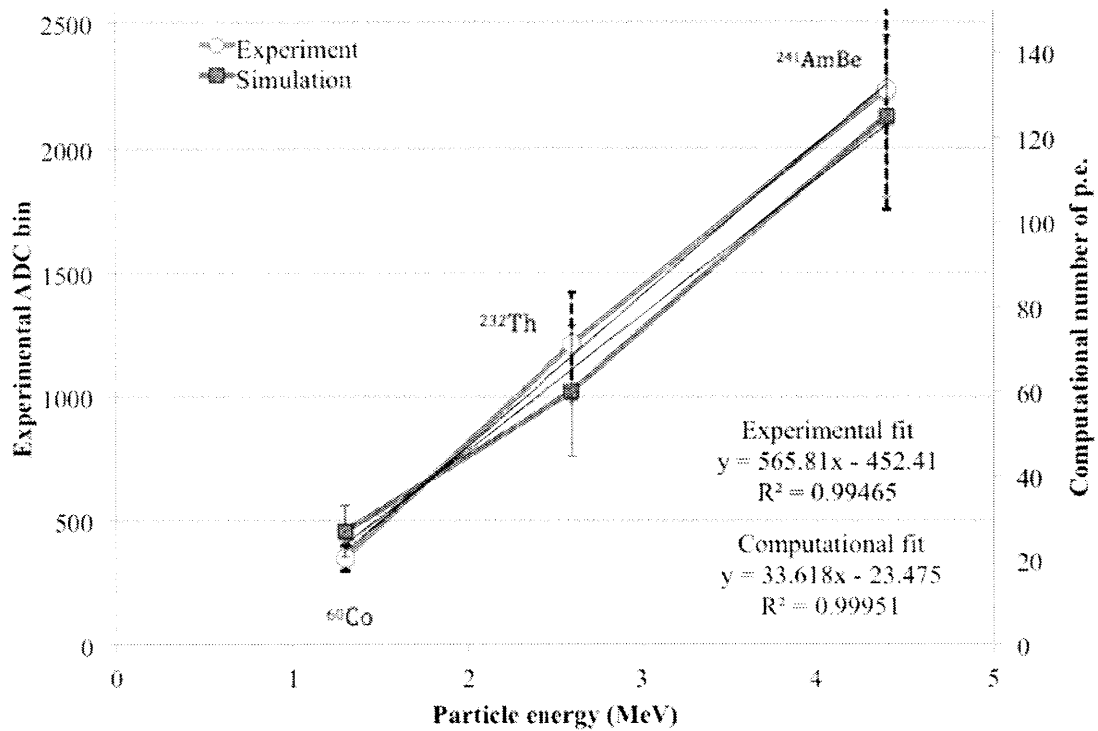


Figure 6-13. Comparison of experimental and computational calibration. The units are different for experimental and computational data sets, but the slope is nearly the same.

6.5. Dead time effects

The dead time of the detector is defined as the time which has to pass between the registration of one set of particles and being able to register the next. During the dead time, the system generally cannot accept a subsequent signal. In our QDC system, the dead time is a combination of the effects of signal acquisition time, data conversion time, and the readout time to memory.

The dead time affects the results of the measurement, and thus it must be accounted for. The difference between the ADC and QDC system with regard to the dead time was discussed in Chapter 5; the discussion of dead time here is for a QDC data acquisition system.

The dead time is measured using a reference pulser which is fed into the spectrum simultaneously with the data acquisition. During the measurement, the number of the reference pulses is determined by a scaler. The reference pulses are then compared with the number of pulses recorded by the system. All of the experimental data reported in this Chapter have been dead time corrected.

Our system does not measure correlated events. Thus, there is no danger of losing correlated events, but there can be a problem with detector behavior during a high-count-rate experiment.

6.6. Efficiency of the detector

Efficiency of the detector was measured using ^{60}Co and ^{137}Cs sources. The sources were placed in front of the detector, as shown in Figure 6-9, and the source bench was moved away from the detector in 50 cm increments. This was done so the angular dependence of the count rate could be determined. Figure 6-14 shows the summed spectra for background and the ^{60}Co source. Note that the muon peak overlaps for all cases. Figures 6-15 and 6-16 show zoomed-in background-subtracted ^{60}Co spectra. Figure 6-17 shows background-subtracted data for ^{137}Cs source. The background-subtracted histograms were integrated to get the total number of counts. The summary of integrated count rates as well as calculated intrinsic efficiencies is provided in Table 6-3. Note that the activity of ^{137}Cs source corresponds to 3 check sources (5 μCi each).

The count rates of the detector with various sources were normalized using the dead time correction discussed in Section 6-5. The summary of live pulser data used for normalization is provided in Table 6-4.

The calculation of the detector efficiency revealed that the detector is capable of detecting small amounts of radioactive material. The results of efficiency measurements using ^{60}Co source are statistically significant and are well above the threshold. However, the measurements performed with ^{137}Cs are questionable. It was expected that the detector would not be able to pick up any signal from ^{137}Cs check source because of low-energy gamma rays emitted by a low-intensity source.

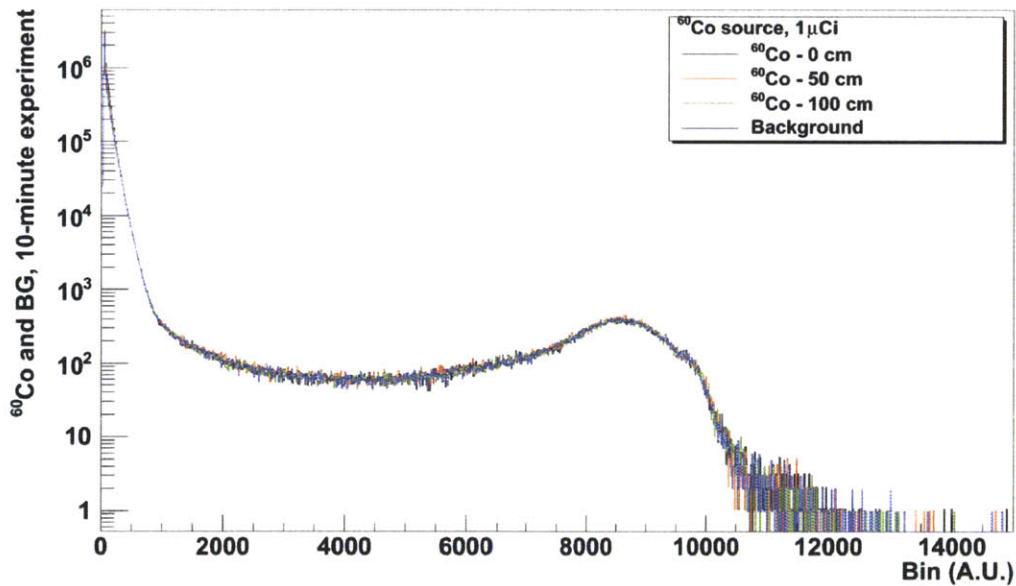


Figure 6-14. Spectrum of background and ^{60}Co source.

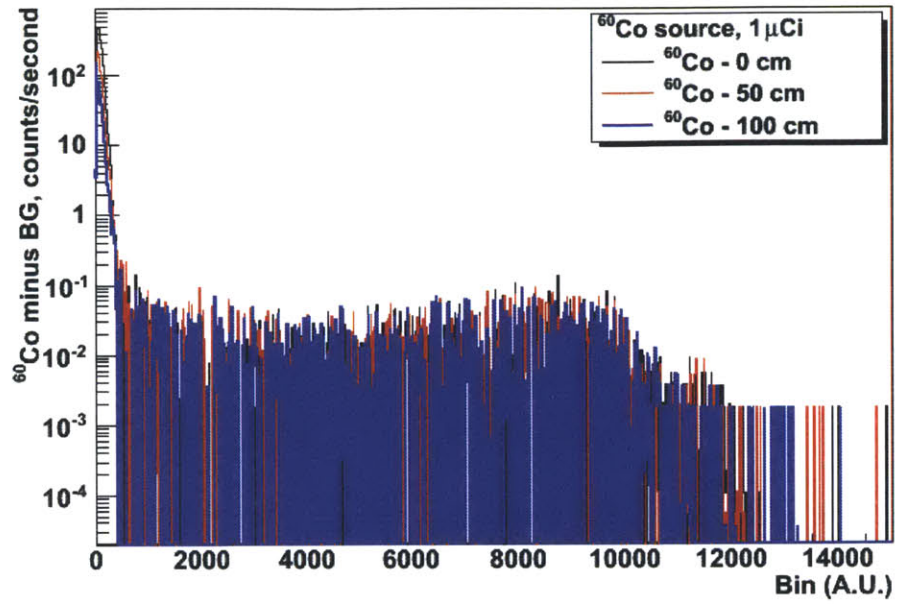


Figure 6-15. Spectrum of ^{60}Co source after background was subtracted. Note that y-axis is now count rate per second.

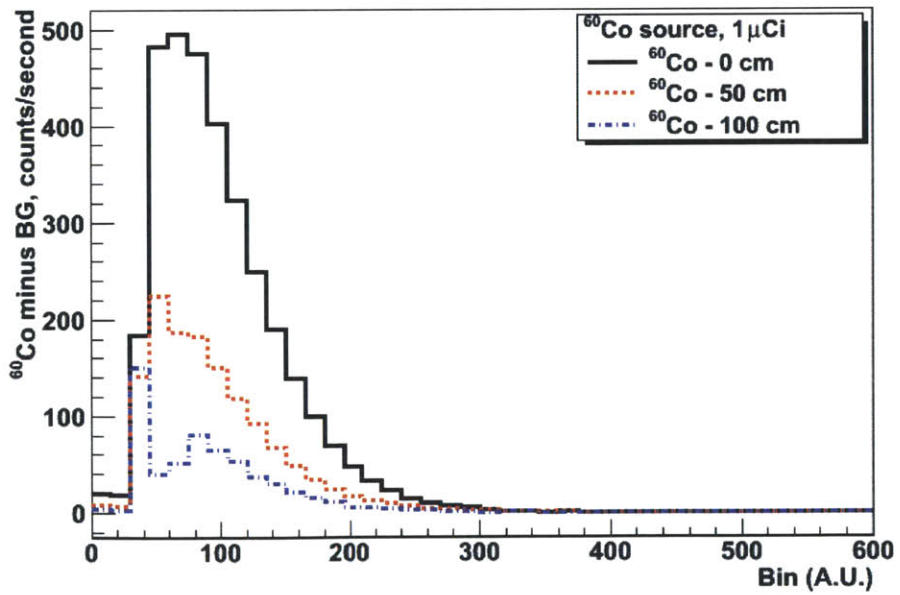


Figure 6-16. Spectrum of ^{60}Co source after background was subtracted.

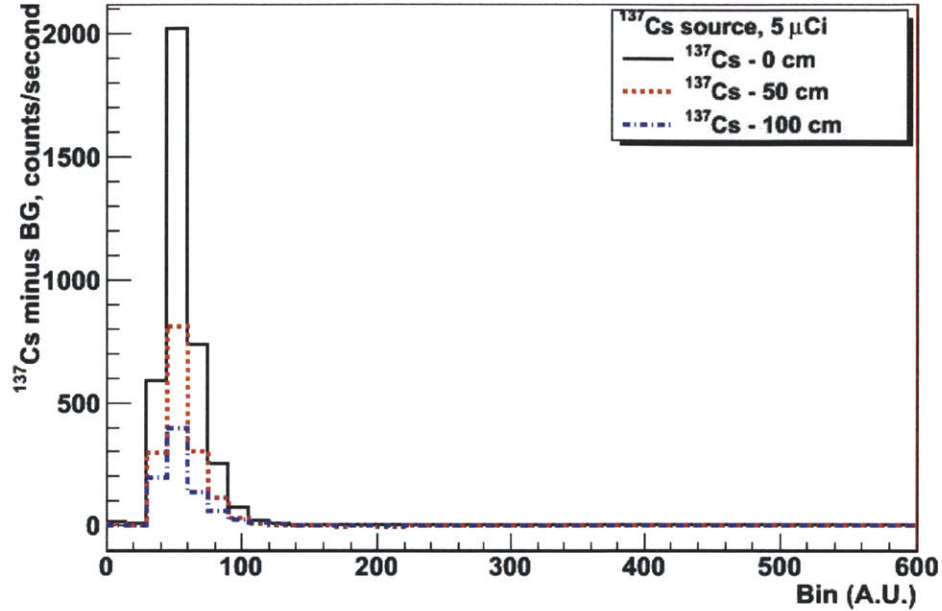


Figure 6-17. Spectrum of ^{137}Cs source after background was subtracted. Note that ^{137}Cs is actually 15 microCi.

Table 6-3. Summary of detector count rates for ^{137}Cs (3 check sources) and ^{60}Co sources.

| | Activity today, dps | Counts per second at 0 cm | Efficiency at 0 cm | Counts at 50 cm | Counts at 100 cm |
|-------------------|---------------------|---------------------------|--------------------|-----------------|------------------|
| ^{60}Co | 14582 | 3292 | 30.1% | 1359 | 593 |
| ^{137}Cs | 470316 | 3669 | 1.56% | 1812 | 761 |

Table 6-4. Summary of live pulser data used for normalization.

| | BG | ^{137}Cs 0 cm | ^{137}Cs 50 cm | ^{137}Cs 100 cm | ^{60}Co 0 cm | ^{60}Co 50 cm | ^{60}Co 100 cm |
|-------------|---------|---------------------------|----------------------------|-----------------------------|--------------------------|---------------------------|----------------------------|
| Live pulser | 4684455 | 4414846 | 4462994 | 4625984 | 4403227 | 4536396 | 4591942 |
| Raw pulser | 5969548 | 5969535 | 5843861 | 5969540 | 5906697 | 5885752 | 5906699 |

7. Event reconstruction methodology

The data output of the detector appears in the form of raw-data digitized electronic signals. Setup of the electronics is discussed in detail in Chapter 5. In this Chapter, a process of converting the digitized detector signal data collected during the experiment into meaningful physical information while recognizing the limitations of the detection system is discussed. Such a process is generally referred to as event reconstruction.

The event reconstruction process can be divided into two main parts: local reconstruction and global reconstruction. Local reconstruction is collection and analysis of the events from individual detector modules, for example energy measurement of a particle in Cherenkov detectors. The global reconstruction process combines information from all individual modules of the detection system, for example data from neutron and gamma ray detectors, in order to produce high-level triggering. A combination of information from multiple detectors can yield information about interrogated material. In this Chapter, local event reconstruction is discussed.

The energy resolution of Cherenkov detectors discussed in Chapter 6 affects our ability to fully reconstruct the initial physical process. Total event reconstruction is not necessary with Cherenkov counters in a remote detection application because the energies of the photofission products appear smeared rather than discrete. The purpose of the event reconstruction as applied to Cherenkov detectors is to determine whether the detected signal is due to gamma rays from photofission or from background.

7.1.Characteristics of the signal

Knowledge of the characteristic signal is an important part of the event reconstruction. Depending on the source of the signal and detector configuration, various interaction spectra can be produced. The interaction spectrum can be characterized as a combination of the incident particle flux, the interaction cross section, and the efficiency of the detector. The simulated^f normalized flux of gamma rays incident on the detector as a result of photofission is shown in Figure 7-1. Note that the interrogation target is 50 m away from the detector, and the flux is a function of energy. The signal is 100 milliseconds after that interrogation pulse.

The flux for materials containing HEU and DU is at least an order of magnitude higher than the one induced in the background. The energies of interest are between 3 and 10 MeV. Note that aside from the larger magnitude of the signal produced by the interrogated unshielded HEU and DU vs. background, there is a clear distinction between the two. However, identification of the nature of the signal might not be possible with a Cherenkov detector because the presence of shielding can alter the absolute magnitude. This effect can be observed when shielded HEU and DU signals are compared. The difference between the two is not significant enough to declare which material produced the signal, but it is sufficient to declare whether a SNM is present.

^f This simulation was done in MCNPX by Eric Johnson.

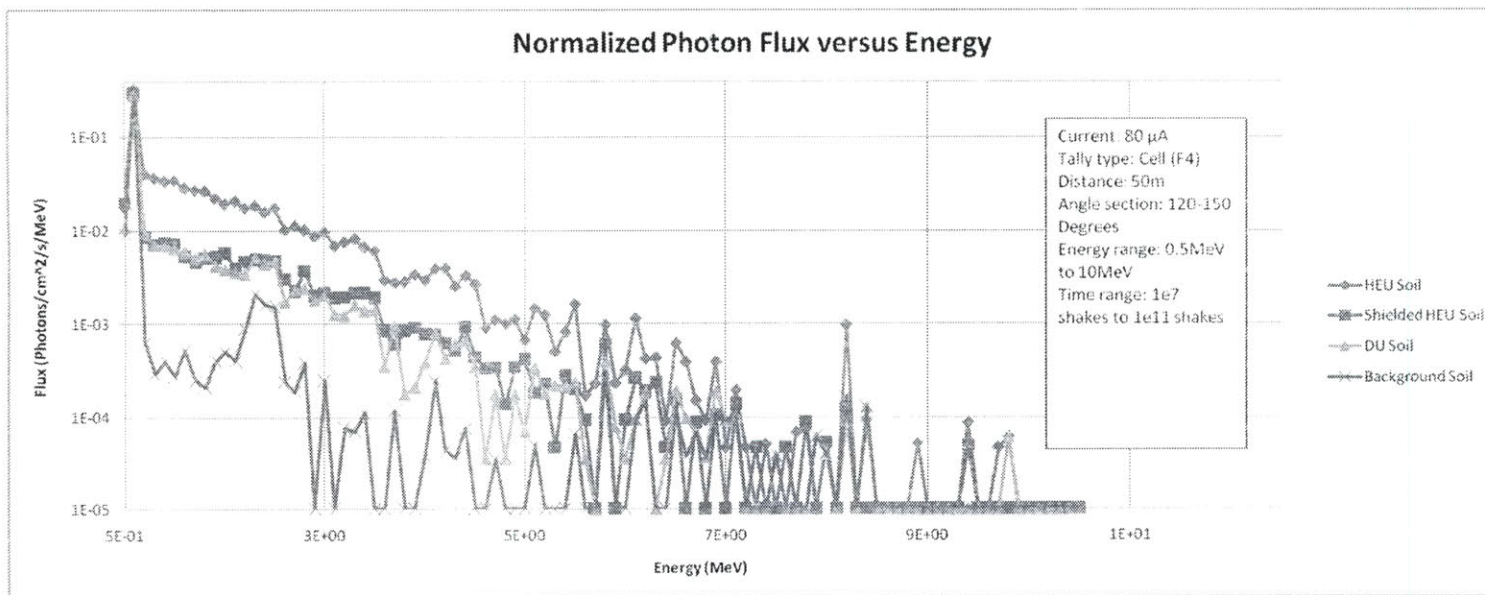


Figure 7-1. Expected signal from various target interrogations. The photon energies shown in the plot are 0.5 to 10 MeV. The time cutoff is 100 msec after the interrogation. [1 shake = 10 ns (10^{-8} s)]

7.2. Ambient and cosmogenic background

Understanding the background and how it can affect the signal is part of the event reconstruction. Low-energy background affects the signal-to-noise ratio in the detector making it difficult to determine whether a real signal was registered. Heusser⁵⁶ pointed out that while count rate directly affects the sensitivity of the detector, the effect of the background is more severe because of the inverse of the square root dependence. Heusser also indicated that environmental radioactivity is one of the more important contributors to the background radiation, although the importance depends on a particular problem.

The most problematic radioactive ambient background gammas are from ^{232}Th and ^{238}U decay series. The prompt beta-gamma cascades near the end of the series have high energies. In addition, high-energy gammas can be produced by free neutron capture. Gamma rays from ^{237}Np and ^{235}U series of naturally occurring decay chains have significantly lower energies. The decay chains of ^{232}Th and ^{238}U are shown in Figure 7-2. Important isotopes and energies of gamma rays associated with these two decay chains⁵⁷ are listed in Table 7-1.

The background spectrum in the laboratory was taken with a HPGe detector. The spectrum is shown in Figure 7-3. Note that most of the characteristic radiation listed in Table 7-1 appear in the spectrum. Two primary non-series radionuclides contributing to ambient background are ^{40}K and ^{87}Rb . ^{40}K emits a beta particle (87.3%) and a gamma ray through electron conversion (10.67%).⁵⁸ The energy of the emitted gamma is 1.46 MeV (highlighted in Figure 7-3). ^{87}Rb decays through an electron emission with low, 0.283 MeV, energy.

Jagam and Simpson⁵⁹ compiled a database of measurements of Th, U and K concentrations in various materials including cement, ceramics, glasses, and aluminum. Their report included several tables of radioactivity levels using direct gamma ray

counting via neutron activation analysis.

| | 81 | 82 | 83 | 84 | 85 | 86 | 87 | 88 | 89 | 90 | 91 | 92 |
|-----|---------------|---------------|---------------|---------------|--------|---------------|--------|---------------|---------------|---------------|---------------|--------------|
| 148 | | | | | | | | | | | | U-240 |
| 147 | | | | | | | | | | Th-237 | | U-239 |
| 146 | | | | | | | | | | Th-236 | Pu-237 | U-238 |
| 145 | | | | | | | | | | Th-235 | Pu-236 | U-237 |
| 144 | | | | | | | | | | Th-234 | Pu-235 | U-236 |
| 143 | | | | | | | | | | Th-233 | Pa-234 | U-235 |
| 142 | | | | | | | | | | Th-232 | Pu-233 | U-234 |
| 141 | | | | | | | | Ra-229 | | Th-231 | Pu-232 | U-233 |
| 140 | | | | | | | | Ra-228 | Ac-229 | Th-230 | Pu-231 | U-232 |
| 139 | | | | | | | | Ra-227 | Ac-228 | Th-229 | Pu-230 | U-231 |
| 138 | | | | | | | | Ra-226 | Ac-227 | Th-228 | | U-230 |
| 137 | | | | | | | | Ra-225 | Ac-226 | Th-227 | | |
| 136 | | | | | | Rn-222 | Fr-223 | Ra-224 | Ac-225 | Th-226 | | |
| 135 | | | | | | Rn-221 | Fr-222 | Ra-223 | Ac-224 | | | |
| 134 | | | | Po-218 | At-219 | Rn-220 | Fr-221 | Ra-222 | | | | |
| 133 | | | | Po-217 | At-218 | Rn-219 | | | | | | |
| 132 | | Pb-214 | Bi-215 | Po-216 | At-217 | Ra-218 | | | | | | |
| 131 | | Pb-213 | Bi-214 | Po-215 | At-216 | | | | | | | |
| 130 | | Pb-212 | Bi-213 | Po-214 | At-215 | | | | | | | |
| 129 | | Pb-211 | Bi-212 | Po-213 | At-214 | | | | | | | |
| 128 | Tl-209 | Pb-210 | Bi-211 | Po-212 | At-213 | | | | | | | |
| 127 | Tl-208 | Pb-209 | Bi-210 | Po-211 | At-212 | | | | | | | |
| 126 | Tl-207 | Pb-208 | Bi-209 | Po-210 | At-211 | | | | | | | |
| 125 | Tl-206 | Pb-207 | Bi-208 | | At-210 | | | | | | | |
| 124 | Tl-205 | Pb-206 | Bi-207 | | | | | | | | | |

Figure 7-2. Decay chains of ^{232}Th and ^{238}U .

The cosmogenic background is harder to account for than ambient background. The flux of high energy (GeV and higher) cosmic rays incident on the atmosphere is on the order of 10^{18} cosmic rays per second.⁶⁰ However, because of their high energy, muons are rather easy to shield against or to veto. The problem is in what the cosmic muons can create as a result of interaction with the atmosphere, detector, and surrounding materials. First, neutrons, gamma and beta rays can be created. In addition, cosmogenic radionuclides are produced by these high-energy cosmic rays interacting with the

elements in the atmosphere and the earth. The illustration of the interaction and the progeny particles produced is shown in Figure 7-4.⁶¹ High-energy muons are also capable of increasing the dead time of the detector if not properly rejected.

Table 7-1. Decay chains and selected energies.

| Series | Isotope | Largest gamma energy (keV) | Yield (%) | Notes |
|-------------------|-------------------|----------------------------|-----------|--|
| ²³⁸ U | ²³⁴ Pa | 1313 | 18 | |
| | ²¹⁴ Bi | 2448 | 1.5 | 20 gammas with energies above 600 keV |
| | ²¹⁰ Bi | 1765 | 15.4 | |
| ²³² Th | ²²⁸ Ac | 1588 | 3.3 | 6 gammas with energies above Cherenkov threshold (420 keV) |
| | ²¹² Bi | 1621 | 1.49 | 3 gammas with energies above Cherenkov threshold (420 keV) |
| | ²⁰⁸ Tl | 2615 | 99.2 | Most characteristic gamma of ²³² Th series |

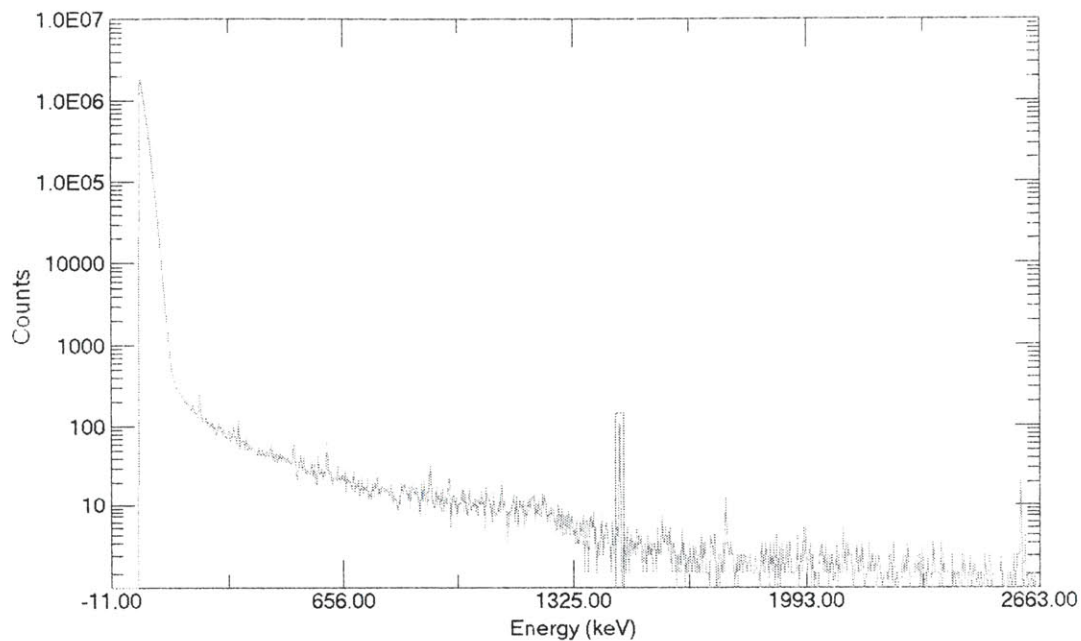


Figure 7-3. Background gamma spectrum obtained with an unshielded HPGe detector, (6293 s live time).

There are multiple radionuclides produced by the cosmic ray interactions. The most prominent are tritium and ^{14}C .⁶² However, both are beta emitters, with particle energies below the Cherenkov threshold. There are radionuclides produced by cosmic rays which are gamma emitters with energies sufficiently high to produce a signal in the detector, for example ^{22}Na (1.27 MeV) and ^{38}Cl (2.17 MeV). They will not be accounted for in the current consideration because the tropospheric concentration of such nuclides is very low.

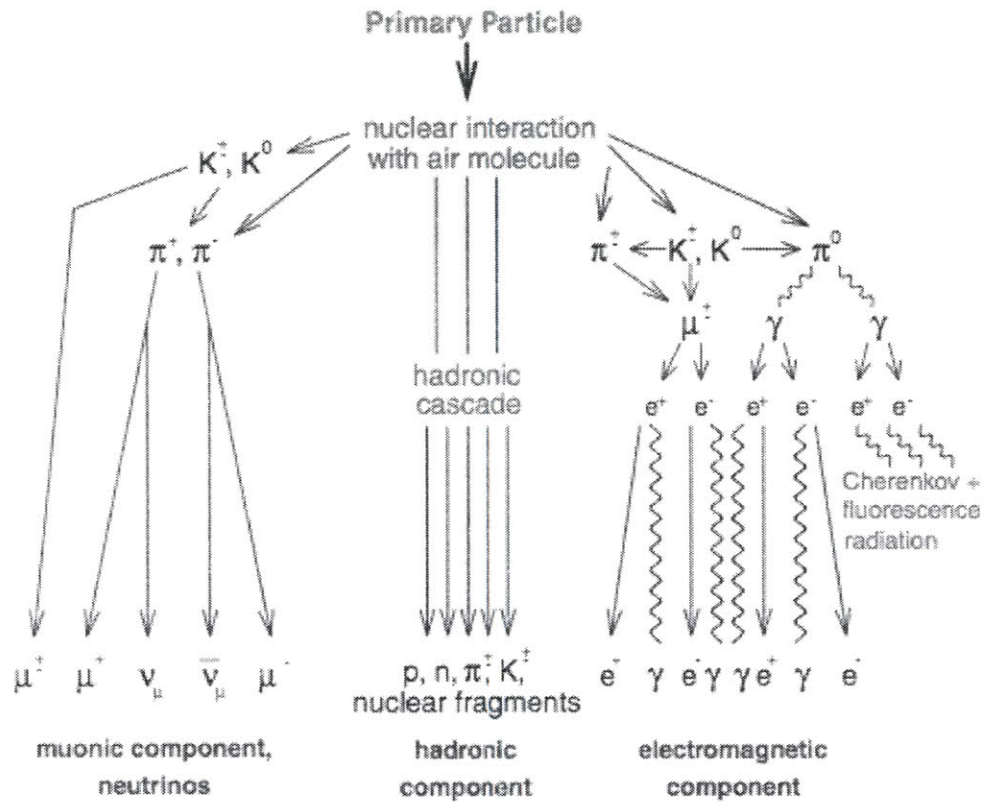


Figure 7-4. Progenies of cosmic ray interacting with the atmospheric gases and earth crust.

Cosmic rays, in particular muons, generally have very high energies well above the Cherenkov threshold. The mean energy of a muon reaching sea level is on the order of 4 GeV. Muon flux is on the order of 1 muon per cm^2 per minute. Since muons are charged particles with energies well above the Cherenkov threshold, they will create a detectable signal in the counter.

Muons are crossing the detector body at various angles. However, the muons crossing the detector vertically will result in the largest signal because of the available amount of the detector body to interact with. A muon will result in a deposition of about 2 MeV per g/cm^2 of material, most of which will turn into ionization. The amount of

energy going into Cherenkov is rather constant. This fact is used to fix the charge scale of the experiment. Because the detector properties can vary with water quality, reflectivity of the walls and stability and optical properties of the PMTs, the energy scale of vertical muons interaction can be used to continuously monitor detector operation and stability.

7.3. Background rejection methods

The choice of the background rejection method depends on the detector type, particles of interest, and the ways background can affect the ability of the detector to select the signals of interest. This particular design of Cherenkov counter was tailored for gamma ray detection. The incident gamma rays are monodirectional because of the large separation between the detector and the source. There are two types of background rejection methods that can be applied to this detector: passive and active. Passive methods generally include shielding and reduction of radioactive contaminants in the detector and surrounding materials. Active methods can include any or a combination of veto and coincidence techniques, energy cuts, signal patterns (for example, PMT majority selection or rise time), and multiple detection mechanisms.

Using gamma ray shielding on the sides of the detector not exposed to the incident flux can potentially reduce the signal from low-energy background gammas. Lead shielding is generally superior to other shielding materials. Simple Geant4 simulation was used to estimate that a 15-cm shield of lead attenuates the background gamma rays by a factor of 10^3 . One has to take into account that lead is also ideal for a muon capture[§] and subsequent generation of a neutron. These fast neutrons can induce high-energy gamma rays in lead through excitation reactions and offset the effects of shielding. In addition, the neutrons can affect the performance of ^{10}B neutron detectors if

[§] Recall that muon capture rate is proportional to Z^4 , where Z is the atomic number.

placed near lead shielding. One of the main drawbacks of lead or other high density shielding is weight. If weight is an issue because the device must be transportable, heavy shielding may not be acceptable.

Reduction of the radioactive nuclides present in the detector components and surrounding materials can be done through material screening and purification. This is a background reduction method, not necessarily rejection, and it is beyond the scope of this work. An extensive review of radionuclide reduction was done by Leonard et al.⁶³

The report included results of direct gamma counting, alpha counting, neutron activation analysis, and high-sensitivity mass spectrometry, and provided thorough analysis of each technique.

The active methods of background rejection when this particular design of water Cherenkov detector is considered are veto and coincidence techniques, energy cuts, and PMT majority selection. The veto techniques are generally used to reduce the background due to muons, especially if the detector is large, on the order of a ton of active volume. The approach is to surround the detector with other detectors that will function in an anticoincidence mode with the primary detector. For example, 2-cm thick plastic scintillator paddles of various sizes were used in anticoincidence mode with a 0.64-ton liquid scintillator reactor antineutrino detector deployed at San Onofre Nuclear Generating Station (SONGS).³³

The next two methods described are directly applicable to the current design of the detector: setting an energy threshold based on energy discrimination and implementing PMT majority selection. With energy discrimination, only events with energies above a certain threshold are recorded. This is particularly useful for the detection of gamma rays from fission and photofission because they arrive with a distribution of energies. As was shown in Figure 7-1, the gamma rays of interest can have energies between 3 and 10 MeV, while the background gamma rays are mostly below 3

MeV. Thus, realizing where to place an energy setting in the spectrum would allow rejection of events produced by low-energy particles.

The second method is based on using the coincidence between PMT responses to the incident particles. For example, only the events that trigger two PMTs or more are recorded. This method is especially useful when dark currents of PMTs must be reduced. Figure 7-5 illustrates changes in background count rates when majority is enforced. Note that the low-energy part of the spectrum is significantly reduced when any two or more (or three or more) PMTs are triggered in coincidence. As was discussed earlier, the muons deposit such large amounts of energy to the detector, so they practically affect all of the PMTs. This can be observed by looking at the muon peak which is unaffected by majority settings.

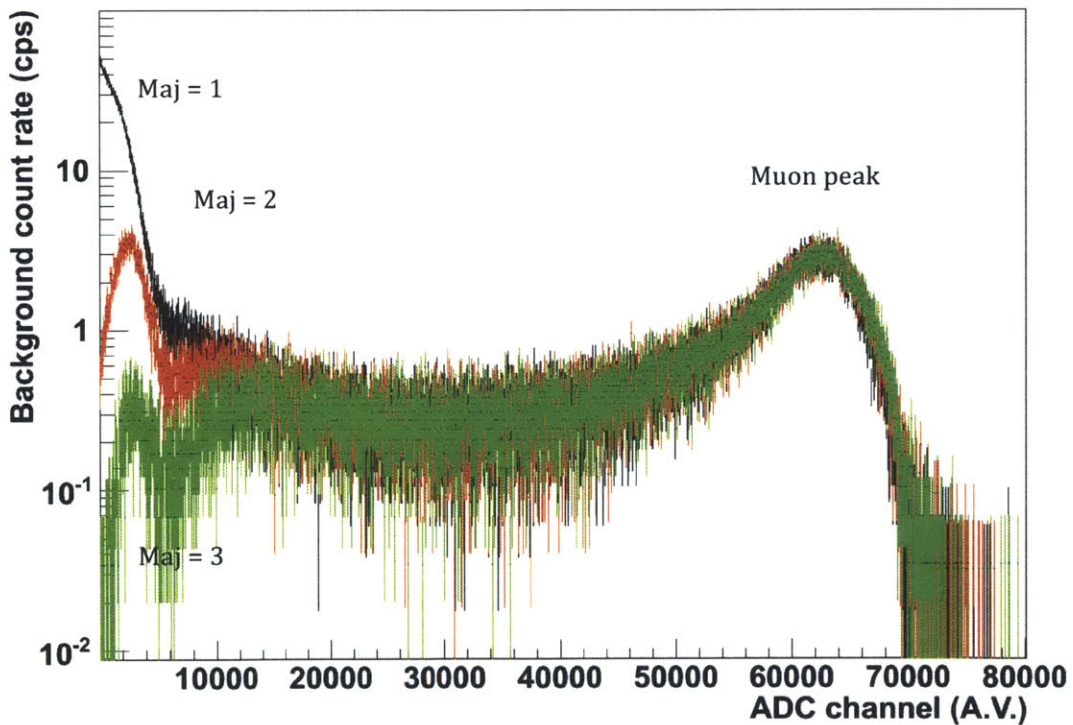


Figure 7-5. Background rates in the Cherenkov tank with majority settings of 1, 2, and 3 PMTs.

7.4. Final (simulated) event sample

The selection criteria for the analysis of reconstructed objects were designed using Geant4 simulation. Using the Geant4 model first, we showed that the detector calibration might be possible using ^{60}Co , ^{232}Th and $^{241}\text{AmBe}$ sources. The calibration was experimentally verified using the same sources. The calibration of the detector revealed possible energy cutoffs.

The final study of the detector performance was done using $^{241}\text{AmBe}$ source. The event was both simulated in Geant4 and studied experimentally to determine the signal efficiency and the capability of background rejection. $^{241}\text{AmBe}$ source was used in order to investigate the detector response to monoenergetic gamma rays as well as neutrons.

7.4.1. Simulation of $^{241}\text{AmBe}$ source

$^{241}\text{AmBe}$ is a neutron and gamma source emitted through the $^9\text{Be}(\alpha, n) ^{12}\text{C}$ reaction. The following three reactions⁶⁴ are relevant in an AmBe system:

1. $^{13}\text{C}^* \rightarrow ^{12}\text{C} + n$
2. $^{13}\text{C}^* \rightarrow ^{12}\text{C}^* + n \rightarrow ^{12}\text{C} + n + \gamma (4.43 \text{ MeV})$
3. $^{13}\text{C}^* \rightarrow ^{12}\text{C}^* + n \rightarrow ^8\text{Be} + n + \alpha \rightarrow n + 3\alpha$

All three reactions result in a neutron emission, but only one of them produces a gamma ray. Simplified schematic of $^{241}\text{AmBe}$ source is illustrated in Figure 7-6. Venkataraman et al.⁶⁴ pointed out that the ratio of gamma to neutron emission is 0.75. More recent experimental results of the gamma-neutron ratio measurements were reported by Liu et al.⁶⁵ The recommended value was $0.575 \pm 4.8\%$. Their result is more consistent with the value of $0.56 \pm 6\%$ reported by Kamboj and Shahani.⁶⁶ The results of

Geant4 simulation reported in this Chapter are based on the ratio of 0.575 as reported by Liu et al.⁶⁵

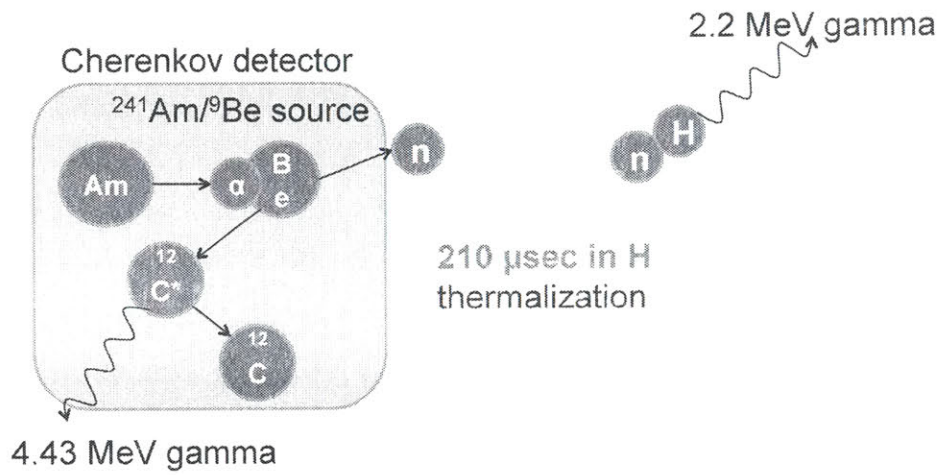


Figure 7-6. $^{241}\text{AmBe}$ source decay with neutron absorption on H in water.

The source was assumed to emit gamma rays and neutrons isotropically. The spectrum⁶⁷ of AmBe neutrons used in simulations is shown in Figure 7-7.

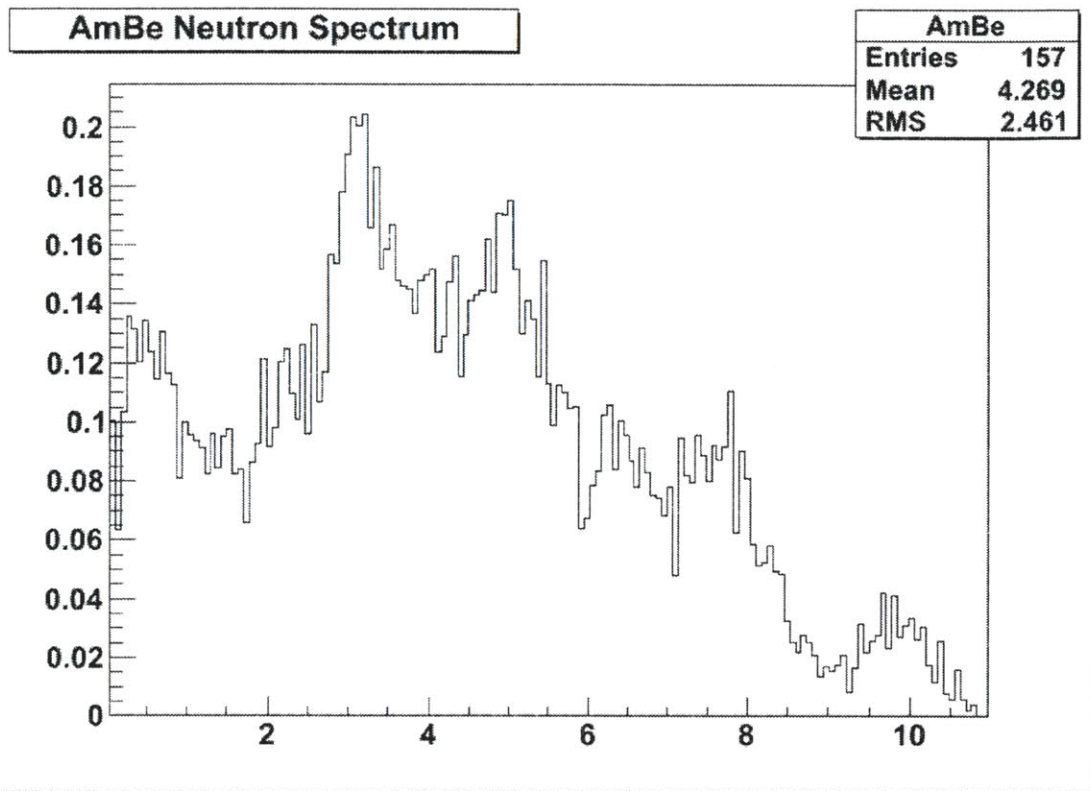


Figure 7-7. ²⁴¹AmBe source neutron spectrum.

The simulation was initially performed for a bare source near the detector. The results are presented in Figure 7-8. Two peaks were identified. The lower energy peak is due to a neutron capture on hydrogen, which results in 2.2 MeV gamma emission. The higher energy peak is due to 4.4 MeV gamma from ¹²C* de-excitation. In order to validate the above observation, a series of cuts were applied along with additional simulations.

First, an energy cut was applied to the neutron capture in the tank. To study possible peak deconvolution, the contribution of 2.2 MeV gamma rays to the signal was excluded from the simulation. The results, shown in Figure 7-8, revealed that the signal above 40 p.e. is mostly due to 4.4 MeV gamma rays. However, experimental

deconvolution would be difficult due to partial contribution of 4.4 MeV gamma rays to the 2.2 MeV peak.

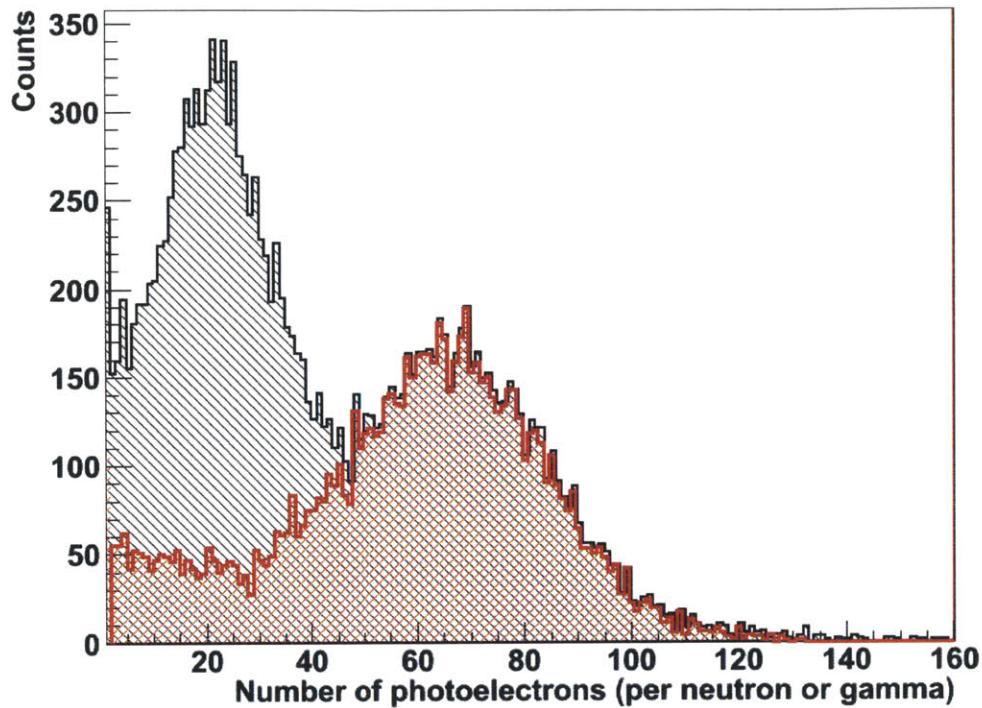


Figure 7-8. AmBe spectrum generated in Cherenkov detector. The signal due to 4.4 MeV gamma rays is shown in red.

7.4.2. Simulation cases

With simulation, it is possible to deconvolute the two peaks by simulating gamma ray and neutron interactions separately. It is difficult to do so experimentally. Thus, shielding variations and their effect on pulse height spectrum were considered because of their possible reproducibility in the lab environment.

To further study potential energy cutoffs as well as peak deconvolution, the simulation of the detector with an AmBe source included modeling of a source and shielding materials as illustrated in Figure 7-9. The source is located 10 cm away from the center of the face of the detector.

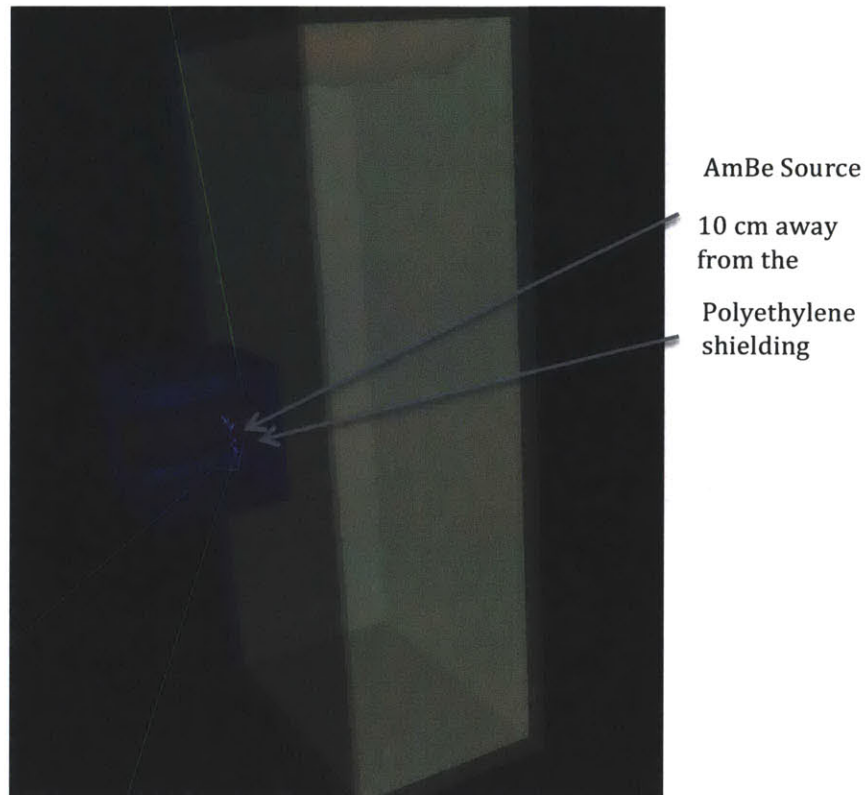


Figure 7-9. $^{241}\text{AmBe}$ source and shielding near the detector.

Three cases reproducible in an experimental environment were considered: (1) bare source, (2) source surrounded by shielding on all sides except the side between the source and the detector face (four sides), and source surrounded by polyethylene shielding on all sides (five sides). In all cases, the source remained at the same position.

Case 1, with bare source, is intended to illustrate 4.4 MeV gamma ray interactions with the detector. In addition, there will be neutrons thermalized in water and subsequently absorbed by hydrogen. Thus, the spectrum is expected to include 2.2 MeV gamma peak from hydrogen capture and 4.4 MeV gamma peak from the AmBe reaction #2 as explained in Section 7.5.1.

Case 2, with shielding on all sides except between the source and the detector, is intended to show attenuation of some of the 4.4 MeV gamma rays, but enhancement of the neutron peak. This is possible because the neutrons that would be ordinarily lost from the detector, as in case of the bare source, are thermalized and absorbed in polyethylene shielding providing the detector with additional 2.2 MeV gamma rays. Note that the neutrons incident on the face of the detector are not attenuated in polyethylene. Case 3, with polyethylene on all sides, illustrates some enhancement of the neutron peak, but mostly is there to attenuate the 4.4 MeV gamma rays.

The results of all three cases are shown in Figure 7-10. The variation of pulse height spectra is due to the effect of polyethylene shielding on gamma ray and neutron arrivals at the detector. The first peak is due to 2.2 MeV gamma rays from ^2H de-excitation. The second peak is due to 4.4 MeV gamma rays.

The 4.4 MeV peak is decreased by about 40% when a 10-cm brick of polyethylene is inserted between the source and the detector. This was checked by a quick gamma ray attenuation calculation using Equation 7-1, where I_0 is the initial intensity of the gamma source, I is the intensity of the source after the attenuator was introduced, x is the thickness of the attenuator, and μ is the attenuation coefficient of polyethylene.

$$\frac{I}{I_0} = e^{-\mu x} \quad \text{Eq. 7-1}$$

The attenuation coefficient of the polyethylene was calculated⁶⁸ to be $3.3 \cdot 10^{-2} \text{ cm}^{-1}$. The calculated decrease in intensity of gamma rays was 25.6%. This compares well with 23% value estimated using the Geant4 model.

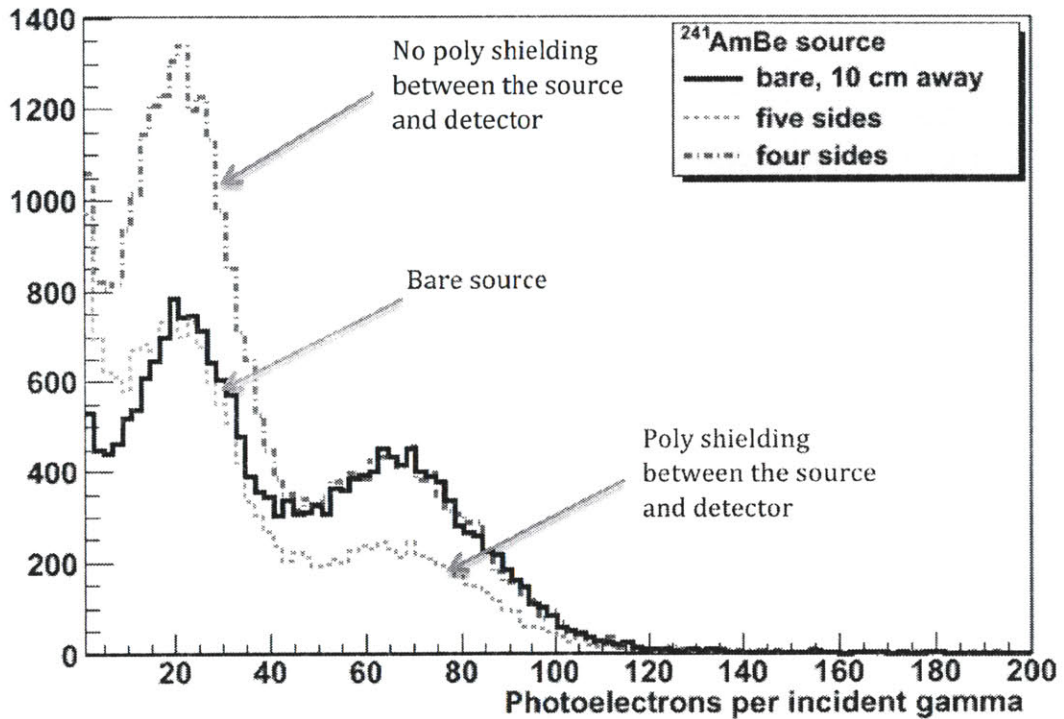


Figure 7-10. Simulation results for AmBe source.

The neutron peak (2.2 MeV gamma peak) was enhanced when the polyethylene moderator was introduced into the system. To study the neutron behavior in the detector

and the polyethylene, the sites of neutron capture were imaged using a ROOT script. The neutron captures in the detector with a bare source near it are illustrated in Figure 7-11.

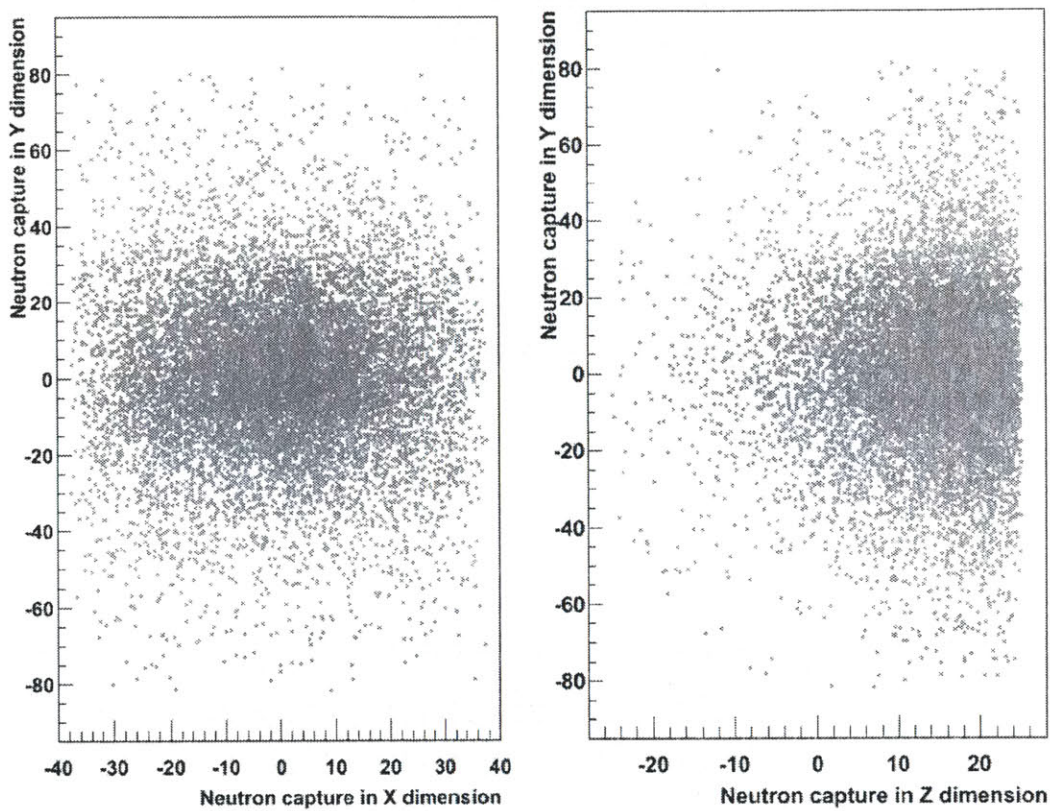


Figure 7-11. Bare source, neutron captures. The dimensions are in cm. Left: face of the detector. Right: captures along the depth of the tank.

The figure on the left shows the face of the detector that the neutrons are incident on. The figure on the right shows the neutron captures along the depth of the tank. Recall that the neutrons are emitted with a distribution of energies; thus, the capture sites are scattered.

Figure 7-12 illustrates the neutron captures in the water as well as in the polyethylene shielding. Note that the intensity of neutron captures in the tank was not changed much, but there are a lot of captures in the polyethylene.

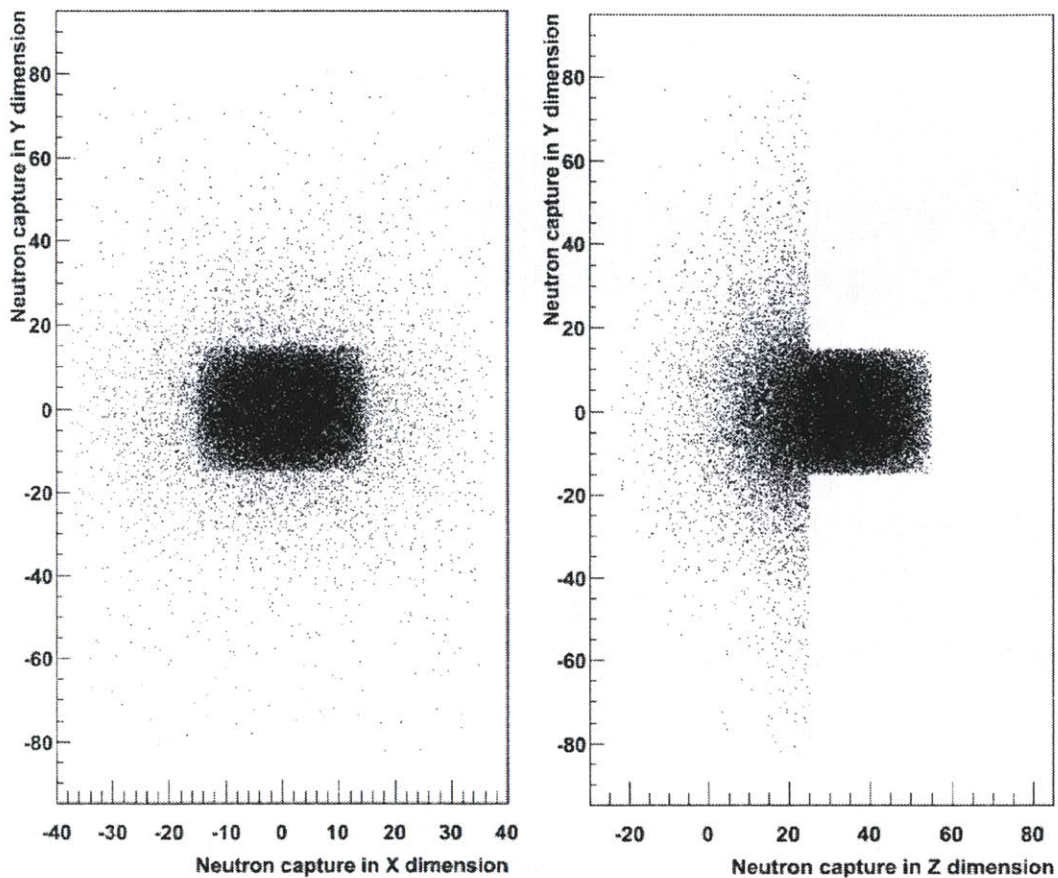


Figure 7-12. Neutron captures in the tank and in the polyethylene shielding placed on four sides around the source. No polyethylene was placed between the tank and the source.

Figure 7-13 is similar to Figure 7-12 and shows neutron captures in the water and the polyethylene. The intensity of neutron captures in the tank decreased significantly due

to the shielding between the tank and the source. The neutron peak is still higher than for the bare source case because of the additional captures in the shielding.

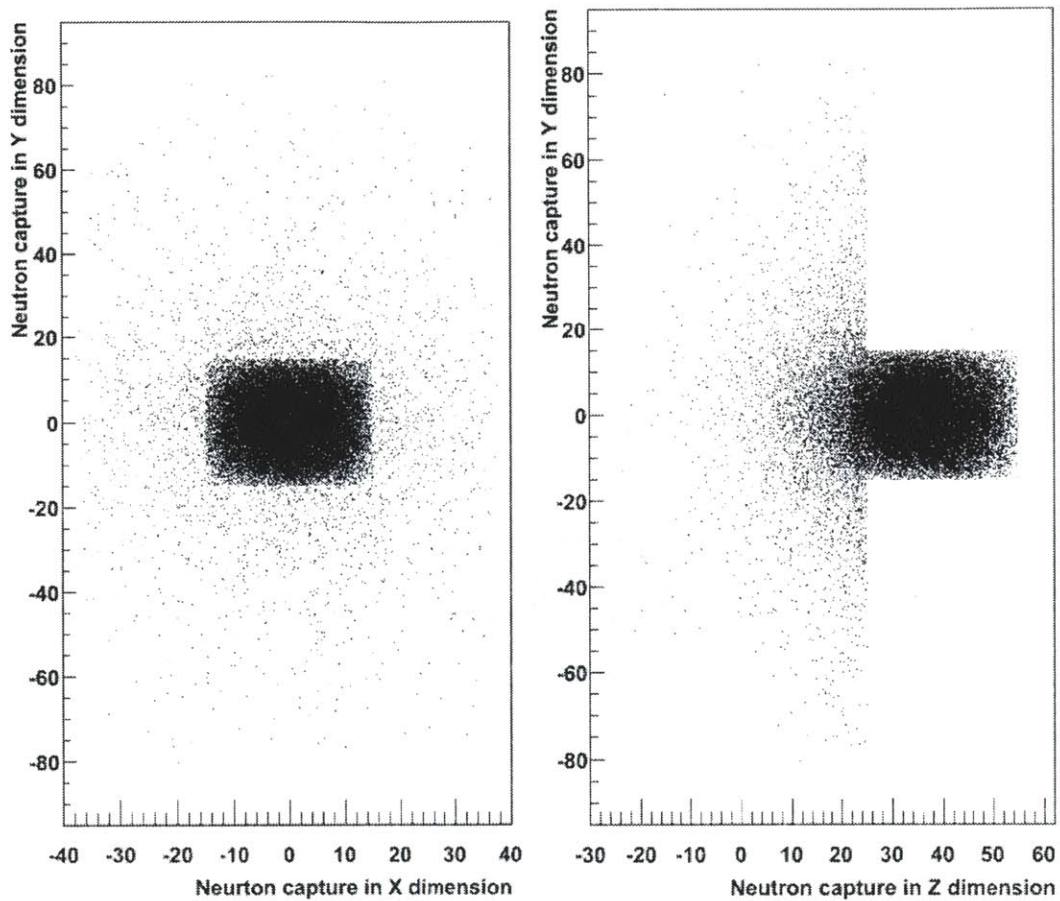


Figure 7-13. Neutron captures in the tank and in the polyethylene shielding placed on five sides around the source. 10-cm polyethylene block was placed between the tank and the source.

7.4.3. Experimental verification of $^{241}\text{AmBe}$ spectrum

The experimental setup is illustrated in Figure 7-14. A 10 mCi $^{241}\text{AmBe}$ source was observed with the WCD under three different shielding conditions to produce a significant attenuation of counts. The setup was described in detail in Sections 7.4.1 and 7.4.2. Three experimental tests were performed: (1) place bare $^{241}\text{AmBe}$ source 10 cm away from the detector face, (2) surround the source on four sides with 10 cm of polyethylene and leave one face open towards the detector, (3) place 10 cm of polyethylene between the source and the detector effectively enclosing the source in all directions with shielding.

The experiments were performed starting and ending with background measurements. PMT settings are as described in Chapter 5. The results of experimental measurements are plotted in Figure 7-15. All experimental measurements were taken for a 10-minute period. Note, that the total number of counts is plotted as a function of ADC bin. The measurements were corrected for the dead time of the detector. The muon peak position, located around bin 9000, is the same for all measurements regardless of source. This was expected since the energy deposited by a muon is much higher than of any sources. Presence of the source is clearly visible even without subtracting the background. However, the response of the detector to various polyethylene shielding configurations requires subtracting the background.

The same experimental results after background subtraction are shown in Figure 7-16. The behavior of the detector is very similar to that predicted by the model. The two peaks corresponding to the bare AmBe source predicted by the model are not as resolved in the experimental results. Thus, the additional experiments with shielding allowed discrimination between the 4.4 MeV and 2.2 MeV gamma rays based on neutron properties.

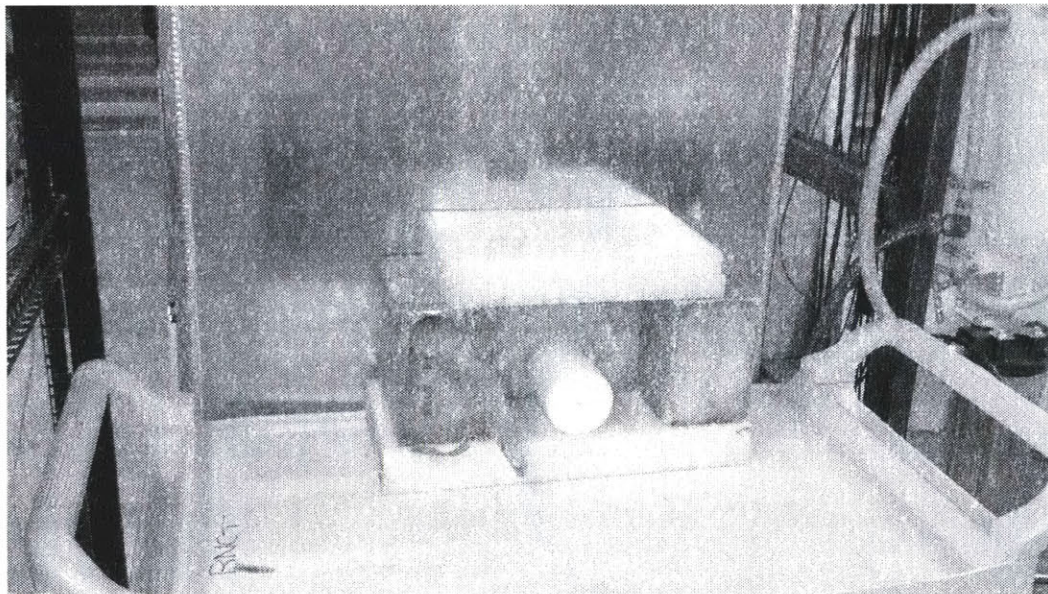
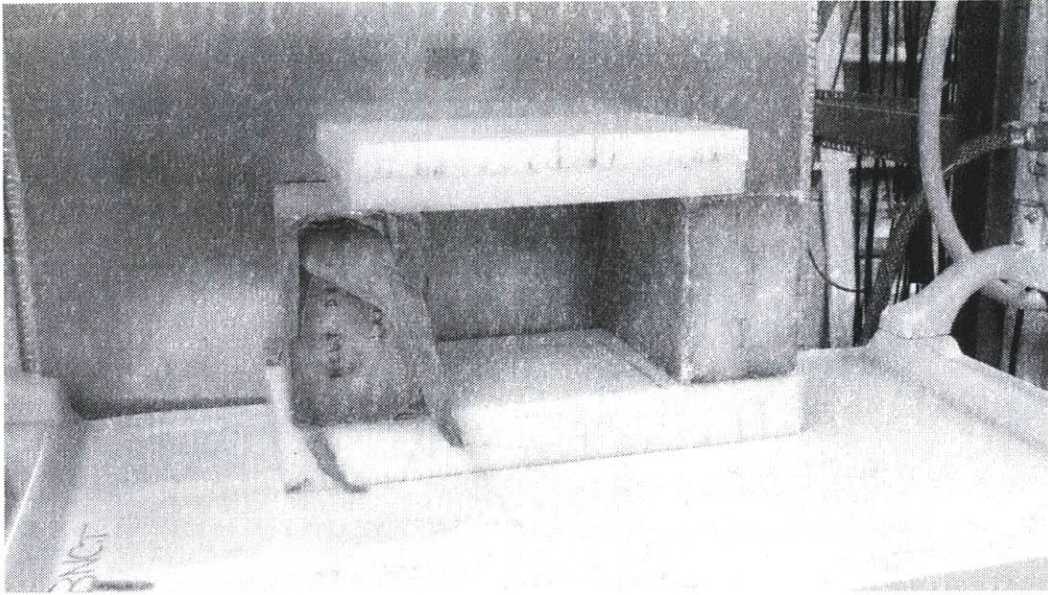


Figure 7-14. Experimental setup of AmBe source and the detector. Top: Shielding on four sides. Bottom: shielding on five sides with polyethylene between the source and the detector. The source is not shown.

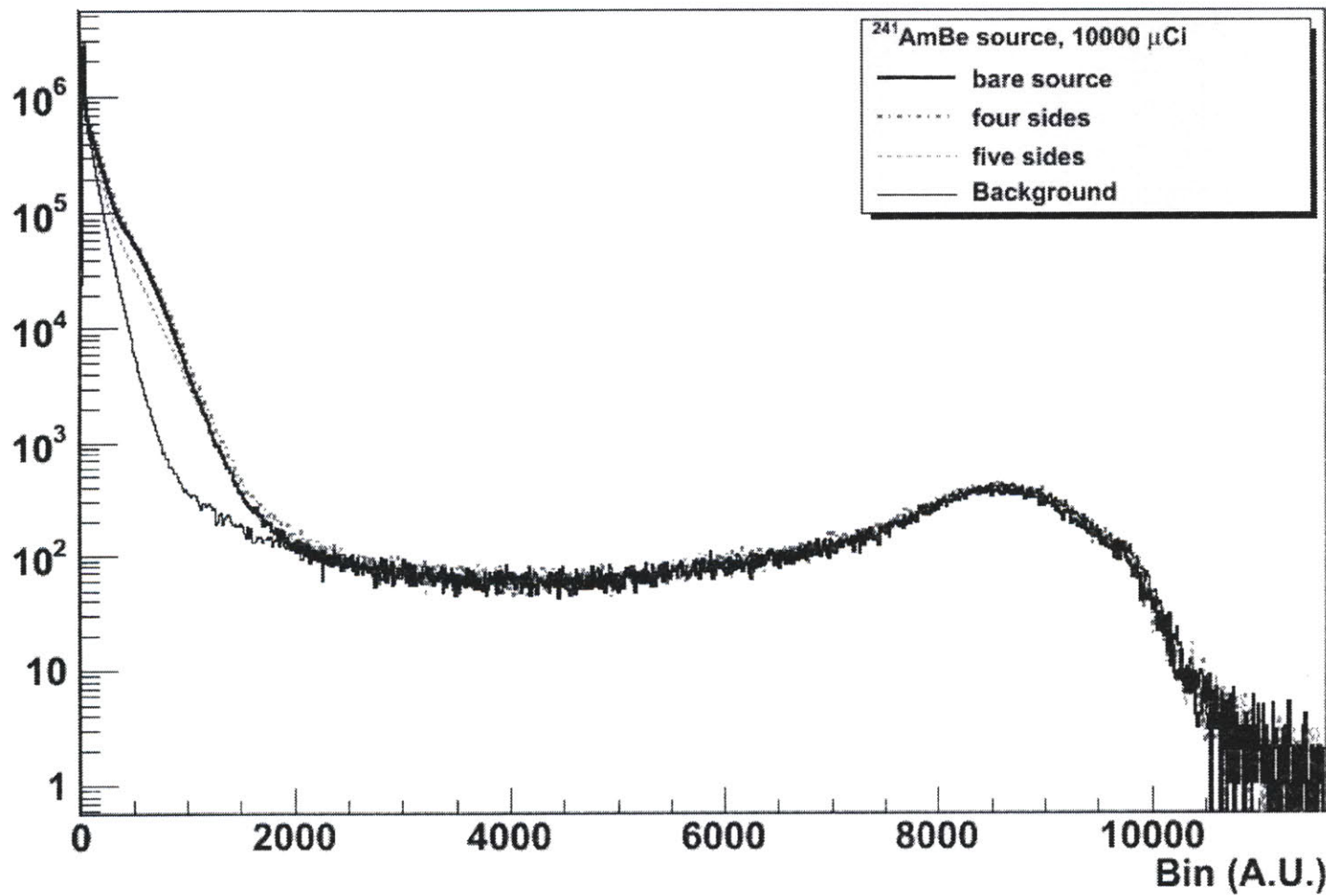


Figure 7-15. Experimental spectra obtained with AmBe source. The background is clearly distinct from the source spectra.

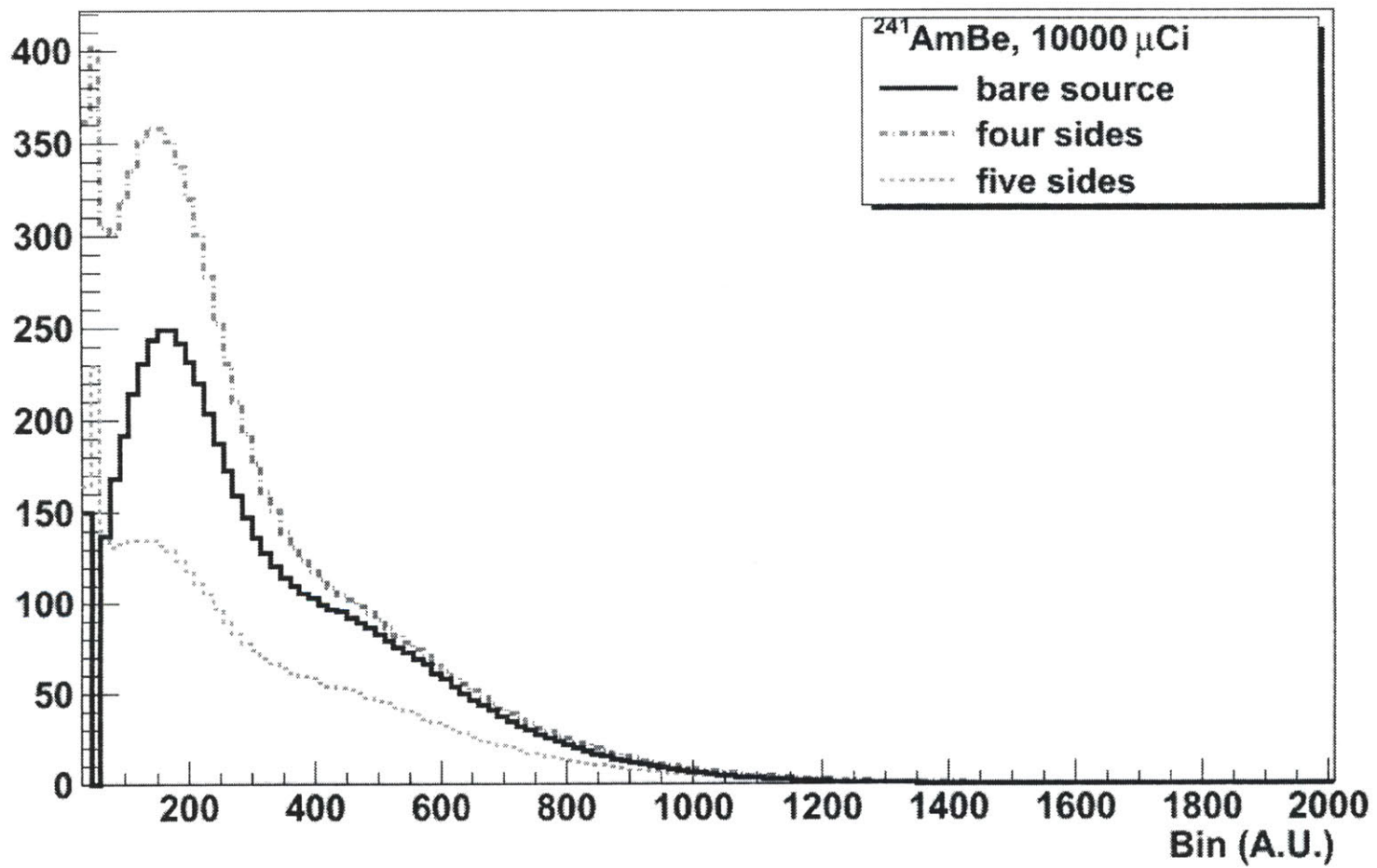


Figure 7-16. Background-subtracted AmBe spectra.

Note that when the bare source is surrounded by the polyethylene shielding on four sides, the neutron capture (2.2 MeV) peak is enhanced. The 4.4 MeV gamma ray peak is not significantly affected. However, when a 10-cm polyethylene brick is inserted between the source and the detector, there is a significant attenuation of 4.4 MeV gamma rays. This is consistent with the prediction of the computational model.

One significant difference between the model and the experiment is the decrease in 2.2 MeV peak for the “five side” case. The computational model showed almost no decrease. This could be because the computational model overestimates the quality of water or reflectivity of the detector walls. The overestimate can result in preservation of more low-energy events as compared to the actual experiment.

7.4.4. Comparison of experimental and computational results

The comparison of the experimental data and the results of computational model was not intended to be quantitative. The assumptions introduced into the model regarding the water purity and reflectivity of the walls can result in a significant difference between the pulse height spectra of experiment and simulation. In addition, simulation of the pulse-processing chain was omitted including the internal amplification and digitization of the PMT pulses. While the model accounts for the Compton scattering, statistical distribution of the generated Cherenkov light, distribution of light absorption and scattering, and statistical distribution of quantum efficiency of PMTs, the limitations of the model will contribute to more resolved spectrum as compared to the experiment. Thus, the discussion in this section is mostly qualitative.

The purpose of the simulation was to predict the behavior of the detector when certain features of the AmBe source were suppressed or enhanced. Peak deconvolution of

AmBe source is a difficult experimental task unless tagging is used. The features predicted by the simulation were then searched for in the experimental spectra.

Figure 7-17 shows both the experimental spectrum of the bare AmBe source and its computational prediction. The difference between the experimental results and computational model can be seen in peak resolution. The resolution of the experimental detector resulted in smeared peaks from 2.2 and 4.4 MeV gamma rays. However, the 2.2 MeV peak is very pronounced, even in the experimental spectrum. As was mentioned before, the simulation predicts considerably better resolution than observed in the experimental data.

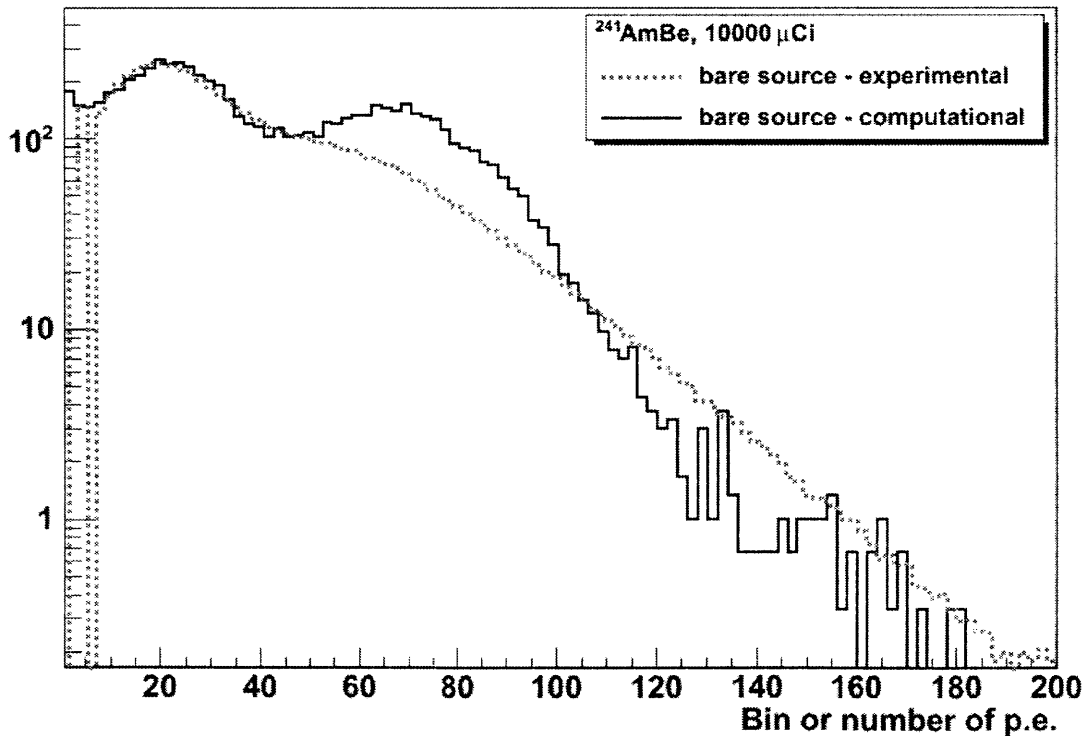


Figure 7-17. Comparison of bare AmBe source spectra obtained using Geant4 model and experimental setup.

The experimental spectra appear to be more smeared when compared to the computational results. This is largely because the experimental spectra are obtained by subtracting the background from the data, which contributes to the spectrum smearing. It is possible to make the experimental spectrum more resolved by using tagging techniques. Additionally, the computationally predicted spectrum can be “smeared” or smoothed by using a smoothing convolution.

Smoothing is often used in imaging techniques and computer vision to reduce the presence of noise. One of the more popular choices for the smoothing function is Gaussian⁶⁹ because of its symmetry, smoothness, and ability to use standard deviation of a filter window as a measure of its size. In particular, Gaussian works very well for two-dimensional graphs (images) because it is a completely circularly symmetric operator that can be decomposed into x and y components effectively reducing a complicated 2-D convolution to a combination of 1-D Gaussian convolutions.

The results of experiment and simulation are organized in histograms of equisized bins. The advantage of using histograms for data representation is in simplicity of representation and analysis. The histograms were converted into frequency polygons to take advantage of smooth density function. The resulted frequency polygons were smeared by a Gaussian smoothing function, in which each point was replaced by a weighted average of its neighbors. The following convolution was used to represent the smoothing function:

$$f(x) = \sum_{i=1}^N p(x_i)K(x - x_i) \quad \text{Eq. 7-2}$$

where p is the frequency polygon vector, N is the number of elements in the vector, and K is a **normalized** Gaussian kernel function used to compute the coefficients for Gaussian window expressed as:

$$K(u) = \begin{cases} e^{-\frac{1}{2}\left(\alpha\frac{u}{n/2}\right)^2}, & \text{if } -\frac{n}{2} < u < \frac{n}{2} \\ 0, & \text{otherwise} \end{cases} \quad \text{Eq. 7-3}$$

where n is number of points in Gaussian window and α is a inverse proportionality constant of Gaussian window n which was kept at the constant value of 2.5^h. Thus, by varying n , we effectively vary Gaussian standard deviation $\sigma = n/\alpha$.

Figure 7-18 illustrates effects of smoothing on the shape of simulation results. Two sizes of Gaussian filter (window) are shown: $n=10$ and $n=20$. Note that the 20-point Gaussian window results in more smeared spectrum than 10-point window. Making the smoothing parameter larger than 20 results in over-smoothing of the spectrum with two peaks combined into a single one. As the smoothing kernel is applied to the simulation results, the well-defined valley between the two peaks disappears, and the shape of the spectrum tends to look more like the experimental.

One interesting feature revealed after spectrum smoothing was that both the peak attributed to 2.2 MeV emitted after neutron absorption on hydrogen and the 4.4 MeV peak decreased in order to fill the valley. The relative height of peaks in experimental and simulation spectra do not match. Such discrepancy could be due to background subtraction effects. Recall from Figure 7-16, Channel 200, that the 2.2 MeV peak is a result of subtraction of two large numbers. Better agreement between the simulation and experiment would be expected if the background rejection techniques discussed in Section 7.3 were implemented.

^h MATLAB default value.

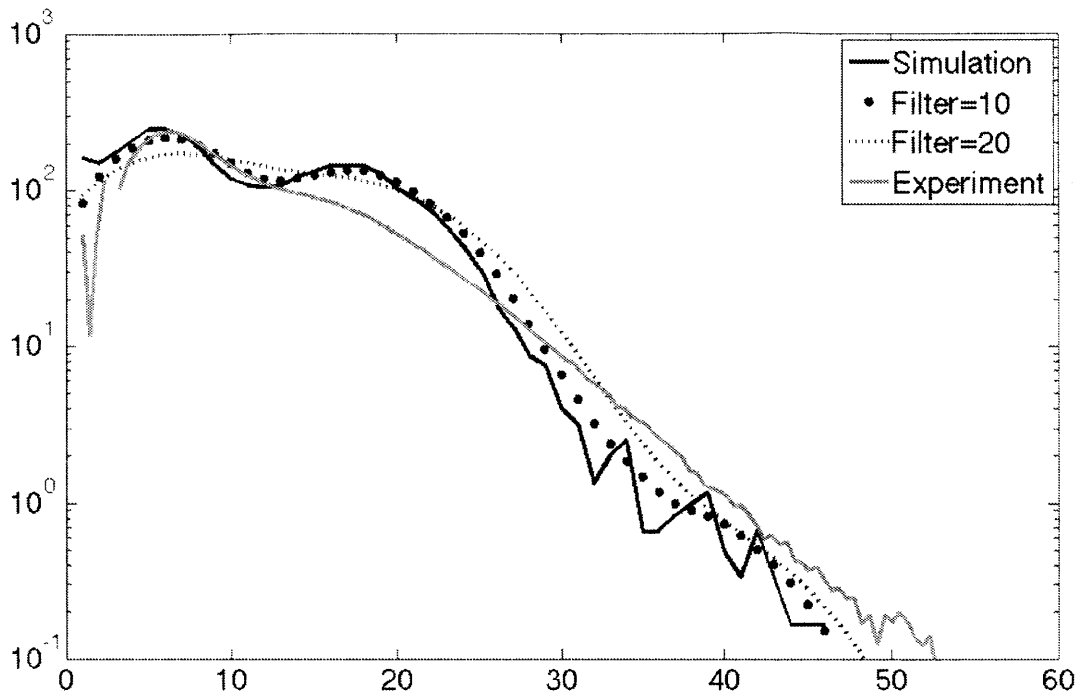


Figure 7-18. Comparison of experiment and simulation after smoothing function was applied. The units of x-axis are arbitrary to show the comparison.

7.5. Summary of event reconstruction methodology

The event reconstruction was approached by coupling pre-experimental simulations in Geant4 and post-experimental data processing using ROOT. The computational model was successfully used to qualitatively predict possible detector behavior in various experimental environments, and experimental data provided verification of the predicted scenario. The quantitative agreement between the experiment and the simulation was not found satisfactory, and implementation of background rejection techniques is recommended. Refinement of detection methods along with

improvements in the computational model upon obtaining experimental results with minimum background contribution would allow for more quantitative predictions of detector behavior. For more complex events, iteration between the experiment and simulation will help to reconstruct the actual event.

8. Conclusions and future work

Long-range active nuclear interrogation techniques require special detectors. The focus of this research was on the development of non-traditional nuclear security detector based on existing expertise with the Cherenkov high-energy particle detectors. We showed that the Cherenkov-type counter has a potential to fulfill the requirements of such novel detection systems for active interrogation applications. Cherenkov detectors have the ability to work in intense low-energy background, for example near a linear accelerator. Cherenkov detectors have **inherent low energy sensitivity cutoff** due to the threshold nature of Cherenkov light. In many active interrogation systems using electron accelerators, the bulk of the background from scattering is often below the threshold of the Cherenkov detector. In addition, such detectors can use **almost any medium as a detector body**, as long as light transparency is ensured and, if water-based such detectors are inexpensive to manufacture, and a variety of shapes can be configured.

The main objective of this thesis was to design a large-size (meter scale) water-based Cherenkov detector capable of detecting gamma rays and to demonstrate that the detector is capable of particle energy discrimination. The detector was shown to successfully detect gamma rays of energies above the Cherenkov threshold.

This Chapter reviews the research objectives, summarizes the work performed to attain these objectives, and provides recommendations for future work.

8.1. Research objectives

The purpose of this thesis was to investigate the principles of design and applicability of the use of water-based Cherenkov detectors for gamma detection and their use in an active interrogation system. The work focused on gamma interrogation of SNM and photon-induced fission. The following objectives were fulfilled in this research:

- create and optimize a computer model of the detector;
- design, manufacture and assemble an experimental detector;
- determine whether water Cherenkov detectors are suitable for gamma detection;
- demonstrate the ability of the detector to discriminate between gamma rays of various energies.

A study of the detector performance using both computational and experimental methods has been conducted.

8.2. Summary of work performed

8.2.1. Computational model

The computational model described in Chapter 4 was developed for the detector optimization studies and prediction of the detector performance with various radiation sources. The model is capable of triggering and tracking optical processes, which include the generation of photons by scintillation process, Cherenkov photon production by a charged particle, and transition radiation. The model incorporates the geometry of the detector including the reflector, water absorption coefficients, optical boundaries, and

quantum efficiencies of PMTs. All of the materials, including the aluminum shell, polypropylene insert, and PMT windows, were modeled in detail featuring their molecular compositions.

For neutron detection, ^{10}B lined tubes were incorporated into the overall design. Detector design studies of the model were conducted mostly on the basis of placement of ^{10}B tubes either within the Cherenkov volume or outside the water. The model predicted no statistically significant difference between performances of the two designs. The experimentally built detector follows simpler design with ^{10}B tubes outside the detection volume.

The model also successfully predicted the detector behavior near various isotope sources. Final verification was done using an $^{241}\text{AmBe}$ source. The double-peak feature of the AmBe source was reproduced experimentally including the scenarios with neutron peak enhancements.

8.2.2. Experimental detector

The experimental detector was designed based on the optimization studies performed with the computational model. The detector is composed of a light-tight 1/8-inch-thick aluminum body, a polypropylene insert for support of high efficiency (98.5%) diffuse reflector (Gore RFP), six 8" PMTs supported by an aluminum plate, and DI-grade filtered water.

One of the main problems with Cherenkov radiation is the limited intensity of the emitted light. We used a material with high diffuse reflectivity to cover the inside walls of the detector in order to preserve as much light as possible. In addition, we designed a water-purifying loop to produce water of high-purity to avoid photon absorption by impurities.

The detector was able to detect a signal from ^{137}Cs , although the statistics of the signal was very poor. This was expected because the energy of the gamma rays emitted by ^{137}Cs (661 keV) is barely above the Cherenkov threshold. The efficiency of the detector for ^{60}Co (1.17, 1.33 MeV) radiation measurement was calculated to be about 30%. One of the significant limitations of the Cherenkov detector was found to be energy resolution. The resolution of such detectors is quite poor. However, the radiation expected from photofission does not have readily identifiable peaks in the 3 to 10 MeV range and thus, consideration of resolution was not a major contributor to the detector design.

Event reconstruction was an important part of the detector performance analysis. The event reconstruction methods were developed by coupling pre-experimental simulations in Geant4 and post-experimental data processing using ROOT. The computational model was used to predict possible detector behavior in various radiation environments, and experimental data provided verification of the predicted scenario.

8.3. Future work

One of the main limitations of the computational model was an approximation used to model light absorption length in water. Because of the complexity of experimental measurements, the actual absorption length was unknown, and an estimate was used. However, as was shown in Chapter 4, the light absorption length can significantly impact the performance of the detector. Therefore, it is recommended that the light absorption coefficients of water estimated as close to the actual as possible.

Models of multiple sources have been incorporated into the detector model. A very limited model of background, which included 2.6 MeV gamma rays due to ^{208}Tl emitted at random angles relative to the detector, was also incorporated. The model can

be improved by including more details of low-energy terrestrial radiation as well as cosmic rays.

The detector design and analysis was done to demonstrate that it is possible to use water-based Cherenkov counters to detect and characterize gamma rays. Several light collection enhancements were employed in the final design, however, there are more ways to improve the detector performance and potentially resolution. One of the possible improvements would be using the directionality property of Cherenkov light. This could potentially improve signal-to-noise ratio of the detector. In an active interrogation application, a target location is directionally predicted, and gamma ray energy of interest is between 3 and 10 MeV. In this range, forward Compton scattering is dominant allowing for directionality exploration. As an alternative to directional methods of background rejection, wavelength-shifting (WLS) dopants can be used. Cherenkov light emission is maximized in the ultraviolet region, which is outside of visible range of most PMTs. Because of the absence of self-absorption of the light in the detector medium, WLS chemicals can enhance light in the PMT-sensitive region. Even though using WLS might be faster path to background rejection, all of directional properties of Cherenkov light would be lost. It must be noted here that there is a difference between development of a total absorption counter (for example, for photon spectroscopy) and a directional counter (for enhanced background rejection) because multiple electron scattering will deteriorate directionality properties.

Current analysis was based on collecting energy information in the detector and using it to reconstruct an event. Another characteristic of the signal – timing information relative to the interrogating beam pulse – was not used in the current analysis. Time and energy information about the radiation arriving at the detector after the target irradiation can provide additional method for background rejection. Fission, whether induced by gamma or neutron, results in emission of prompt (within 10^{-15} seconds) and delayed radiation. Prompt neutrons are emitted in higher numbers and with higher energies than delayed neutrons. On the other hand, a unique signature of SNM is emission of delayed

gammas and neutrons after fission. Such delayed gammas are product of beta decay of many short-lived fission products and generally have high energies making them distinguishable from background. Delayed neutrons are generated in low numbers, but their quantity is proportional to the amount of actinides in the target. Measuring both prompt and delayed radiation as well as neutrons and gammas could potentially allow for a spectroscopic long-range active interrogation detector.

Consider the following time scale of a fission process. A photon beam is fired in the direction of a target. It takes about 10^{-15} seconds for a fission or photofission process to take place. The nucleus is split into two fragments. Two or three prompt neutrons are emitted 10^{-20} seconds later, and eight gammas are emitted 10^{-17} seconds after the split. Temporal behavior of delayed neutrons (generally referred to as six groups based on their decay constant) depends on a nuclide that underwent fission. Six to eight delayed gammas are emitted seconds and minutes after the nucleus split with total energy of 6-8 MeV. Unique gamma ray signatures exist for each nuclide of special nuclear material. This simplified example illustrates how the problem of acquiring time and energy information in Cherenkov detectors can be approached using the time structure of the signals.

8.4.Data acquisition system

The results reported in this thesis have been obtained using a QDC (gated integrator) data acquisition system. As a part of this thesis work, the data acquisition system was reconfigured from the QDC analog approach to a fast, waveform digitizing ADC. In this system, the analog waveform is digitized at 4 ns intervals and an internal FPGA is used to calculate the total charge. More testing of the ADC system is necessary

including testing of effects of various integrating window widths, threshold parameters, and multiplicity.

Using the fast ADC as a data acquisition system is recommended because of the simplified DAQ as well as improvement of data collection, however it must be noted here that the firmware for ADC systems are generally more complex than for QDC.

9. Bibliography

1. American Physical Society, "Nuclear power and proliferation resistance: security benefits, limiting risk," Report of the Nuclear Energy Study Group of the American Physical Society Panel on Public Affairs, Washington, May 2005.
2. U.S. Department of Defense, "Nuclear Posture Review Report," April 2010.
3. R. Mowatt-Larssen, "Nightmares of nuclear terrorism," *Bulletin of the Atomic Scientists*, vol. 66, pp. 37-45, 2010.
4. R. Scott Kemp and Alexander Glaser, "Statement on Iran's ability to make a nuclear weapon and the significance of the 19 February 2009 IAEA report on Iran's uranium-enrichment program," March 2 2009.
5. U.S. Congress, Office of Technology Assessment, "Nuclear Safeguards and the International Atomic Energy Agency," OTA-ISS-615 (Washington, DC: U.S. Government Printing Office), p11, June 1995.
6. A. Glaser and Z. Mian, "Fissile Material Stockpiles and Production," *Science & Global Security*, vol. 16, pp. 55-73, 2008.
7. M.V. Hynes, "Denying Armageddon: preventing terrorist use of nuclear weapons," *The ANNALS of the American Academy of Political and Social Science*, vol. 607, pp. 150-161, 2006.
8. C.W. Forsberg et al., "Definition of weapons-usable uranium-233," ORNL/TM-13517, March 1998.
9. W.G. Schubert, "On The Security Of Our Seaports," statement, February 26, 2002, before the Committee on the Judiciary Subcommittee on Technology, Terrorism, and Government Information United States Senate. Available at: <http://www.gpo.gov/fdsys/pkg/CHRG-107shrg85082/html/CHRG-107shrg85082.htm>; Accessed: 11/09/09.
10. Megaport Initiative. Available at:

<http://nnsa.energy.gov/aboutus/ourprograms/nonproliferation/programoffices/internationalmaterialprotectionandcooperation/-5>; Accessed: 11/13/09.

11. R.C. Byrd et al., "Nuclear detection to prevent or defeat clandestine nuclear attack," *IEEE Sensors J.*, vol. 5, pp. 593-609, 2005.
12. K.P. Ziock et al., "Large area imaging detector for long-range, passive detection of fissile material," *IEEE Trans. Nucl. Sci.*, vol. 51, pp. 2238-2244, 2004.
13. D. Dietrich et al., "A kinematically beamed, low energy pulsed neutron source for active interrogation," *Nucl. Instrum. Meth. B*, vol. 241, pp. 826-830, 2005.
14. J. Jones et al., "High-energy photon interrogation for nonproliferation applications," *Nucl. Instrum. Meth. B*, vol. 261, pp. 326-330, 2007.
15. J. Jones et al., "Detection of shielded nuclear material in a cargo container," *Nucl. Instrum. Meth. A*, vol. 562, pp. 1085-1088, 2006.
16. J.O. Malley et al., "Advanced active interrogation sources for remote detection of special nuclear material," *IEEE Conf. Technologies for Homeland Security (HST'09)*, Boston, MA, 11-12 May 2009, pp. 287-294.
17. D. Slaughter et al., "Detection of special nuclear material in cargo containers using neutron interrogation," UCRL-ID-155315, Aug. 2003.
18. C.E. Moss et al., "Neutron detectors for active interrogation of highly enriched uranium," *IEEE Trans. Nucl. Sci.*, vol. 51, pp. 1677-1681, 2004.
19. L. Claude and P.-G. Rancoita, *Radiation Interaction In Matter And Detection*. Singapore: World Scientific Publishing, 2009, pp. 419-435.
20. S. Dazeley et al., "Observation of neutrons with a gadolinium doped water Cherenkov detector," *Nucl. Instrum. Meth. A*, vol. 607, pp. 616-619, 2009.
21. J. Medalia, "Detection of Nuclear Weapons and Materials: Science, Technologies, Observations," CRS Report for Congress, Congressional Research Service R40154, 2009.
22. T. Gozani, "Active Nondestructive Assay of Nuclear Materials," Technical Report NUREG/CR-0602, U.S. Nuclear regulatory Commission, Washington, D.C., 1981.

23. IAEA Nuclear Data Services, Photonuclear cross sections with mono-energetic neutron-capture gamma rays. Available at: <http://www-nds.iaea.org>; Accessed: 03/01/11.
24. H.W. Koch, J. McElhinney and E.L. Gasteiger, "Experimental photo-fission thresholds in ${}_{92}\text{U}^{235}$, ${}_{92}\text{U}^{238}$, ${}_{92}\text{U}^{233}$, ${}_{94}\text{Pu}^{239}$, and ${}_{90}\text{Th}^{232}$," *Phys. Rev.*, vol. 77, pp. 329-336, 1950.
25. B.L. Berman et al., "Photofission and photoneutron cross sections and photofission neutron multiplicities for ${}^{233}\text{U}$, ${}^{234}\text{U}$, ${}^{237}\text{Np}$, and ${}^{239}\text{Pu}$," *Phys. Rev. C*, vol. 34, pp. 2201-2214, 1986.
26. R. Walton et al., "Delayed gamma rays from photofission of U^{238} , U^{235} , and Th^{232} ," *Phys. Rev.*, vol. 134, B824, 1964.
27. J.J. Griffin, "Beta decays and delayed gammas from fission fragments," *Phys Rev*, 134, B817, 1964.
28. D.H. Beddingfield and F.E. Cecil, "Identification of fissile materials from fission product gamma-ray spectra," *Nucl. Instrum. Meth. A*, vol. 417, pp. 405-412, 1998.
29. E. Swanberg et al., "Using low resolution gamma detectors to detect and differentiate ${}^{239}\text{Pu}$ and ${}^{235}\text{U}$ fissions," *J. Radioanal. Nucl. Ch.*, vol. 282, pp. 901-904, 2009.
30. R. Marrs et al., "Fission-product gamma-ray line pairs sensitive to fissile material and neutron energy," *Nucl. Instrum. Meth. A*, vol. 592, pp. 463-471, 2008.
31. R. Kouzes et al., " ${}^3\text{He}$ Alternatives for National Security," AAAS Workshop on Helium-3, FRM II, July 7-8, 2009.
32. H. Watanabea et al., "First study of neutron tagging with a water Cherenkov detector," *Astropart. Phys.*, vol. 31, pp. 320-328, 2009.
33. N. Bowden et al., "Experimental results from an antineutrino detector for cooperative monitoring of nuclear reactors," *Nucl. Instrum. Meth. A*, vol. 572, pp. 985-998, 2007.
34. W. Coleman et al., "Transparency of 0.2% GdCl_3 doped water in a stainless steel test environment," *Nucl. Instrum. Meth. A*, vol. 595, pp. 339-345, 2008.

35. A. Kibayashi, "Gadolinium study for a water Cherenkov detector," *Proc. DPF-2009 Conf.*, Detroit, MI, pp. 1-4, Sep. 2009.
36. P.A. Cherenkov, "Vidimoe svechenie chistykh zhidkosti pod deistviem γ -radiatsii," *Dokl. Akad. Nauk SSSR*, vol. 2, p. 451, 1934.
37. P. Čerenkov, "Visible radiation produced by electrons moving in a medium with velocities exceeding that of light," *Phys. Rev.*, vol. 52, pp. 378-379, 1937.
38. I.M. Frank and I.G. Tamm, "Coherent visible radiation of fast electrons passing through matter," *Dokl. Akad. Nauk SSSR*, vol. 14, p. 109, 1937.
39. I.M. Frank, "A conceptual history of the Vavilov-Cherenkov radiation," *Sov. Phys. Usp.*, vol. 27, pp. 385-395, 1984.
40. B.D. Sowerby, "Čerenkov detectors for low-energy gamma rays," *Nucl. Instrum. Meth.*, vol. 97, 145-149, 1971.
41. G. Knoll, *Radiation Detection and Measurement*. 3rd Ed., John Wiley and Sons, Inc. 2000, p. 52.
42. S. Agostinelli, "Geant4—a simulation toolkit," *Nucl. Instrum. Meth. A*, vol. 506, pp. 250-303, 2003.
43. J. Allison et al., "Geant4 developments and applications," *IEEE Trans. Nucl. Sci.*, vol. 53, pp. 270-278, 2006.
44. Geant4: a toolkit for the simulation of the passage of particles through matter. Available at:

<http://www.geant4.org/geant4/>; Accessed: 01/05/11.
45. Schubert, E.F. Light Emitting Diodes. Available at:

<http://www.ecse.rpi.edu/~schubert/Light-Emitting-Diodes-dot-org/>; Accessed: 02/02/11.
46. GORE® Diffuse Reflector Product. Available at:

http://www.gore.com/en_xx/products/electronic/specialty/specialty.html;
Accessed: 10/03/10.

47. G.M. Hale and M.R. Querry, "Optical Constants of Water in the 200-nm to 200-microm Wavelength Region," *Appl. Optics*, vol. 12, pp. 555-563, 1973.
48. M.R. Querry, P.G. Cary and R.C. Waring, "Split-pulse laser method for measuring attenuation coefficients of transparent liquids: application to deionized filtered water in the visible region," *Appl. Optics*, vol. 17, pp. 3587-3592, 1978.
49. R.C. Smith and K.S. Baker, "Optical properties of the clearest natural waters (200-800 nm)," *Appl. Optics*, vol. 20, pp. 177-184, 1981.
50. B. Blackburn, personal communication.
51. C. Grupen and B. Shwartz, *Particle Detectors*. Cambridge, MA: Cambridge University Press, 2008, pp. 390-433.
52. C. Tintori, "Digital Pulse Processing in Nuclear Physics," *CAEN Reports*, p. 4, 2011.
53. CAEN Electronic Instrumentation V1495 General Purpose VME Board. Available at:

<http://www.caen.it/jsp/Template2/CaenProd.jsp?tab=4&parent=11&idmod=484>;
Accessed: 04/12/11
54. CAEN Electronic Instrumentation V1720 8 Channel 12bit 250 MS/s Digitizer. Available at:

<http://www.caen.it/csite/CaenProd.jsp?idmod=570&parent=11>;

Accessed: 04/12/11
55. Hamamatsu Photonics. Available at:

<http://www.hamamatsu.com>; Accessed: 04/12/11
56. J. Martin, *Physics for radiation protection: a handbook*. Wiley VCH, 2006, pp. 255-305.
57. Table of Nuclides. Available at:

atom.kaeri.re.kr; Accessed: 04/22/11

56. G. Heusser, Low-Radioactivity Background Techniques. *Ann. Rev. Nucl. Part. S.* vol. 45, pp. 543-590, 1995.
57. J. Martin, *Physics for radiation protection: a handbook*. Wiley VCH, 2006, pp. 255-305.
58. Table of Nuclides. Available at:

atom.kaeri.re.kr; Accessed: 04/22/11
59. P. Jagam and J. Simpson, "Measurements of Th, U and K concentrations in a variety of materials," *Nucl. Instrum. Meth. A*, vol. 324, pp. 389-398, 1993.
60. J. Shapiro, *Radiation Protection: A Guide for Scientists and Physicians*. Harvard, MA: Harvard University Press, 1990, p. 355.
61. A. Haungs and H. Rebel, "Energy spectrum and mass composition of high-energy cosmic rays," *Rep. Prog. Phys.*, vol. 66, pp. 1145-1206, 2003.
62. J.K. Shultis and R.E. Faw, *Fundamentals of Nuclear Science and Engineering*. CRC Press, 2002, p. 111.
63. D. Leonard, "Systematic study of trace radioactive impurities in candidate construction materials for EXO-200," *Nucl. Instrum. Meth. A*, vol. 591, pp. 490-509, 2008.
64. G. Venkataraman et al., "The gamma to neutron ratios for Pu-Be and Am-Be neutron sources," *Nucl. Instrum. Meth.*, vol. 82, pp. 49-50, 1970.
65. Z. Liu et al., "The 4.438 MeV gamma to neutron ratio for the Am-Be neutron source," *Appl. Radiat. Isotopes*, vol. 65, pp. 1318-1321, 2007.
66. B. Kamboj and M. Shahani, "Precise measurement of the gamma to neutron ratio of an Am- α -Be neutron source using an improved manganese bath technique," *Nucl. Instrum. Meth. A*, vol. 244, pp. 513-515, 1986.
67. J. Marxh et al., "High resolution measurements of neutron energy spectra from Am-Be and Am-B neutron sources," *Nucl. Instrum. Meth. A*, vol. 366, pp. 340-348, 1995.
68. X-Ray Mass Attenuation Coefficients. Available at:

<http://physics.nist.gov/PhysRefData/XrayMassCoef/tab4.html>; Accessed: 01/21/11

69. R. Haddad and A. Akansu, "A class of fast Gaussian binomial filters for speech and image processing," *IEEE T. Signal Proces.*, vol. 39, pp. 723-727, 1991.
70. F. Becvar, "Simulation of γ cascades in complex nuclei with emphasis on assessment of uncertainties of cascade-related quantities," *Nucl. Instrum. Meth. A*, vol. 417, pp. 434-449, 1998.

Appendix A. Ideal case based on Tamm-Frank derivation

The goal is to derive expression for Cherenkov radiation in terms of total energy radiated per unit path length by a charged particle. These derivations are based on Frank-Tamm theory, and the references were provided in Chapter 3.

The assumptions for these derivations are outlines below:

- Particle with charge e^- moving in a straight line with a constant velocity v
- Infinite, isotropic and transparent dielectric
- Properties of the medium are described by dielectric constant only ($\epsilon \neq 1$) or equivalently by refractive coefficient $n(\omega) = \sqrt{\epsilon(\omega)}$
- Magnetic permeability μ is taken as 1

A.1. Dispersive medium, dielectric constant and magnetic permeability

One of the main assumptions of this derivation is that the magnetic permeability is a constant, while the dielectric constant is a function of photon frequency. If the medium is not dispersive, both the dielectric constant and magnetic permeability of such medium are constant and relate electric and magnetic induction to the electric and

magnetic fields, respectively. The assumption that the magnetic permeability is a constant is valid in the current derivation because water is a non-magnetic medium. However, the dielectric constant in water, which is a dispersive medium, is a function of electromagnetic wave frequency.

A.2. Maxwell's equations

The electromagnetic field generated by such a particle can be described using Maxwell's equations A-1:

$$\left\{ \begin{array}{l} \vec{\nabla} \cdot \vec{E} = \frac{4\pi}{\epsilon} \rho \\ \vec{\nabla} \times \vec{E} + \frac{1}{c} \frac{\partial \vec{H}}{\partial t} = 0 \\ \vec{\nabla} \cdot \vec{H} = 0 \\ \vec{\nabla} \times \vec{H} = \frac{4\pi}{c} \vec{j} + \frac{1}{c} \frac{\partial \vec{D}}{\partial t} \end{array} \right. \quad \text{Eq. A-1}$$

The first equation, known as Gauss' law for \vec{E} , describes electric flux through a surface which is proportional to the enclosed charge. The second equation is known as Faraday's law describing how changing magnetic flux produces electric field. The third equation is Gauss's law for magnetism, \vec{H} , stating that magnetic monopoles do not exist. The last equation is Ampere-Maxwell law describing magnetic field produced by electric current and changing electric field. ρ and \vec{j} are the free charge and the current densities created by the passing charged particle.

We can simplify Equation A-1 by rewriting it in terms of vector potential. The magnetic vector potential \vec{A} is a three-dimensional polar vector whose curl is the magnetic field. To describe electric field, both magnetic potential and scalar potential are required. Equation A-2 describes magnetic (top 2) and electric (bottom) fields in terms of potential. The definition of \vec{E} and \vec{H} satisfies the two homogeneous Maxwell's equations.

$$\begin{cases} \vec{H} = \frac{1}{\mu} \vec{\nabla} \times \vec{A} \\ \vec{E} = -\nabla\phi - \frac{1}{c} \frac{\partial \vec{A}}{\partial t} \end{cases} \quad \text{Eq. A-2}$$

The dynamic behavior of \vec{A} and ϕ is determined by inhomogeneous Maxwell's equations. We can rewrite inhomogeneous Maxwell's equations in terms of potentials as:

$$\begin{cases} \nabla^2 \vec{A} - \frac{\epsilon\mu}{c^2} \frac{\partial^2 \vec{A}}{\partial t^2} - \nabla \left(\vec{\nabla} \cdot \vec{A} + \frac{\epsilon\mu}{c} \frac{\partial \phi}{\partial t} \right) = -\frac{4\pi\mu}{c} \vec{j} \\ \nabla^2 \phi + \frac{1}{c} \frac{\partial}{\partial t} (\vec{\nabla} \cdot \vec{A}) = -\frac{4\pi}{\epsilon} \rho \end{cases} \quad \text{Eq. A-3}$$

Additionally, to ensure that the above magnetic vector potential is uniquely defined (recall that additional curl-free components can be added to the magnetic potential without changing the observed magnetic field), we set the vector potential to satisfy Lorenz gauge condition written as Equation A-4:

$$\vec{\nabla} \cdot \vec{A} + \frac{\epsilon\mu}{c} \frac{\partial \phi}{\partial t} = 0 \quad \text{Eq. A-4}$$

Using the Lorenz gauge condition, we can uncouple inhomogeneous Maxwell's equations leaving two independent wave equations, with sources:

$$\begin{cases} \nabla^2 \vec{A} - \frac{\epsilon\mu}{c^2} \frac{\partial^2 \vec{A}}{\partial t^2} = -\frac{4\pi\mu}{c} \vec{j} \\ \nabla^2 \varphi - \frac{\epsilon\mu}{c^2} \frac{\partial^2 \varphi}{\partial t^2} = -\frac{4\pi}{\epsilon} \rho \end{cases} \quad \text{Eq. A-5}$$

Equations A-5 combined with Lorentz gauge condition form complete set of equations equivalent to Maxwell's equations. The equations A-5 are considered to be the starting point of almost any derivation related to Cherenkov phenomenon and, more generally, problems treating a charge moving through a medium.

A.3. Moving point charge and its fields

The simple case of current density and free charge moving along the z-axis can be describes as:

$$\begin{cases} j_x = j_y = 0 \\ j_z = ev\delta(x)\delta(y)\delta(z - vt) \\ \rho = e\delta(x)\delta(y)\delta(z - vt) \end{cases} \quad \text{Eq. A-8}$$

The moving charge uniformly moving in an infinite and isotropic medium emits electromagnetic field, which is stationary in the reference frame of the point charge. The

system of equations A-5 must satisfy the plane electromagnetic wave equation emitted by the charge, where \vec{k} is the wave vector:

$$\zeta = e^{i\vec{k}(\hat{z}-\vec{v}t)} \quad \text{Eq. A-9}$$

The surfaces of the emitted electromagnetic waves are perpendicular to \vec{k} . The electromagnetic waves propagate through the medium with velocity \vec{v} .

Since the system of equations A-5 is homogeneous everywhere in time-space except at $\vec{z} = \vec{v}t$ (see Eq. A-8), we can rewrite A-5 as:

$$\begin{cases} \frac{1}{\mu} \left(\nabla^2 \vec{A} - \frac{\varepsilon\mu}{c^2} \frac{\partial^2 \vec{A}}{\partial t^2} \right) = 0 \\ \varepsilon \left(\nabla^2 \varphi - \frac{\varepsilon\mu}{c^2} \frac{\partial^2 \varphi}{\partial t^2} \right) = 0 \end{cases} \quad \text{Eq. A-10}$$

Substituting the wave equation A-9 into the system, we get a system of equations A-11. Note that the dielectric constant and the magnetic permeability are functions of frequency $\omega = \vec{k}\vec{v}$.

$$\begin{cases} \frac{1}{\mu(\vec{k}\vec{v})} \left(k^2 - \mu(\vec{k}\vec{v})\varepsilon(\vec{k}\vec{v}) \frac{(\vec{k}\vec{v})^2}{c^2} \right) = 0 \\ \varepsilon(\vec{k}\vec{v}) \left(k^2 - \mu(\vec{k}\vec{v})\varepsilon(\vec{k}\vec{v}) \frac{(\vec{k}\vec{v})^2}{c^2} \right) = 0 \end{cases} \quad \text{Eq. A-11}$$

From equations A-11, we can deduce that the following relations are possible:

$$\mu \neq 0 \quad \text{Eq. A-12a}$$

$$k^2 = \mu\varepsilon(\omega) \frac{(\omega)^2}{c^2} \quad \text{Eq. A-12b}$$

$$\varepsilon(\omega) = 0 \quad \text{Eq. A-12c}$$

Electromagnetic waves that satisfy the condition A-12b are called Cherenkov waves. Recognizing that the dot product can be written as $\vec{k}\vec{v} = kv\cos\theta$, we can rewrite Eq. A-12b as:

$$k^2 = \mu\varepsilon(\omega) \frac{(kv\cos\theta)^2}{c^2} \implies (\cos\theta)^2 = \frac{c^2}{\mu\varepsilon(\omega)v^2} \quad \text{Eq. A-13}$$

Recall from the discussion in Section A.1 that the magnetic permeability is constant and $n(\omega) = \sqrt{\varepsilon(\omega)}$. Rewriting Eq. A-13 in terms of refractive coefficient of the medium:

$$\cos\theta = \frac{1}{n(\omega)\beta} \quad \text{Eq. A-14}$$

Where β is the ratio of particle velocity v to the speed of light in vacuum c .

Appendix B. Neutron detection using Cherenkov counters

Since neutron particles are also uncharged, Cherenkov light must be produced by indirect interaction with charged particles. A neutron interaction with an electron is impossible. However, a neutron capture on a nucleus with high-capture cross section and subsequent decay by gamma emission can be used to detect neutron presence. The process of neutron detection is complicated by a necessary neutron capture and emission of a single gamma ray or a cascade of gamma rays and subsequent Compton interaction of such gamma rays with electrons. In neutron detection, the directionality is completely lost because of neutron capture and isotropic gamma release.

One of the most recent developments of neutron detection was addition of high-capture cross section dopings into the detector medium, for example Gd salts. GdCl_3 is used because of large neutron capture cross section of the Gd isotopes (49,000 barns for natural Gd). When a neutron is captured on Gd nucleus, a gamma cascade with total energy 7.9 MeV for ^{157}Gd and 8.5 MeV for ^{155}Gd is released. Neutron detection is achieved through Cherenkov light generated by Compton scatter by such gamma-ray cascades following neutron capture on Gd.

B.1 Gd modeling in Geant4: comparing Geant4, Dicebox and ENDF libraries

When a neutron is captured on Gadolinium nucleus, a gamma cascade with total energy 7.9 MeV for ^{157}Gd and 8.5 MeV for ^{155}Gd is released. Because the neutron capture is characterized by such gamma cascades, accurate modeling of Gd de-excitation gamma cascades is essential in simulation of Gd-loaded neutron detector. Currently, Geant4.9.3 does not properly reproduce Gd excited nucleus decay. Moreover, occasionally Geant4 violates the conservation of energy of the excited nucleus decay. DICEBOX, a Monte Carlo based code, generates γ -ray cascades initiating at the neutron capturing state and terminating at the ground state following the rules of the extreme statistical model.

Figure B-1 compares the gamma cascades generated in Geant4 and DICEBOX. Note that obvious discrepancies between the two codes in the discrete gamma region, especially for 7.9 MeV gamma release. The figure also contains an extra 2.2 MeV line due to capture on hydrogen but this line is an artifact of the simulation.

Cascade energies generated by DICEBOX were introduced into GEANT4 model to compare computational results with experimental. In order to model the gamma cascade following a neutron capture on Gd, the following methodology was applied. First, a flux of neutrons incident on the detector was simulated. The locations and times of neutron absorption were recorded and stored. The Geant4 run was terminated. Second, the absorption location and time data set was supplied with gamma and electron cascade details obtained from DICEBOX. The Geant4 run was restarted with newly "defined" particles - gammas and electrons from a cascade. The simulation continued normally from this point on. Such approach allowed us to use more reliable DICEBOX data to simulate neutron absorption on Gd and subsequent gamma cascade release.

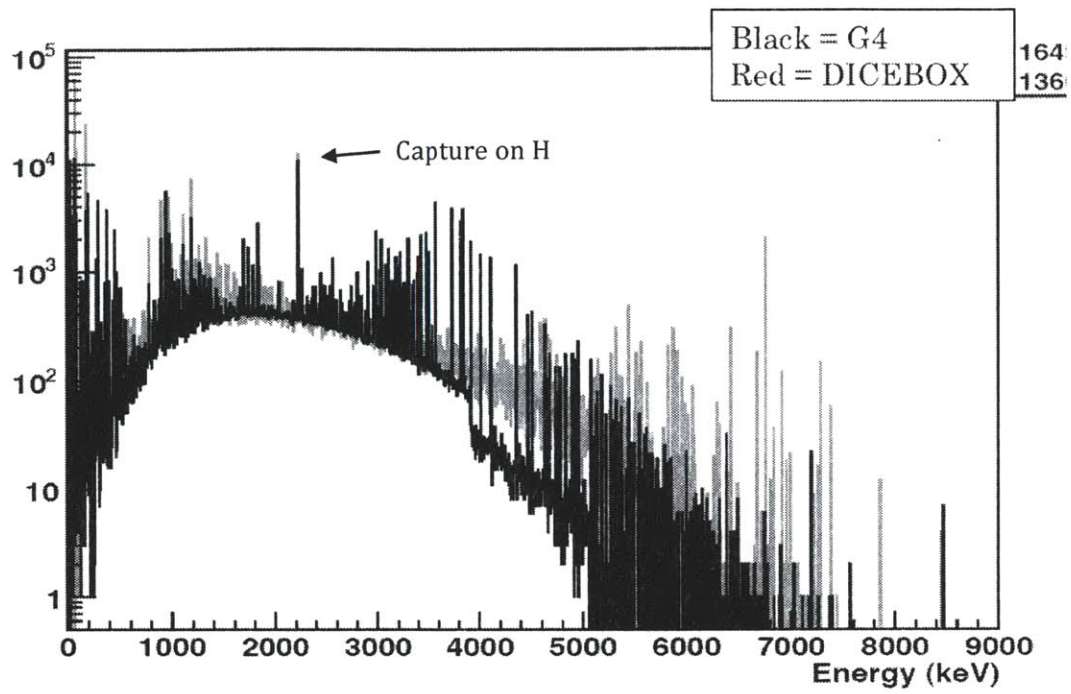


Figure B-1. Comparison of Geant4 and DICEBOX gamma cascade generation following neutron captures on Gd.

Appendix C. Examples of Geant4 and ROOT

C.1. Detector geometry and construction

This portion of the code provides the arrays used in the model to simulate Cherenkov photon energies, quantum efficiency of the PMTs, refractive coefficient of the water, and light absorption length in the water. The last three vectors are functions of the declared photon energies.

```
OTNSimDetectorConstruction::OTNSimDetectorConstruction()  
{ materials = new OTNSimMaterials();  
  
    numEnergies = 32;  
  
    PhotonEnergy[0] = 1.034*eV;  
    PhotonEnergy[1] = 2.068*eV;  
    PhotonEnergy[2] = 2.103*eV;  
    PhotonEnergy[3] = 2.139*eV;  
    PhotonEnergy[4] = 2.177*eV;  
    PhotonEnergy[5] = 2.216*eV;  
    PhotonEnergy[6] = 2.256*eV;  
    PhotonEnergy[7] = 2.298*eV;  
    PhotonEnergy[8] = 2.341*eV;  
    PhotonEnergy[9] = 2.386*eV;  
    PhotonEnergy[10] = 2.433*eV;  
    PhotonEnergy[11] = 2.481*eV;  
    PhotonEnergy[12] = 2.532*eV;  
    PhotonEnergy[13] = 2.585*eV;  
    PhotonEnergy[14] = 2.640*eV;  
    PhotonEnergy[15] = 2.697*eV;
```

```
PhotonEnergy[16] = 2.757*eV;  
PhotonEnergy[17] = 2.820*eV;  
PhotonEnergy[18] = 2.885*eV;  
PhotonEnergy[19] = 2.954*eV;  
PhotonEnergy[20] = 3.026*eV;  
PhotonEnergy[21] = 3.102*eV;  
PhotonEnergy[22] = 3.181*eV;  
PhotonEnergy[23] = 3.265*eV;  
PhotonEnergy[24] = 3.353*eV;  
PhotonEnergy[25] = 3.446*eV;  
PhotonEnergy[26] = 3.545*eV;  
PhotonEnergy[27] = 3.649*eV;  
PhotonEnergy[28] = 3.760*eV;  
PhotonEnergy[29] = 3.877*eV;  
PhotonEnergy[30] = 4.002*eV;  
PhotonEnergy[31] = 8.136*eV;
```

```
// Hamamatsu R7021-20  
PMTQEarray[0] = 0.0;  
PMTQEarray[1] = 0.033;  
PMTQEarray[2] = 0.04;  
PMTQEarray[3] = 0.05;  
PMTQEarray[4] = 0.06;  
PMTQEarray[5] = 0.08;  
PMTQEarray[6] = 0.09;  
PMTQEarray[7] = 0.11;  
PMTQEarray[8] = 0.12;  
PMTQEarray[9] = 0.14;  
PMTQEarray[10] = 0.17;  
PMTQEarray[11] = 0.18;  
PMTQEarray[12] = 0.19;  
PMTQEarray[13] = 0.20;  
PMTQEarray[14] = 0.205;  
PMTQEarray[15] = 0.21;  
PMTQEarray[16] = 0.22;  
PMTQEarray[17] = 0.225;  
PMTQEarray[18] = 0.23;  
PMTQEarray[19] = 0.235;  
PMTQEarray[20] = 0.24;  
PMTQEarray[21] = 0.24;  
PMTQEarray[22] = 0.25;  
PMTQEarray[23] = 0.25;  
PMTQEarray[24] = 0.25;  
PMTQEarray[25] = 0.24;  
PMTQEarray[26] = 0.23;  
PMTQEarray[27] = 0.21;
```

```

PMTQEarray[28] = 0.19;
PMTQEarray[29] = 0.18;
PMTQEarray[30] = 0.08;
PMTQEarray[31] = 0.0;

// Water and Doped Water Material Properties
G4double refractiveIndexWater[nEntries] = {1.3435, 1.344, 1.3445,
1.345, 1.3455, 1.346, 1.3465, 1.347, 1.3475, 1.348,
1.3485, 1.3492, 1.35, 1.3505, 1.351,
1.3518, 1.3522, 1.3530, 1.3535, 1.354,
1.3545, 1.355, 1.3555, 1.356, 1.3568,
1.3572, 1.358, 1.3585, 1.359, 1.3595,
1.36, 1.3608};

G4double absorptionWater[nEntries] =
{3.448*m, 4.082*m, 6.329*m, 9.174*m, 12.346*m,
13.889*m, 15.152*m, 17.241*m, 18.868*m, 20.000*m,
26.316*m, 35.714*m, 45.455*m, 47.619*m, 52.632*m,
52.632*m, 55.556*m, 52.632*m, 52.632*m, 47.619*m,
45.455*m, 41.667*m, 37.037*m, 33.333*m, 30.000*m,
28.500*m, 27.000*m, 24.500*m, 22.000*m, 19.500*m,
17.500*m, 14.500*m};

```

The following list represents the materials incorporated into the code. Compositions of some materials that are crucial for the detector model are also provided.

```

OTNSimMaterials::~~OTNSimMaterials()
{
delete tyvek;
delete water;
delete acrylic;
delete vacuum;
delete quartz;
delete polyethylene;
delete gadolinium;
delete blackAcrylic;
delete air;
delete mumetal;
delete ss304;
delete teflon;
delete al6061;
delete bf3;
}

```

```

    delete dopedWater;
}

void OTNSimMaterials::CreateMaterials()
{
    // Materials
    tyvek = new G4Material( "tyvek",0.96*g/cm3,2);
    tyvek->AddElement( natH, 2);
    tyvek->AddElement( natC, 1);

    // BF3 from
http://encyclopedia.airliquide.com/encyclopedia.asp?GasID=68
    bf3 = new G4Material( "bf3",2.84*kg/m3,2);
    bf3->AddElement( natB, 1);
    bf3->AddElement( natF, 3);

    // SS304 http://www.azom.com/Details.asp?ArticleID=965
    ss304 = new G4Material( "ss304",8000*kg/m3,9);
    ss304->AddElement( natFe, 66.5*perCent);
    ss304->AddElement( natC, 0.08*perCent);
    ss304->AddElement( natMn, 2.00*perCent);
    ss304->AddElement( natSi, 0.75*perCent);
    ss304->AddElement( natP, 0.045*perCent);
    ss304->AddElement( natS, 0.03*perCent);
    ss304->AddElement( natCr, 20.0*perCent);
    ss304->AddElement( natNi, 10.5*perCent);
    ss304->AddElement( natN, 0.10*perCent);

    // 6061 Al alloy. Composition provided by Dave Johnson.
    al6061= new G4Material( "al6061",2.7*g/cm3,9);
    al6061->AddElement( natAl, 96.10*perCent);
    al6061->AddElement( natSi, 0.80*perCent);
    al6061->AddElement( natFe, 0.70*perCent);
    al6061->AddElement( natMn, 0.15*perCent);
    al6061->AddElement( natMg, 0.15*perCent);
    al6061->AddElement( natCr, 1.20*perCent);
    al6061->AddElement( natCu, 0.40*perCent);
    al6061->AddElement( natZn, 0.35*perCent);
    al6061->AddElement( natTi, 0.15*perCent);

    air = new G4Material( "air",1.184*kg/m3,2);
    air->AddElement( natN, 80.0*perCent);
    air->AddElement( natO, 20.0*perCent);

    polyethylene = new G4Material( "polyethylene", 0.94*g/cm3, 2 );
    polyethylene->AddElement( natC, 1 );
    polyethylene->AddElement( natH, 2 );

```

```

vacuum = new G4Material( "vacuum", 1., 1.008*g/mole, 1.e-
25*g/cm3,kStateGas, 273*kelvin, 3.8e-18*pascal );

quartz = new G4Material( "quartz", 2.65*g/cm3, 2 );
quartz->AddElement( natSi, 1 );
quartz->AddElement( natO, 2 );

water = new G4Material( "water", 1*g/cm3, 2 );
water->AddElement( natH, 2 );
water->AddElement( natO, 1 );

gadolinium = G4NistManager::Instance()-
>FindOrBuildMaterial("G4_Gd");

dopedWater = new G4Material("dopedWater",1.0*g/cm3,2);
dopedWater->AddMaterial(water, 99.9*perCent);
dopedWater->AddMaterial(gadolinium, 0.1*perCent);
}

```

C.2. Optical photons

The following code snippet shows how most photons that have energies other than that of interest can be “killed” to save on computational time. The photons must satisfy three conditions in order to be accounted for: (1) be optical photons with energies between 1.0 eV and 4.5 eV, be newly born (created by a charged particle), be created in water Cherenkov volume. The code is part of user-defined “Stacking Action.”

```

if(particleName=="opticalphoton" && currentTrack-
>GetTrackLength()==0 && currentVolumeName == "Water")
{
    G4double KE = currentTrack->GetKineticEnergy();
    if(KE>4.5*eV && KE<1.0*eV) status = fKill;
    else {
        RunAction->IncrCerenkovPhotonCreated();
    }
}

```

```
}
```

C.3. Sample ROOT output analysis code

```
{  
  
  gStyle->SetOptStat(0);  
  gStyle->SetFrameFillColor(19);  
  gStyle->SetOptLogy(1);  
  
  //GRAB SPECTRUM HISTOGRAMS  
  
  //OPENING ROOT HISTOGRAMS  
  //m40 - studies of reflectivity effects  
  TFile  
  fm20_70("/Applications/g4work/MIT/Th232/myOTNSim_2cm.root");  
  TTree * m20_70_spectrum = (TTree *)fm20_70.Get("event_tree");  
  
  TFile  
  fm20_80("/Applications/g4work/MIT/Th232/myOTNSim_25cm.root");  
  TTree * m20_80_spectrum = (TTree *)fm20_80.Get("event_tree");  
  
  TFile  
  fm20_90("/Applications/g4work/MIT/Th232/myOTNSim_50cm.root");  
  TTree * m20_90_spectrum = (TTree *)fm20_90.Get("event_tree");  
  
  TFile  
  fm20_98("/Applications/g4work/MIT/Th232/myOTNSim_75cm.root");  
  TTree * m20_98_spectrum = (TTree *)fm20_98.Get("event_tree");  
  
  Int_t numPmtHits;  
  
  TH1F * m20_70_plot = new TH1F ("m20_70_plot", "232Th", 80., 1., 80.);  
  m20_70_spectrum -> SetBranchAddress("numPmtHits", &numPmtHits);  
  for(int i=0; i<m20_70_spectrum ->GetEntries(); i++){  
    m20_70_spectrum ->GetEntry(i);  
    m20_70_plot->Fill(numPmtHits);  
  }  
  TH1F * m20_80_plot = new TH1F  
  ("m20_80_plot", "m20_80", 80., 1., 80.);
```

```

m20_80_spectrum -> SetBranchAddress("numPmtHits",&numPmtHits);
for(int i=0; i<m20_80_spectrum ->GetEntries(); i++){
    m20_80_spectrum ->GetEntry(i);
    m20_80_plot->Fill(numPmtHits);
}
TH1F * m20_90_plot = new TH1F
("m20_90_plot","m20_90",80.,1.,80.);
m20_90_spectrum -> SetBranchAddress("numPmtHits",&numPmtHits);
for(int i=0; i<m20_90_spectrum ->GetEntries(); i++){
    m20_90_spectrum ->GetEntry(i);
    m20_90_plot->Fill(numPmtHits);
}
TH1F * m20_98_plot = new TH1F
("m20_98_plot","m20_98",80.,1.,80.);
m20_98_spectrum -> SetBranchAddress("numPmtHits",&numPmtHits);
for(int i=0; i<m20_98_spectrum ->GetEntries(); i++){
    m20_98_spectrum ->GetEntry(i);
    m20_98_plot->Fill(numPmtHits);
}

//DRAW SPECTRUM HISTORGRAMS
TCanvas * c1 = new TCanvas;

c1 -> SetBorderMode(0);
c1 -> SetFillColor(kWhite);

m20_70_plot -> GetXaxis() -> SetTitle("Number of PEs created by
each gamma");
m20_70_plot -> GetYaxis() -> SetTitle("^{232}Th, 100,000
histories");
m20_70_plot -> SetLineColor(1);
m20_70_plot ->Draw();

m20_80_plot -> SetLineColor(2);
m20_80_plot ->Draw("same");

m20_90_plot -> SetLineColor(3);
m20_90_plot ->Draw("same");

m20_98_plot -> SetLineColor(4);
m20_98_plot ->Draw("same");

leg1 = new TLegend(0.6,0.7,0.89,0.89); //coordinates are
fractions of pad dimensions
leg1->AddEntry(m20_70_plot,"2 cm","1");
leg1->AddEntry(m20_80_plot,"25 cm","1");

```

```

leg1->AddEntry(m20_90_plot,"50 cm","l"); // "l" means line, use
"f" for a box
leg1->AddEntry(m20_98_plot,"75 cm","l");

leg1->Draw();

leg1->SetHeader("^{}Th source");
leg1->Draw();

Float_t sum_m20_70 = 0;
Float_t sum_m20_80 = 0;
Float_t sum_m20_90 = 0;
Float_t sum_m20_98 = 0;

TH1F *m20_70_int = new TH1F("m20_70_int","Effect of cuts >
20pe on photon collection",80.,1.,80.);
TH1F *m20_80_int = new TH1F("m20_80_int","h1 bins
integral",80.,1.,80.);
TH1F *m20_90_int = new TH1F("m20_90_int","h1 bins
integral",80.,1.,80.);
TH1F *m20_98_int = new TH1F("m20_98_int","h1 bins
integral",80.,1.,80.);

//above 20 PE
for (Int_t i=1;i<=80;i++) {
sum_m20_70 += m20_70_plot->GetBinContent(i);
m20_70_int->SetBinContent(i,sum_m20_70);
sum_m20_80 += m20_80_plot->GetBinContent(i);
m20_80_int->SetBinContent(i,sum_m20_80);
sum_m20_90 += m20_90_plot->GetBinContent(i);
m20_90_int->SetBinContent(i,sum_m20_90);
sum_m20_98 += m20_98_plot->GetBinContent(i);
m20_98_int->SetBinContent(i,sum_m20_98);
}
cout<<"integrated value of counts 70% refl, 20 m water is
"<< m20_70_int->GetBinContent(80)<<endl;
cout<<"integrated value of counts 80% refl, 20 m water is
"<< m20_80_int->GetBinContent(80)<<endl;
cout<<"integrated value of counts 90% refl, 20 m water is
"<< m20_90_int->GetBinContent(80)<<endl;
cout<<"integrated value of counts 98% refl, 20 m water is
"<< m20_98_int->GetBinContent(80)<<endl;

TCanvas * c2 = new TCanvas;

```

```
c2 -> SetBorderMode(0);
c2 -> SetFillColor(kWhite);

    m20_70_int -> GetXaxis() -> SetTitle("Integrated number of
PEs");
    m20_70_int -> GetYaxis() -> SetTitle("Integrated values");
    m20_70_int -> SetLineColor(6);
    m20_70_int -> Draw();

    m20_70_int -> SetLineColor(1);
    m20_70_int -> Draw("same");

    m20_80_int -> SetLineColor(2);
    m20_80_int -> Draw("same");

    m20_90_int -> SetLineColor(3);
    m20_90_int -> Draw("same");

    m20_98_int -> SetLineColor(4);
    m20_98_int -> Draw("same");

}
```


List of acronyms and abbreviations

| | |
|------|-------------------------------|
| ADC | Analog-to-Digital Converter |
| DAQ | Data Acquisition |
| DAS | Data Acquisition System |
| dps | Disintegrations per second |
| FIFO | Fan-In/Fan-Out |
| FPGA | Field Programmable Gate Array |
| FWHM | Full Width Half Maximum |
| MCA | Multichannel analyser |
| p.e. | Photoelectron |
| PMT | Photomultiplier Tube |
| QDC | Charge-to-Digital Conversion |
| QE | Quantum efficiency |

WFD Waveform Digitizer

WLS Wavelength shifters